

UNIVERSITY OF CALIFORNIA

Santa Barbara

**Coarse-Grained Analysis of Collective Motion in Animal Groups**

A Dissertation submitted in partial satisfaction of the  
requirements for the degree of Doctor of Philosophy  
in Mathematics

by

Allison Kolpas

Committee in charge:  
Professor Jeffrey Moehlis, Chair  
Professor Hector Ceniceros  
Professor Roger Nisbet

June 2008

The dissertation of Allison Kolpas is approved.

---

Professor Hector Ceniceros

---

Professor Roger Nisbet

---

Professor Jeffrey Moehlis, Committee Chair

June 2008

**Coarse-Grained Analysis of Collective Motion in Animal Groups**

Copyright 2008

by

Allison Kolpas

To my husband Shawn, for his constant love and support.

## Acknowledgments

This thesis could not have been written without the encouragement and support of my advisor Jeff Moehlis. He is an amazing teacher, researcher, and mentor, and has been truly inspiring. Much thanks also goes to my committee members Hector Cenicerros and Roger Nisbet for their valuable suggestions and advice.

I want to thank Bjorn Birnir, Iain Couzin, Thomas Frewen, Danny Grünbaum, Yannis Kevrekidis, and Simon Levin for helpful discussions related to the research. I especially want to thank Iain Couzin for the opportunity to work with him at Oxford University. He is an extraordinary scientist and has helped me to better understand the biology of self-organized animal groups. I also want to thank Yannis Kevrekidis for all of the useful conversations regarding equation-free coarse-grained computation and his guidance with the research. Also, thanks to Hong Li and Linda Petzold at UCSB for their assistance in programming a graphics processing unit to perform simulations of the two-dimensional schooling model in parallel.

Finally, I want to acknowledge and thank my husband Shawn Pfeil, my father Dr. Sidney J. Kolpas, my mother Laurie P. Kolpas, and my sister Jamie Kolpas, for their love, support, and encouragement. Now there will be another “Dr. K” in the family!

# Vita of Allison Kolpas

## Education

Ph.D Mathematics, University of California, Santa Barbara	June 2008
M.A. Mathematics, University of California, Santa Barbara	June 2004
B.A. Mathematics, <i>cum laude</i> , Revelle College, University of California, San Diego	June 2002

## Professional Employment

Graduate Student Researcher, UCSB	2005-2008
Teaching Associate, UCSB	Summer 2004
Instructor, Summer Transition Enrichment Program, UCSB	Summer 2005,2006
Teaching Assistant, UCSB	2002-2005

## Publications

A. Kolpas, J. Moehlis, and I. G. Kevrekidis, Coarse Analysis of Stochasticity-Induced Switching Between Collective Motion States. *Proc. Nat. Acad. Sci. USA* **104**, 5931-5936, 2007.

H. Li, A. Kolpas, L. Petzold, and J. Moehlis, Parallel Simulation for a Fish Schooling Model on a General-Purpose Graphics Processing Unit, to appear *Concurrency and Computation: Practice and Experience*

A. Kolpas and J. Moehlis, Optimal Switching Between Collective Motion States for Two Agents, to appear *Applied Mathematics Letters*

## Awards and Honors

IGERT Associate, Systems Biology, UCSB	Spring 2007-present
----------------------------------------	---------------------

## Abstract

Coarse-Grained Analysis of Collective Motion in Animal Groups

by

Allison Kolpas

In this dissertation, we present a framework for the coarse, population-level analysis of the collective motion of animal groups whose dynamics are described by models at the individual-level.

For a one-dimensional model of self-organized group formation, we observe stochasticity-induced switching between two metastable collective motion states. We characterize the behavior of this system with a single dynamically meaningful “coarse observable” whose dynamics are described by an effective Fokker-Planck equation. This leads to the construction of an effective potential, which is used to locate metastable states, determine their parametric dependence, and estimate mean switching times between the states. Both empirical and automated, data-driven techniques are used to find suitable coarse observables. For the empirical observable, a “lifting” procedure is presented, which enables more efficient estimation of the drift and diffusion terms in the Fokker-Planck equation through short bursts of appropriately initialized simulations.

We then present a continuous-time model for two interacting agents with coupled oscillator dynamics, and consider how to design interaction rules which si-

multaneously stabilize different collective motion states. Variational methods are used to determine the optimal input to the steering control of one of the agents which leads to switching between these collective states. Existence and uniqueness of the optimal input is proved, and a transition time symmetry between different switching problems is identified.

Finally, we explore the relationship between spatial position and information transfer in fish schools. We present a two-dimensional individual-based model for fish schooling, and use a cross-correlation function to quantify how perturbations in the headings of individual members affects the dynamics at the population-level. We find that as schools become polarized, they respond more strongly and rapidly to perturbations. Furthermore, individuals in the second quartile, as measured by rank, induce the largest response and thus have more “control” over the group motion.

Overall, the techniques and analysis described in this dissertation allow us to gain a new level of understanding and quantification of biological self-organization by bridging individual-based modeling with coarse, population-level analysis.

# Contents

<b>List of Figures</b>	<b>xi</b>
<b>1 Introduction</b>	<b>1</b>
1.1 Self-Organization . . . . .	1
1.2 Modeling . . . . .	3
1.3 Aims and Scope . . . . .	5
<b>2 Coarse Analysis of Stochasticity-Induced Switching in an Individual-Based Schooling Model</b>	<b>8</b>
2.1 Introduction . . . . .	8
2.2 The Model . . . . .	13
2.2.1 Coarse Observable . . . . .	17
2.2.2 Computational Observations . . . . .	18
2.3 Macroscopic Description . . . . .	20
2.3.1 Numerical Model Validation . . . . .	22
2.4 Effective Potential: Long-Time Simulations . . . . .	25
2.5 Effective Potential: Short-Time Simulations . . . . .	28
2.5.1 Lifting Algorithm . . . . .	33
2.5.2 Results . . . . .	34
2.6 Mean Residence Times . . . . .	36
2.7 Coarse Bifurcation Diagrams . . . . .	38
2.8 Conclusion . . . . .	38
<b>3 Coarse Analysis of Collective Motion with Different Communication Mechanisms</b>	<b>42</b>
3.1 Introduction . . . . .	42
3.2 The Model . . . . .	44
3.3 Diffusion maps: data-driven detection of coarse observables . . . . .	46
3.3.1 Background . . . . .	46
3.3.2 Diffusion Map Theory . . . . .	46
3.3.3 Diffusion Map Coordinates and Nyström extension . . . . .	48
3.4 Distance measure for the Schooling Model . . . . .	50

3.5	Diffusion Map Coordinates for the Schooling Model . . . . .	52
3.6	Estimating the Effective Potential and Mean Residence Times . . .	57
3.7	Coarse Bifurcation Diagrams . . . . .	61
3.8	Conclusion . . . . .	62
<b>4</b>	<b>Bistability in a Model for Collective Motion with Coupled Oscillator Dynamics</b>	<b>66</b>
4.1	Introduction . . . . .	66
4.2	The Model . . . . .	68
4.2.1	Fixed Points and Stability . . . . .	69
4.2.2	Coupling Function and Bistability . . . . .	71
4.3	Stochasticity-Induced Switching . . . . .	76
4.3.1	Coarse Analysis . . . . .	77
4.3.2	Numerical Simulations . . . . .	78
4.3.3	Coarse-Grained Computation . . . . .	80
4.4	Conclusion . . . . .	84
<b>5</b>	<b>Optimal Switching between Coexisting Collective Motion States</b>	<b>85</b>
5.1	Introduction . . . . .	85
5.2	Optimal Switching . . . . .	86
5.3	Existence and Uniqueness of $I(t)$ . . . . .	89
5.4	Transition Time Symmetry . . . . .	90
5.5	Example . . . . .	91
5.6	Conclusion . . . . .	97
<b>6</b>	<b>Spatial Position and Information Transfer in a Schooling Model</b>	<b>99</b>
6.1	Introduction . . . . .	99
6.2	The Model . . . . .	100
6.3	Observables . . . . .	103
6.4	Simulation Statistics . . . . .	104
6.5	Spatial Position and Information Transfer . . . . .	109
6.5.1	Perturbing a Single Individual . . . . .	109
6.5.2	Perturbing Multiple Individuals . . . . .	114
6.6	Conclusion . . . . .	115
<b>A</b>	<b>Derivation of the Fokker-Planck Equation</b>	<b>118</b>
<b>B</b>	<b>Derivation of Mean Residence Times and Kramers Formula</b>	<b>123</b>
<b>C</b>	<b>Diffusion Maps and Principal Component Analysis</b>	<b>127</b>
<b>D</b>	<b>Parallel Simulation on a GPU</b>	<b>130</b>
	<b>Bibliography</b>	<b>133</b>

# List of Figures

2.1	Four collective motion states . . . . .	10
2.2	Stochasticity-induced switching in a three-dimensional schooling model . . . . .	11
2.3	Behavioral zones for the one-dimensional schooling model . . . . .	14
2.4	Stochasticity-induced switching in the one-dimensional schooling model . . . . .	16
2.5	Probability distribution functions and effective potentials . . . . .	19
2.6	PDF and autocorrelation function . . . . .	24
2.7	Estimate of $D^{(1)}(A)$ , $D^{(2)}(A)$ , and $U(A)$ . . . . .	27
2.8	Trajectories approach the slow manifold $x = y$ . . . . .	30
2.9	Trajectories approach the slow manifold in $(A, S)$ plane . . . . .	31
2.10	Comparison of effective potentials . . . . .	35
2.11	Distribution of residence times . . . . .	36
2.12	Coarse-grained bifurcation diagram . . . . .	39
3.1	Diffusion map coordinate representation of a school . . . . .	54
3.2	Data collapse on an approximately one-dimensional manifold . . . . .	55
3.3	Comparison of $\Phi_2^{(i)}$ and $A$ on two “neutrally stable” datasets . . . . .	56
3.4	Comparison of a pdf and effective potential for the original and signal constrained model . . . . .	58
3.5	Estimate of $D^{(1)}(\Phi_2)$ , $D^{(2)}(\Phi_2)$ , and $U(\Phi_2)$ . . . . .	60
3.6	Comparison of bifurcation diagrams for the original and signal constrained model . . . . .	63
4.1	Phase-locked states and collective motion . . . . .	72
4.2	Existence and stability of $S_2$ , $Z_2$ , and $S_1 \times S_1$ state . . . . .	74
4.3	Pitchfork bifurcation of the $Z_2$ state . . . . .	75
4.4	Stochasticity-induced switching in phase-reduced model . . . . .	79
4.5	Numerical estimates of drift and diffusion terms . . . . .	82
4.6	Numerical estimate of effective potential . . . . .	83
5.1	Optimal input for transitions from $S_2$ to $Z_2$ . . . . .	92
5.2	Optimal input for transitions from $Z_2$ to $S_2$ . . . . .	92
5.3	Transition in the $(\psi, \lambda)$ plane from $S_2$ to $Z_2$ . . . . .	93
5.4	Transition in the $(\psi, \lambda)$ plane from $Z_2$ to $S_2$ . . . . .	94

5.5	Transition in the $(x, y)$ plane from $S_2$ to $Z_2$ . . . . .	95
5.6	Transition in the $(x, y)$ plane from $Z_2$ to $S_2$ . . . . .	96
6.1	Statistics for schools of size $N = 25, 50, 100, 150$ . . . . .	106
6.2	Illustration of fragmentation processes . . . . .	107
6.3	Average heading autocorrelation function . . . . .	108
6.4	Cross-correlation functions and sample schools . . . . .	111
6.5	Peak correlation as a function of $r$ . . . . .	113
6.6	Response to multiple perturbations in the 2nd quartile . . . . .	115
6.7	Peak response to multiple perturbations . . . . .	116
C.1	Two gaussian clouds . . . . .	128
C.2	PCA vs. diffusion map representation of dataset . . . . .	129

# Chapter 1

## Introduction

### 1.1 Self-Organization

Many organisms move collectively in groups such as schools of fish, flocks of birds, herds of wildebeest, and swarms of locusts [11, 62, 83, 85, 98, 101]. Often such groups are *self-organized*, that is, the collective motion arises from local interactions of individual agents with their neighbors, without any regard to a leader, template, or other external cue [11]. The number of individuals involved in such collective motion can be huge, from several hundred thousand wildebeests migrating on the Serengeti plain to millions of Atlantic cod off the Newfoundland coast. Despite these large numbers, the group can seem to move as a single organism, with all individuals rapidly responding to their neighbors to maintain the collective motion.

Self-organized animal groups are believed to be maintained through simple positive and negative feedback mechanisms at the individual level such as behavioral

matching (allelomimesis), repulsion, and attraction [8, 11, 57, 85]. The ability to sense and communicate with one's neighbors is crucial for group formation and maintenance. For fish schooling, it is believed that vision and the lateral line, an organ sensitive to changes in water pressure, are the main sensory systems involved [85, 87]. Signalling is often an important communication tool. For example, flocks of birds may use vocal cues to coordinate group motion [106], while chemical signals are used by a variety of groups including colonies of ants [8] and cellular slime molds [50].

Group living is often advantageous, allowing individuals to increase their harvesting efficiency [64, 85], better follow migration routes [18, 37], improve their aerodynamic efficiency [65, 105], and avoid predation [23, 73]. However, the costs and benefits of group membership are not evenly distributed among members [83]. For example, individuals located near the front of a fish school are more likely to maximize their food uptake but may have a greater risk of predation [55]. For birds flying in a Vee formation, the lead bird saves less energy than those trailing behind [2].

Groups are capable of performing complex tasks not possible at the individual level such as pattern formation, decision making, and information processing [8, 11, 21]. For example, schools of fish may display a variety of complex patterns in response to a predator such as compression, hourglass, vacuole, fountain, or flash expansion [84]. Ant colonies are capable of making decisions such as choosing between food sources and nest sites as well as selecting the shortest path between

them [8]. Animals traveling in polarized groups, such as fish schools and bird flocks, act as an integrated array of sensors, capable of processing and transferring information such as the location of resources or predators [17].

Animal groups can quickly and efficiently transition between different behavioral patterns. These transitions could be due to changing behavioral rules, environmental factors including introduction of predators, or stochastic effects. Different collective behaviors serve different functions. For example, a school of fish might be composed of individuals all approximately swimming in the same fixed direction (e.g., to find food), later changing to a state in which individuals move in a swarm (e.g., for food uptake).

It is of fundamental importance to understand how and why animal groups change between different collective states and how individual decisions effect the group dynamics. Questions of this nature arise in the control and prediction of locust swarm outbreaks, management of over fishing, crowd and traffic control in human populations, as well as the design and control of unmanned vehicles and sensor networks.

## 1.2 Modeling

Many different types of mathematical models have been formulated to analyze and predict the collective dynamics of self-organizing animal groups, see e.g., [3, 19, 25, 77, 90, 100, 102]. Such models can be classified into two main categories: population-based and individual-based.

Population-based or “Eulerian” formulations use partial differential equations to model the dynamics of a group. In animal aggregation, the evolution of the population density and velocity vector field are modeled as nonlinear partial differential equations [100]. Population-based models are typically constructed *a priori* [24, 68, 100] since coarse-graining from individual-level formulations is difficult [99]. Analytical progress, such as the derivation of conditions for existence and uniqueness of solutions as well as stability analysis, is often possible using the theory of partial differential equations.

In individual-based “Lagrangian” formulations, the dynamics of each interacting agent is prescribed. Individual-based formulations are used most often in modeling animal aggregation because they provide a natural description of the system as a set of interacting agents, can be more readily linked to experimental data, and are quite flexible [7]. Individual-based models can be further classified into two categories: continuous-time and discrete-time.

Continuous-time models of collective motion at the individual-level use coupled ordinary or stochastic differential equations to describe the evolution of a group of interacting self-propelled particles <sup>1</sup> in time. In some cases, equations for the positions and velocities of the agents are formulated using Newton’s laws, where individuals react to forces by accelerating [28, 69]. In other cases, models are used which prescribe equations for the positions and headings of agents traveling at constant speed so that they can maneuver by steering but not by speeding

---

<sup>1</sup>In the physics literature individuals are commonly referred to as “particles”, while in the engineering community the term “agents” is commonly used.

up or slowing down [82]. Some analytical progress has been made using mean-field approximations [88], and when models are proposed as gradient systems [69] or with coupled oscillator dynamics [95], however numerical simulations are more commonly employed.

Discrete-time individual-based or *agent-based* models use update rules to simulate the movement of agents in discrete units of time [19, 43, 45, 91, 102]. Agent-based models can incorporate biologically realistic behavioral responses and social interactions that might be discontinuous (e.g., characterized by thresholds or if/then rules) or stochastic in nature, support complex network topologies, and allow for individual variability. Most importantly, they allow one to study the relationship between adaptive behavior at the individual-level and emergent phenomena at the population-level [36]. Most analysis of discrete-time individual-based models relies on computationally expensive long-time equilibrium simulations which can be difficult to interpret and analyze [3, 19, 43, 102].

### 1.3 Aims and Scope

In this dissertation, our aim is to develop mathematical and computational methods for the analysis of the collective dynamics of animal groups described by models at the individual-level. Both discrete and continuous-time models are presented and analyzed using coarse-grained computation and theory from stochastic processes and dynamical systems. We focus our attention on understanding the mechanisms of switching between different collective states, including the role of

spatial position on information transfer.

In Chapters 2 and 3 we will show how repeated switching between distinct collective states can occur entirely because of stochastic effects. Here we formulate a one-dimensional individual-based model for self-organized group formation and develop methods for efficient analysis of the population-level dynamics using coarse-grained computation. The group behavior is characterized with a single observable whose dynamics are described by an effective Fokker-Planck equation. Both empirical (Chapter 2) and automated, data-driven (Chapter 3) techniques are used to identify a suitable coarse observable. With this formalism, an effective potential is constructed as a function of the coarse observable and used to perform *coarse bifurcation analysis*, by locating metastable collective states and their parametric dependence, and estimate mean switching times. Such an approach allows one to quantify how collective behavior at the population-level emerges from simple interaction laws at the individual-based level.

In Chapters 4 and 5 we will present a continuous-time kinetic model for two interacting agents with coupled oscillator dynamics that is amenable to analysis. In Chapter 4, we derive conditions for the existence of bistability between coherent and incoherent motion. In the bistable regime, with the addition of noise, the system exhibits switching between collective motion states. An effective potential is derived analytically and the results are compared with estimates obtained using the coarse-grained computational framework of Chapter 2. In Chapter 5, we will solve for the optimal input to the heading control of one of the agents to induce

switching between the different collective states. We identify a transition time symmetry between switching problems and prove the existence and uniqueness of an optimal input.

For the one-dimensional schooling model developed in Chapters 2 and 3, we note that transitions often begin with a stochastic change in the heading of an individual at the edge of a school which then propagates throughout the rest of the school. In Chapter 6, we explore the role of spatial position with respect to information transfer for a two-dimensional individual-based schooling model. Here, we identify the best “control” positions using a cross-correlation function to measure the response of a school to internal perturbations in the heading of individual members. Unlike the one-dimensional schooling model, we find that individuals in the middle and not the edge propagate information most efficiently.

# Chapter 2

## Coarse Analysis of Stochasticity-Induced Switching in an Individual-Based Schooling Model

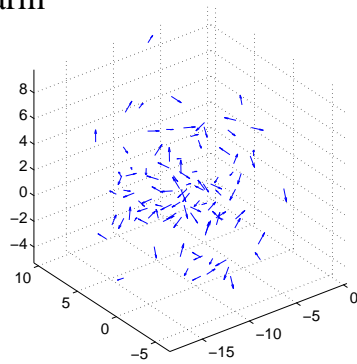
### 2.1 Introduction

One class of biologically motivated individual-based models for group formation, frequently used for schooling fish, abstracts animal behavior by placing zones around individuals in which they respond to others through repulsion, alignment, and/or attraction [3, 19, 20, 45, 84, 89, 93, 104]. In the three-dimensional model of Couzin *et al.* [19], interactions take place within three concentric zones around an

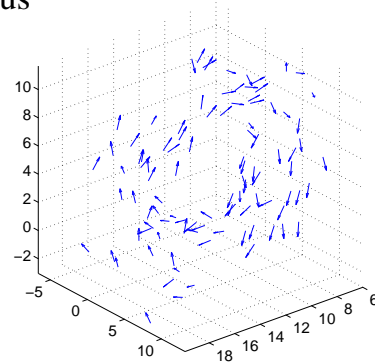
individual: a “zone of repulsion”, “zone of orientation”, and “zone of attraction”, the latter two excluding a blind volume behind the individual for which neighbors are undetectable. Stochasticity is included to account for imperfect sensing and processing. For different values of the parameters (width of the behavioral zones), long-time steady state computations revealed four different types of stable collective behaviors: swarm, torus (milling), dynamic parallel, and highly parallel; see Figure 2.1. For certain values of the parameters, bistability was observed between the dynamic parallel and the milling behaviors with *hysteresis*, that is, the previous history of the group behavioral pattern influences the collective behavior of the group as parameters related to individual-level behaviors change.

In [19], stochasticity is incorporated by adding noise (with probability  $p = 1$ ) at each time step to an agent’s desired heading, determined by its interactions with neighbors within the three zones. In practice, this is performed by drawing a new direction of travel from a spherically wrapped normal distribution of small variance centered about the agent’s desired heading. If instead noise is added to an agent’s desired heading with probability  $p < 1$  and drawn from a spherically wrapped normal distribution with relatively large variance, then for certain regions of parameter space, multiple successive transitions between the torus and the dynamic parallel state can occur; see Figure 2.2. Such “stochasticity-induced” switching demonstrates a mechanism for which a school can change between different collective states, without a need for a change in the quantitative features of the behavioral rules of all of the individual members.

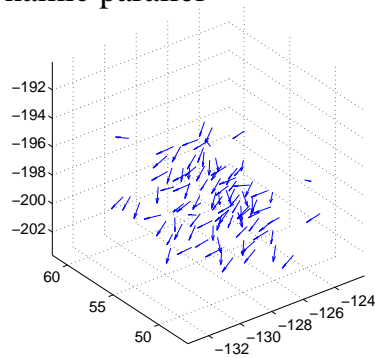
(a) swarm



(b) torus



(c) dynamic parallel



(d) highly parallel

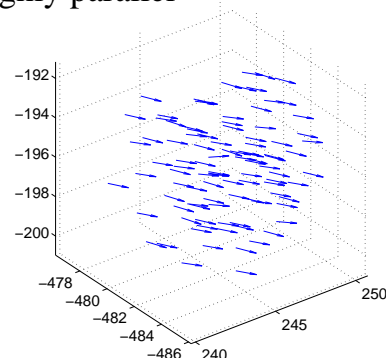


Figure 2.1: Four possible collective states of the individual-based model of Couzin, et. al. [19]: (a) swarm, (b) torus, (c) dynamic parallel, and (d) highly parallel.

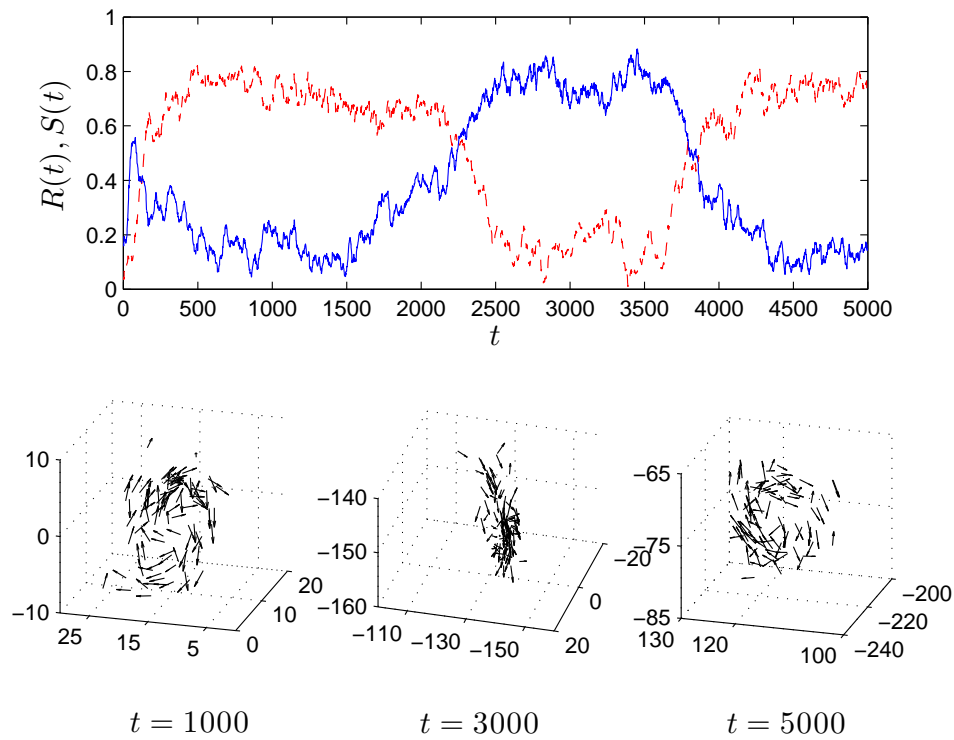


Figure 2.2: Transitions between the torus state and the dynamic parallel state for a modified version of the three-dimensional schooling model of Couzin *et. al.* [19] with  $\Delta r_o = 2$  and  $\Delta r_a = 9$ ,  $p = 0.005$ ,  $\sigma = 5$ . (Red)  $R(t)$  = angular momentum, (Blue)  $S(t)$  = group polarization, both normalized.

In this chapter, we will study such stochasticity-induced transitions in a corresponding one-dimensional version of the individual-based schooling model. The model exhibits repeated stochasticity-induced switching between two distinct ordered collective motion states, a *mobile* state, in which the school travels in the positive or negative direction, and a *stationary* state, in which the dynamics are driven by repulsion, and the school remains approximately stationary in time. This switching is similar in nature, but different in detail, from results obtained using other such models of group formation. In those cases, collective motion transitions between *symmetry-related* states (e.g. between clockwise and counterclockwise motions for marching locusts constrained to a ring [10], or the “alternating flock” in [79, 88]), stochastically-driven transitions between ordered and disordered states mediated by clustering [43], mixed phase states at phase transition boundaries [35], or transitions which do not occur repeatedly [28] were observed.

To analyze the dynamics of the one-dimensional schooling model, we will use coarse-grained computation. Although the interactions among individuals are complicated, the group’s collective behavior is quantifiable in a simple way. We characterize this with a single *coarse observable*,  $A(t)$ , a scalar variable which measures the average distance to an agent’s nearest neighbor, quantifying the global structure of the school. We show computational evidence to support that  $A(t)$  parameterizes a one-dimensional, attracting, invariant *slow manifold*, which correlates with the steady-state dynamics of the system. This, along with further numerical verification of the statistical properties of  $A$ , suggests that  $A$  obeys an effective Langevin

equation, or equivalently its probability distribution  $P(A)$  obeys an effective Fokker-Planck (FP) equation, whose drift and diffusion coefficients are determined by the short-time evolution of the first two moments of  $A$ . We locally estimate these coefficients by developing a *lifting* algorithm which enables efficient estimation of the drift and diffusion terms through short bursts of appropriately initialized simulations [51]. This framework allows us to construct an effective potential, thereby enabling coarse bifurcation analysis and estimation of the mean residence times in each collective state. Local estimation of the FP coefficients through the use of the *lifting* algorithm allows us to perform such coarse analysis without the need for computationally expensive “long-time” equilibrium simulations of the individual-based model.

## 2.2 The Model

$N$  agents with positions  $c_i(t)$  and unit directions  $\hat{v}_i(t) = \pm 1$ ,  $i = 1, \dots, N$ , move on the line with constant speed  $s$ . Every time step  $\tau$ , individuals simultaneously determine their direction of travel by considering neighbors within three non-overlapping zones, the zone of repulsion  $Z_{r_i}(t) = (c_i(t) - r_r, c_i(t) + r_r)$ , zone of orientation  $Z_{o_i}(t) = (c_i(t) - r_o, c_i(t) + r_o) \setminus Z_{r_i}(t)$ , and zone of attraction  $Z_{a_i}(t) = (c_i(t) - r_a, c_i(t) + r_a) \setminus (Z_{r_i}(t) \cup Z_{o_i}(t))$ , where  $r_r$  is the radius of repulsion,  $r_o$  the radius of orientation, and  $r_a$  the radius of attraction. We denote the width of the zone of orientation as  $\Delta r_o = r_o - r_r$ , and the width of the zone of attraction as  $\Delta r_a = r_a - r_o$ . See Figure 2.3 for a schematic diagram of these behavioral zones.



Figure 2.3: Behavioral Zones for the 1D Model

These zones are used to define rules which are abstractions of the behavioral tendencies seen in animals groups in nature, the first being that animals tend to repel away from those that are too close, and the second that, if they are not so repelled, they tend to align with and feel an attraction towards their neighbors [57, 85]. Specifically, if individual  $i$  finds other agents within its zone of repulsion, then it orients its direction away from the average relative directions of those agents. Its desired direction of travel in the next time step is given by

$$v_i(t + \tau) = - \sum_{\substack{c_j(t) \in Z_{r_i}(t) \\ i \neq j}} \frac{c_j(t) - c_i(t)}{|c_j(t) - c_i(t)|}. \quad (2.1)$$

This vector is normalized as  $\hat{v}_i(t + \tau) = \frac{v_i(t + \tau)}{|v_i(t + \tau)|}$ , assuming  $v_i(t + \tau) \neq 0$ . In the case that  $v_i(t + \tau) = 0$ , agent  $i$  maintains its previous direction of travel as its desired direction of travel, giving  $\hat{v}_i(t + \tau) = \hat{v}_i(t)$ .

If individual  $i$  does not find agents within its zone of repulsion, it aligns its direction toward an equally weighted combination of the average direction of itself and those within its zone of orientation,  $o_i(t)$ , and the average relative direction of those within its zone of attraction,  $a_i(t)$ . Its desired direction of travel in the next time step is given by

$$v_i(t + \tau) = o_i(t) + a_i(t), \quad (2.2)$$

where,

$$o_i(t) = \frac{\hat{v}_i(t) + \sum_{c_j(t) \in Z_{o_i}(t)} \hat{v}_j(t)}{\left| \hat{v}_i(t) + \sum_{c_j(t) \in Z_{o_i}(t)} \hat{v}_j(t) \right|}, \quad a_i(t) = \frac{\sum_{c_j(t) \in Z_{a_i}(t)} \frac{c_j(t) - c_i(t)}{|c_j(t) - c_i(t)|}}{\left| \sum_{c_j(t) \in Z_{a_i}(t)} \frac{c_j(t) - c_i(t)}{|c_j(t) - c_i(t)|} \right|}. \quad (2.3)$$

The total contribution from orientation and alignment is then normalized as  $\hat{v}_i(t + \tau) = \frac{v_i(t + \tau)}{|v_i(t + \tau)|}$ , assuming  $v_i(t + \tau) \neq 0$ . As before, if  $v_i(t + \tau) = 0$ , then agent  $i$  maintains its previous direction of travel. Stochastic effects are incorporated into the model by changing the sign of agent  $i$ 's desired direction with probability  $p$ . Finally, each agents' position is updated simultaneously according to

$$c_i(t + \tau) = c_i(t) + s\hat{v}_i(t + \tau)\tau. \quad (2.4)$$

To begin a simulation,  $N$  individuals are placed randomly on the interval  $[-\frac{N}{4}, \frac{N}{4}]$  with random directions, chosen so that each agent initially interacts with at least one other agent.

In certain regions of parameter space, the model can display two metastable cohesive collective states which we call *stationary* and *mobile*. In the stationary state, the individual dynamics are driven by repulsion. The school remains approximately stationary in time as agents on average change their direction at each time step in order to avoid neighbors to the right or left. We interpret this ordered stationary state as a one-dimensional analog of circular milling behavior. In the mobile state,

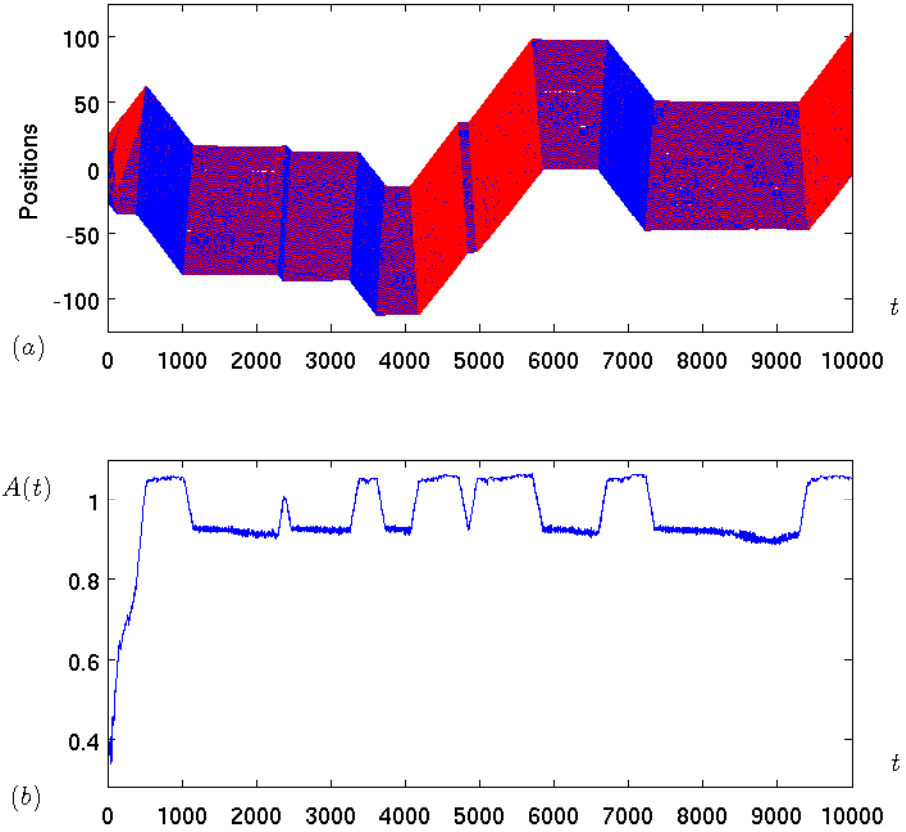


Figure 2.4: (a) Positions of  $N = 100$  fish for a  $10^4$  step run, with parameters:  $s = 0.75, \tau = 0.1, r_r = 1, \Delta r_o = 0.6, \Delta r_a = 1, p = 0.001$ , blue (resp., red) indicates an agent moving in the negative (resp., positive) direction. (b) Corresponding time series plot of the coarse variable  $A(t)$ , average distance to nearest neighbor.

the individual dynamics are driven by orientation and attraction, and the school coherently travels in the positive or negative direction. This is the one-dimensional analog of parallel motion. For certain values of the parameters we find “stick/slip” behavior in which the school alternates at apparently random times between the stationary and mobile state; such transitions arise from random fluctuations in the directions of individuals because of the stochasticity in the model. See Figure 2.4(a). In what follows, we focus primarily on parameters for which both the stationary and mobile states are metastable and the probability of fragmentation of more than a few individuals from the group is low.

### 2.2.1 Coarse Observable

Through simulations we are led to hypothesize that the dynamics of the model can be suitably characterized by a single coarse observable  $A(t)$ , the average nearest neighbor distance

$$A(t) = \frac{1}{N} \sum_{i=1}^N \min_{i \neq j} |c_j(t) - c_i(t)|. \quad (2.5)$$

This variable has been previously used in fish schooling models as a measure of the global structure of the school [45].  $A(t)$  can distinguish between the stationary and mobile states as long as the school is not fragmented into subgroups displaying different collective dynamics. When the system is in the stationary state, typically  $A(t) < r_r$  (repulsion driven), and when the system is in the mobile state, typically  $A(t) > r_r$  (orientation and attraction driven). Thus  $A(t)$  seems to capture the collective behavior of the school. See Figure 2.4(b). In Chapter 3 we will discuss

an automated, computer-assisted approach for the generation of appropriate coarse observables.

### 2.2.2 Computational Observations

For our simulations, we fix  $N = 100$ ,  $s = 0.75$ ,  $\tau = 0.1$ ,  $r_r = 1$ ,  $\Delta r_a = 1$ ,  $p = 0.001$ , and let  $\Delta r_o$  vary. For each value of  $\Delta r_o$  studied, data was taken from 100 runs lasting  $10^4$  steps. For  $\Delta r_o$  sufficiently small, the school remains in the stationary state for the duration of a simulation. As  $\Delta r_o$  is increased to approximately 0.14, the school exhibits stick/slip behavior in which it transitions at apparently random times between the stationary state and the mobile state. Transitions between these states typically begin with a stochastic change in direction of an agent at the edge of the school, which then “propagates” through the rest of the school, cf. [79, 88]. For  $\Delta r_o > 1.08$ , the school remains in the mobile state for the entire duration of the simulations.

Observing the steady-state probability distributions for various values of the parameter  $\Delta r_o$ , shown in the first column of Figure 2.5, one can see the signature of the transitions between the stationary and mobile state. The probability distribution peaks at approximately  $A = w_1 \equiv r_r - s\tau$ , corresponding to the stationary state, and at approximately  $A = w_2 \equiv r_r + s\tau$ , corresponding to the mobile state, a distance of approximately  $2s\tau$  from the stationary state. This may be rationalized by considering the dynamics of the stationary state, which is characterized by each agent typically changing its direction at every single time step to avoid its neigh-

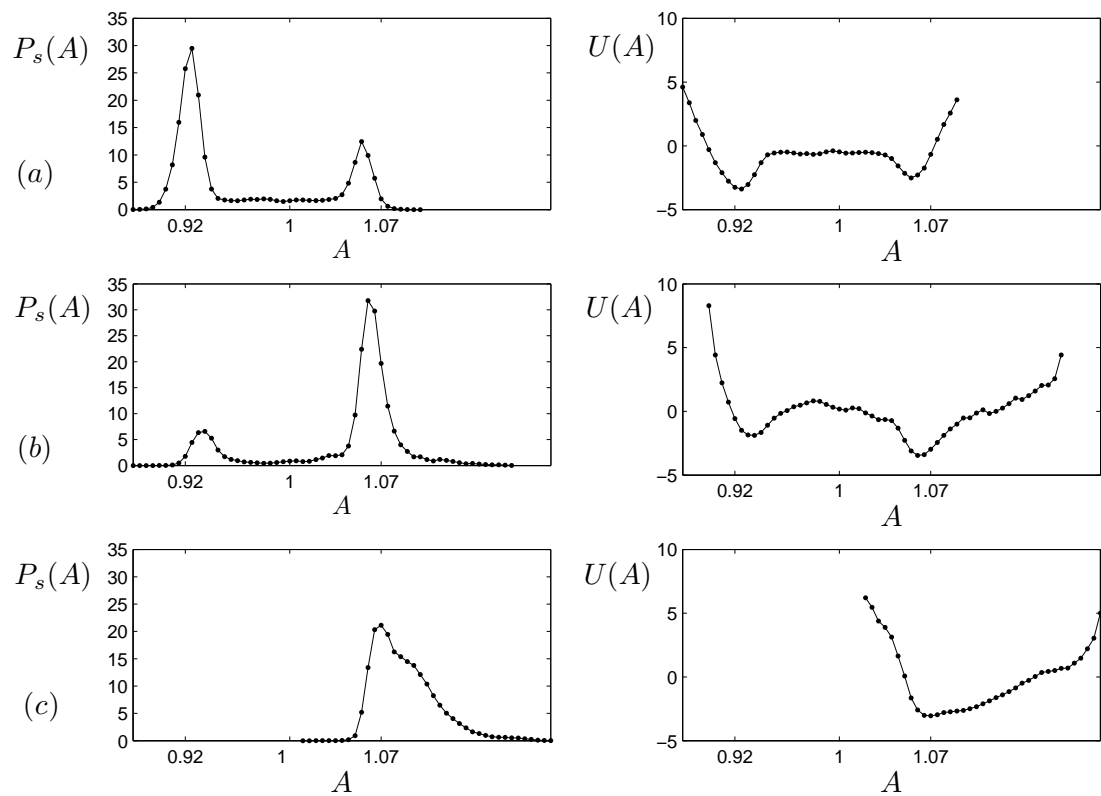


Figure 2.5: Probability distribution functions  $P_s(A)$  (left panel) and effective potentials  $U(A)$  (right panel) for 100 trials,  $10^4$  steps/trial,  $N = 100$ ,  $r_r = 1$ ,  $\Delta r_a = 1$ ,  $s = 0.75$ ,  $\tau = 0.1$ ,  $p = 0.001$ , (a)  $\Delta r_o = 0.6$ , (b)  $\Delta r_o = 1$ , (c)  $\Delta r_o = 1.1$ .

bor to the right or left, with  $A$  remaining nearly constant. Thus, one expects the individuals to be spaced approximately at alternating distances of  $d_1$  and  $d_2$  where  $d_1 < r_r$  and  $d_2 \approx d_1 + 2s\tau > r_r$ . When the group exhibits a transition from the stationary state to the mobile state, the distance  $d_2$  “propagates” throughout the school so that  $A \approx d_2$  in the mobile state.

In our simulations we find that the locations of the peaks of the stationary probability distribution depend somewhat on the details of the initial positions of the agents. This is a straightforward consequence of an important property of the model: in determining the desired direction of a given agent at the next time step, the only positional information used is which (if any) zone the other agents are in. Thus, agents can be moved slightly without changing their zones and hence with no change to the dynamics, but with a change to the value of  $A$ . These “neutrally stable” states have consequences for our lifting procedure described in Section 2.5.1.

## 2.3 Macroscopic Description

We assume that the system dynamics at the macroscopic level may be suitably characterized by our single coarse variable  $A(t)$ . We therefore consider describing the dynamics of  $A$  with an effective Langevin equation, or equivalently its probability distribution  $P(A, t)$  with an effective Fokker-Planck (FP), or forward Kolmogorov equation, cf. [40, 44, 54]:

$$\frac{\partial P(A, t)}{\partial t} = -\frac{\partial}{\partial A} [D^{(1)}(A)P(A, t)] + \frac{\partial^2}{\partial A^2} [D^{(2)}(A)P(A, t)], \quad (2.6)$$

where  $D^{(1)}(A)$  is the drift coefficient and  $D^{(2)}(A) > 0$  is the diffusion coefficient [13, 30, 92]. As derived in Appendix A, the drift  $D^{(1)}(A)$  and diffusion term  $D^{(2)}(A)$  are related to the short time evolution of the first two moments by

$$D^{(1)}(A_0) = \left. \frac{\partial \langle A(t; A_0) \rangle}{\partial t} \right|_{t=0}, \quad D^{(2)}(A_0) = \left. \frac{1}{2} \frac{\partial \text{Var}(t; A_0)}{\partial t} \right|_{t=0}, \quad (2.7)$$

where  $A(t; A_0)$  denotes a trajectory initialized at  $A_0$  at  $t = 0$ , angular brackets denote ensemble averaging over different realizations of the trajectory, and  $\text{Var}(A)$  denotes the variance of  $A$  for such an ensemble. The FP equation is equivalent to the Itô stochastic differential equation

$$dA = D^{(1)}(A)dt + \sqrt{2D^{(2)}(A)}dW, \quad (2.8)$$

with  $W(t)$  a Wiener process [30]. In the limit  $D^{(2)}(A) = 0$ , (2.8) describes the deterministic motion of  $A$  subject to the *effective potential*  $U_0(A) = -\int_{-\infty}^A D^{(1)}(A')dA' + \text{const.}$

In general, an effective potential  $U(A)$  can be obtained from the stationary probability distribution function  $P_s(A)$  which satisfies the steady state ( $\partial/\partial t = 0$ ) FP equation. Defining

$$P_s(A) \sim \exp(-U(A)), \quad (2.9)$$

it follows that  $U(A)$  satisfies

$$U(A) = \log(D^{(2)}(A)) - \int_{-\infty}^A \frac{D^{(1)}(A')}{D^{(2)}(A')} dA' + \text{const.} \quad (2.10)$$

When  $D^{(2)}(A) = \text{const.}$ , this corresponds to Brownian motion of  $A$  subject to an effective potential proportional to  $U_0(A)$ .

We will verify numerically that the assumptions inherent in using an effective Langevin and thus an effective FP equation are valid in Section 2.3.1. Expression (2.7) relates the drift and diffusion terms of the Fokker-Planck equation (2.6) to short-time statistical measures of the evolution of the coarse variable  $A$  initialized at a given value  $A_0$ . Techniques for consistently initializing a system at a given value of a coarse variable have been developed as part of the equation-free computational methodology [51]. These techniques will be discussed in more detail in Section 2.5. Once the effective FP equation is constructed, one may estimate global properties of the system such as the effective potential  $U(A)$  and transition rates between its metastable states. We first estimate the effective potential by compiling data from long-time simulations in Section 2.4. We then take advantage of formula (2.7) by developing a lifting procedure in Section 2.5.1. We use this lifting procedure to perform short bursts of appropriately initialized simulations that can be used to locally estimate coefficients in the effective Fokker-Planck equation.

### 2.3.1 Numerical Model Validation

We verify with numerical experiments that the assumptions of the effective Langevin equation are indeed satisfied for our coarse variable  $A(t)$ . If  $A(t)$  satisfies an effective Langevin equation (2.8), then its solution can be approximated to first order using the explicit Euler-Maruyama method as [53]

$$A(t) \approx A(t_0) + D^{(1)}(A(t_0))(t - t_0) + \sqrt{2D^{(2)}(A(t_0))}(W(t) - W(t_0)), \quad (2.11)$$

where  $W(t)$  is a Wiener process with  $W(t) - W(t_0) \sim N(0, t - t_0)$ . This means that over a short time interval, the solution to the Fokker-Planck equation, given an initial delta distribution at  $A(t_0) = A_0$ , will be approximately Gaussian with mean  $A_0 + D^{(1)}(A_0)(t - t_0)$  and finite variance  $2D^{(2)}(A_0)(t - t_0)$ . To verify this, we locate all appearances of  $A = A_0$  (within an error tolerance) in an ensemble of 100 runs of length  $10^4$  steps. We then select these instances to form an approximate delta distribution at  $A_0$  and track its evolution over a short time step. We find that for short times, the resulting distributions are approximately Gaussian with mean close to  $A_0$  and relatively small variance. Some results are shown in Figure 2.6(a) for  $A_0 = 0.95$  and are typical for all values of  $A_0$ .

Second, when modeling with an effective Fokker-Planck equation, it is assumed that the stochastic process is Markovian, or equivalently, the forcing term in the effective Langevin equation is white noise. It suffices to verify that the derivative of the fluctuation of  $A(t)$  about its mean,

$$\Lambda(t) \equiv \frac{d(A(t) - \langle A(t) \rangle)}{dt}, \quad (2.12)$$

has practically zero-correlation time [54]. We thus compute the (normalized) autocorrelation function of  $\Lambda(t)$  to verify this assumption. The time derivative in equation (2.12) is estimated using forward differences. We find that the autocorrelation function of  $\Lambda(t)$  is practically zero for  $t \neq 0$  and therefore conclude that our assumption that the process is Markovian is a valid one. Some results are shown in Figure 2.6(b) for an initial  $A_0 = 0.95$  and are typical for all values of  $A_0$ .

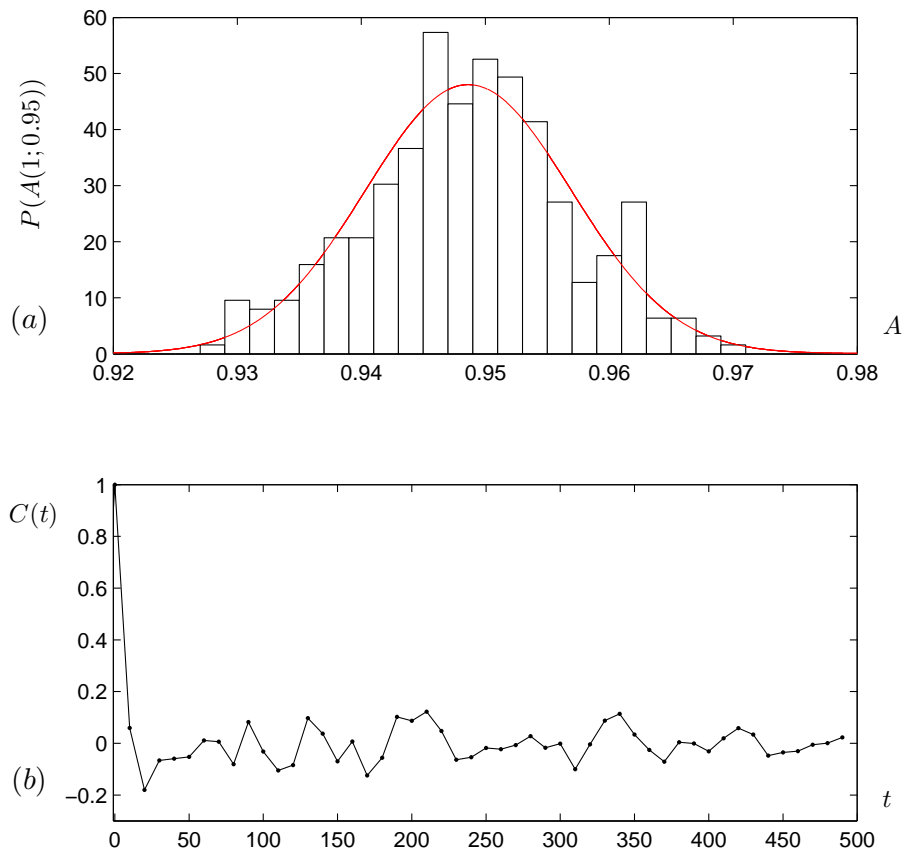


Figure 2.6: (a) Probability density function  $P(A(t; A_0))$  for  $A_0 = 0.95$ ,  $t = 1$ . Every appearance of  $A_0$  (within an error tolerance) in an ensemble of 100,  $10^4$  step simulations was recorded and its subsequent values saved over one time step. The probability density function was computed with an ensemble of 314 different data points. The red line shows the fit to a normal distribution. (b) (Normalized) autocorrelation function  $C(t)$  computed for  $A_0 = 0.95$  over a time interval of 500 steps. Both results are typical for all values of  $A_0$ .

## 2.4 Effective Potential: Long-Time Simulations

One may construct the effective potential in terms of the coarse variable  $A$  from long-time simulation data in one of two ways. The simplest approach is to obtain a steady-state probability distribution function  $P_s(A)$  directly from long-time simulation statistics and then use the relation  $U(A) = -\log(P_s(A)) + \text{const}$  to estimate the effective potential. This method is used in Figure 2.5 in which the probability distributions and corresponding effective potentials are shown for  $\Delta r_o = 0.6, 1.0, 1.1$ . In each case, a database was obtained from one hundred  $10^4$  step simulations, with the first 1000 steps discarded. As one can see from the figure, for  $\Delta r_o = 0.6$ , the model has two metastable states, the stationary state at  $A \approx 0.925$  and the mobile state at  $A \approx 1.055$ . The school exhibits stochasticity-induced switching between these states, spending more time in the stationary than in the mobile state on average. For  $\Delta r_o = 1.0$ , the model has the same two metastable states, but spends more time in the mobile than the stationary state on average. While, for  $\Delta r_o = 1.1$ , the school spends its time in the mobile state for the duration of a simulation. This suggests there is a *coarse bifurcation*, or a qualitative change in the collective dynamics of the system, as the parameter  $\Delta r_o$  is varied. The precise parametric dependencies of the system on the parameter  $\Delta r_o$  will be investigated in Section 2.7 by locating the local maximum and minima of the effective potential.

Alternatively, one may estimate the effective potential by compiling enough statistics from a long-time simulation database to estimate the drift and diffusion

terms using (2.7). More specifically,  $A$  is discretized over a grid of values that appear in the database:  $A_0 = 0.88 + mk$ ,  $m = 0.005$  (mesh size),  $k = 0, 1, \dots, 42$  for  $\Delta r_o = 0.6$ . Then, for each  $A_0$  over the grid,  $D^{(1)}(A_0)$  and  $D^{(2)}(A_0)$  are approximated using (2.7) as follows. Every appearance of  $A_0$  (within a certain error tolerance) as well as its subsequent values over a short fixed time interval of length  $t = 10$  steps are saved. The ensemble mean  $\langle A(t; A_0) \rangle$  and variance  $\text{Var}(t; A_0)$  are then estimated by averaging over these short trajectories. The drift (resp., diffusion) term,  $D^{(1)}(A_0)$  (resp.,  $D^{(2)}(A_0)$ ), are estimated by computing the slope of the linear regression of  $\langle A(t; A_0) \rangle$  (resp.,  $\text{Var}(t; A_0)$ ). Better fitting techniques like maximum likelihood estimation [1] could be used to estimate these quantities, but the method described above was found to be sufficient. Finally, the integral in expression (2.10) is numerically approximated using rectangles and the effective potential  $U(A)$  is estimated over the grid of  $A$  values using expression (2.10).

Figure 2.7 shows for  $\Delta r_o = 0.6$ , estimates of the drift, diffusion, and effective potential as a function of  $A$ , the latter of which was estimated using both approaches. The drift term,  $D^{(1)}(A)$ , is close to zero at the local minima (wells) (e.g.,  $\Delta r_o = 0.925, 1.055$ ) and at our estimation for the local maximum (i.e.,  $\Delta r_o = 0.995$ ). The drift term is positive near the left of each well and negative near the right of each well. Thus, there is an effective force pushing  $A$  towards the local minima of the effective potential which are the stable steady-states of the corresponding deterministic system and away from the local maximum (saddle point) which is an unstable steady-state of the corresponding deterministic system.

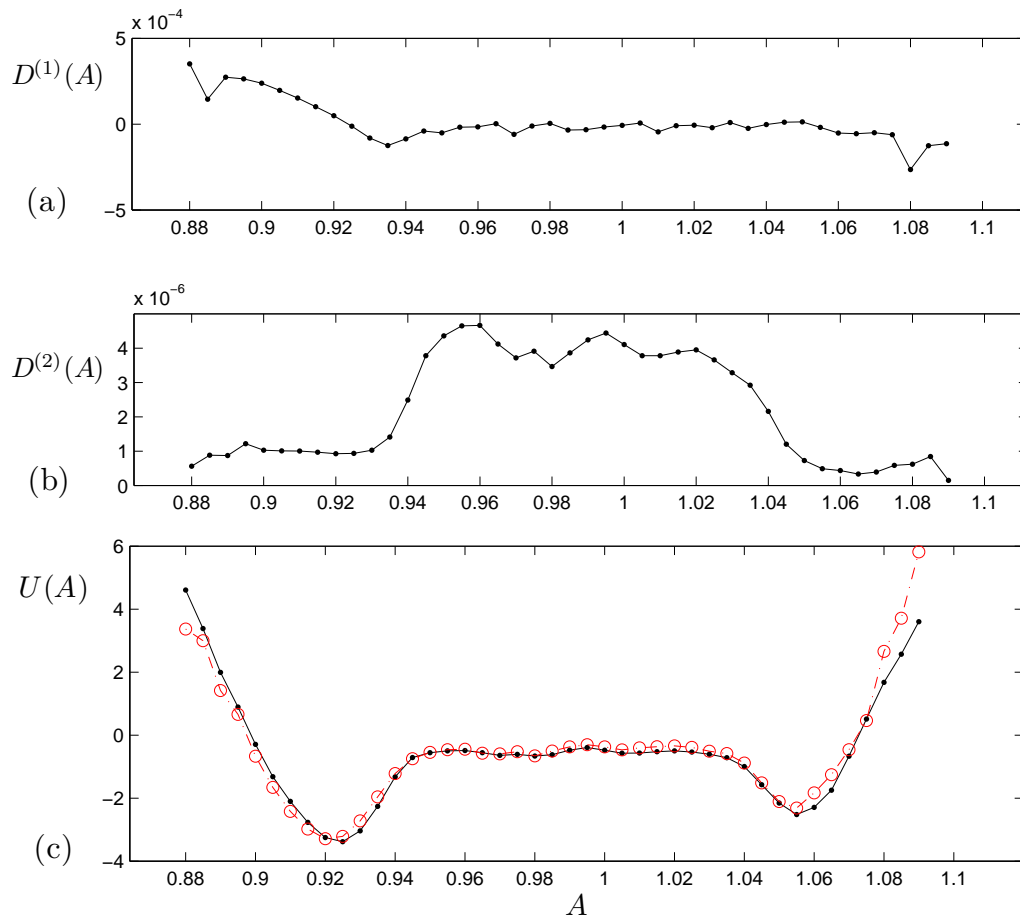


Figure 2.7: Estimate of  $D^{(1)}(A)$ ,  $D^{(2)}(A)$ , and  $U(A)$  for  $\Delta r_o = 0.6$  using long-time simulation data. (a) Estimation of  $D^{(1)}(A)$ , (b) Estimation of  $D^{(2)}(A)$ , and (c) Estimation of  $U(A)$  using (black)  $U(A) = -\log(P_s(A))$  and (red) equation (2.10).

The effective potential obtained using the second approach agrees quite well with that obtained using the first approach, which confirms that  $A$  is a dynamically meaningful observable. Both methods, however, do not offer any computational savings since we had to compile data from sufficiently extensive temporal simulations (an “equilibrium run”), which takes approximately 10 hours for 100,  $10^4$  step trials running with Matlab on a standard workstation. Instead, one can use the lifting procedure of the “equation-free” methodology of Kevrekidis and coworkers [51] to estimate  $D^{(1)}(A)$  and  $D^{(2)}(A)$  by using appropriately initialized short-time integrations of the individual based model.

## 2.5 Effective Potential: Short-Time Simulations

Recently, Kevrekidis *et al.* [51] have developed an “equation-free” computational framework for extracting population-level information from individual-based models; the term “equation-free” arises because the population-level equations are not explicitly known. The approach relies on the assumption that the system state variables can be decomposed into a subset of fast variables and a low-dimensional subset of slow variables, which parameterize an attracting invariant slow manifold. If a simulation is appropriately initialized at a prescribed value of the slow variables, say  $X_0$ , then after a short time, once all of the fast variables have equilibrated, one will in effect sample the slow manifold at  $X_0$ . This framework can be used to efficiently estimate on demand (without long-time simulation) the drift and diffusion terms in the effective FP equation [44, 54].

Note that one does not need to have knowledge of the slow and fast variables to use the “equation-free” framework. It suffices to identify a set of coarse observables that parameterize the slow manifold. However, if the hyperplane corresponding to these observables is not approximately orthogonal to the fast flow, then integrating the system to the slow manifold may significantly change the initial value of the observables, especially when initial conditions are far from the slow manifold [32].

As an example, consider the planar system

$$\begin{aligned} \dot{u} &= \frac{1}{\epsilon}v - 1, \\ \dot{v} &= \frac{1}{\epsilon}v + 1 \end{aligned} \tag{2.13}$$

with  $0 < \epsilon \ll 1$ . Making the coordinate transformation  $x = (u-v)/2$ ,  $y = (u+v)/2$ , system (2.14) reduces to singular perturbation form:

$$\begin{aligned} \dot{x} &= -1, \\ \epsilon \dot{y} &= x - y \end{aligned} \tag{2.14}$$

where  $x$  is the “slow variable” and  $y$  is the “fast variable”. Solutions starting off the slow manifold  $x = y$  quickly approach it, keeping approximately the same initial value of the slow variable  $x$ . In  $(u, v)$  coordinates, one may treat  $u$  as a coarse observable, with the slow manifold being parameterized by the equation  $v = 0$ . In this case, however, the initial  $u$ -value changes significantly as trajectories collapse down to the slow manifold. See Figure 2.8. If a simulation is initialized in  $(u, v)$  coordinates at say,  $(0, v_0)$  for some  $v_0 > 0$ , then after a short time it will arrive on the slow manifold but far from the value of the coarse observable  $u = 0$  it was

initialized at.

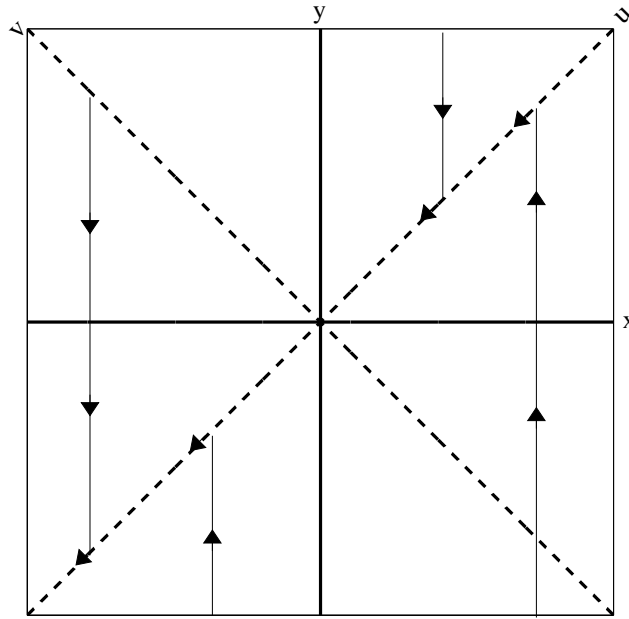


Figure 2.8: Trajectories approach the slow manifold  $x = y$ . In  $(x, y)$  coordinates, solutions maintain their initial  $x$ -value as they approach the slow manifold, while in  $(u, v)$  coordinates they do not.

In order to put the equation-free coarse-grained computational framework to use for the schooling model, one must identify an appropriate set of coarse observables, and develop a *lifting* algorithm, that is, a method for constructing fine scale states “consistent with” the prescribed value of the coarse observables that are “mature”, that is, close to the slow manifold. We discuss both aspects of this with regards to the fish schooling model below.

As discussed in section 2.2.1, we found  $A$  to be an appropriate coarse observable. Although  $A(t)$  distinguishes between the two collective states the school displays, one might also consider using the average heading of all individuals within the

school, group polarization, as a coarse observable. More formally we define *group polarization* as

$$S(t) = \frac{1}{N} \left| \sum_{i=1}^N v_i(t) \right|. \quad (2.15)$$

$S(t)$  has been used in many fish schooling models as a measure of school structure [19, 45]. When  $S(t) \approx 1$ , the school is mobile and when  $S(t) \approx 0$ , the school is stationary. Thus  $S(t)$  seems to be another good candidate for a coarse observable.

In Figure 2.9 we show the long-term dynamics of the system in the  $(A, S)$  plane. The data collapses on an approximately one-dimensional manifold, which justifies our selection of  $A$  as a coarse observable. Here, data was taken from an ensemble of five  $10^4$  step simulations after steady-state was reached ( $\approx 10^3$  steps) for  $\Delta r_o = 0.6$ .

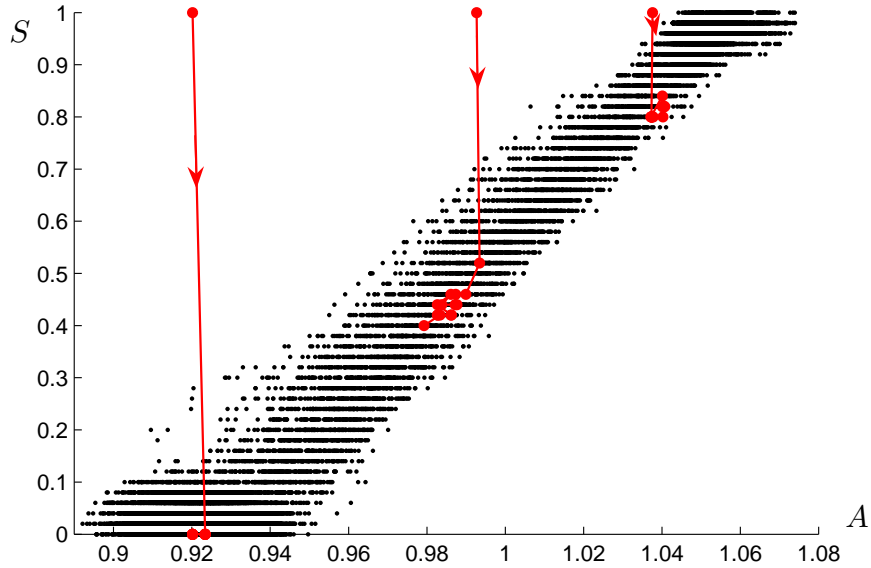


Figure 2.9: (Black) Computational evidence for a slow manifold in the  $A, S$  plane. Data was taken from an ensemble of 5,  $10^4$  step simulations after steady state was reached (approx. 1000 steps) for  $\Delta r_o = 0.6$ . (Red) Sample trajectories are initialized using the lifting algorithm described in Section 2.5.1 and evolve for 15 steps. After a short time, trajectories approach an apparent slow manifold. Arrows show the direction of increasing time.

In addition, we find that under appropriate conditions,  $S(t)$  becomes slaved under the dynamics of the system to  $A(t)$ . Recall that when the school is in the stationary state, the dynamics are driven by repulsion and the directions are updated according to rule (2.1). In this case, if individuals are placed a repulsion distance away from their nearest neighbors, then no matter how their directions are initialized, after just one time step, the directions will settle to the appropriate values. This is because rule (2.1) is entirely based on positional information. Note that it is important to place individuals greater than a repulsion distance away from their second nearest neighbors so that the repulsion contributions do not balance out.

If however, individuals are placed in the mobile state and given random directions, a large separation of time scales no longer persists. After a relatively short time, the system finds itself on the “slow manifold”, but far from the value of  $A$  for which it was initialized at. This is because rule (2.2) mixes both positional (attraction) and directional (orientation) information. One may apply techniques to constrain the dynamics of the system in order to arrive on the “slow manifold” at the appropriate value of  $A_0$  [32, 70]. Instead, we find that simply initializing the directions to be all the same, i.e, taking  $S = 1$ , puts the system sufficiently close to the slow manifold when initializing  $A$  in the mobile state.

For intermediate values of  $A$ , portions of the school obey rule (2.1), while other portions obey (2.2). Since heading information is not taken into account when the dynamics are repulsion driven (2.1), we are free to initialize headings as we desire

without changing the dynamics. We therefore simply initialize all individuals with the same direction, i.e., we take  $S = 1$ . By initializing with  $S = 1$ , the time scale of approach to the “slow manifold” is comparable for the entire school whether members are obeying rule (2.1) or rule (2.2).

Because of the “neutrally stable” states mentioned in Section 2.2.2, to equilibrate to the desired slow manifold we must take care when placing agents at a given value of  $A_0$ . From these computations, we found that the distribution of distances between individuals in the stick/slip state is bimodal, with peaks at  $w_1 = r_r - s\tau$ ,  $w_2 = r_r + s\tau$ , a distance of  $2s\tau$  from each other. We use this information in our lifting algorithm to place individuals at a given  $A_0$ .

### 2.5.1 Lifting Algorithm

The procedure to initialize the positions and directions of  $N$  individuals with a given average distance to nearest neighbors,  $A_0$ , is as follows:

1. Calculate proportions  $p_1$  and  $p_2$  of distances  $w_1$  and  $w_2$  so that  $p_1w_1 + p_2w_2 = A_0$ . If  $A_0 < w_1$ , set  $w_1 = A_0$  and if  $A_0 > w_2$ , set  $w_2 = A_0$ .
2. Draw the appropriate proportion  $p_1$  and  $p_2$  of distances to first nearest neighbors from tight Gaussian distributions centered at  $w_1$  and  $w_2$ . Place them randomly in the vector  $d_1$ .
3. Draw distances to second nearest neighbors from a tight Gaussian distribution centered at  $w_2$ . Place them randomly in the vector  $d_2$ .

4. Start the first agent at some position  $c_1$  on the line. Place the second agent at position  $c_2 = c_1 + d_1(1)$ . Place the third agent at position  $c_3 = c_2 + d_2(1)$ . Place the fourth agent at position  $c_4 = c_3 + d_1(2)$ . Continue this process until there are  $N$  agents positioned.
5. Let  $v_i = 1, \forall i$ .

To validate this procedure we consider the coarse dynamics in the  $(A, S)$  plane; see Figure 2.9. Our lifting algorithm initializes the population with  $S = 1$ , and the time scale of approach to the slow manifold is comparable whether  $A_0 > r_r$  or  $A_0 < r_r$ . The quick relaxation to the slow manifold for  $A_0 < r_r$  occurs because rule (2.1) causes the agents to try to immediately move away from each other.

## 2.5.2 Results

One may proceed to estimate the drift and diffusion coefficients as described in Section 2.4 and obtain an estimate for the effective potential. More specifically, for each  $A_0$  over the mesh, an ensemble of 1000 simulations was initialized at  $A_0$  using the lifting procedure and then integrated for a short 50 time steps. The drift  $D^{(1)}(A)$  (resp., diffusion  $D^{(2)}(A)$ ) terms were then estimated after waiting a short healing time of 15 steps by computing the slope of the linear regression of the mean (resp., variance) of the simulation statistics over the time interval  $[15, 45]$ . Finally, the effective potential  $U(A)$  was estimated using equation (2.10). The effective potential obtained using the short-time simulation statistics is in good agreement with that obtained from long-time simulation statistics and requires approximately

a factor of 5 less computation. See Figure 2.10 for a comparison of the effective potentials. The procedure does not approximate the depth of the mobile well as accurately as that of the stationary well. Additional degrees of freedom may therefore be required for full characterization, degrees whose time scales are not well separated from  $A(t)$ .

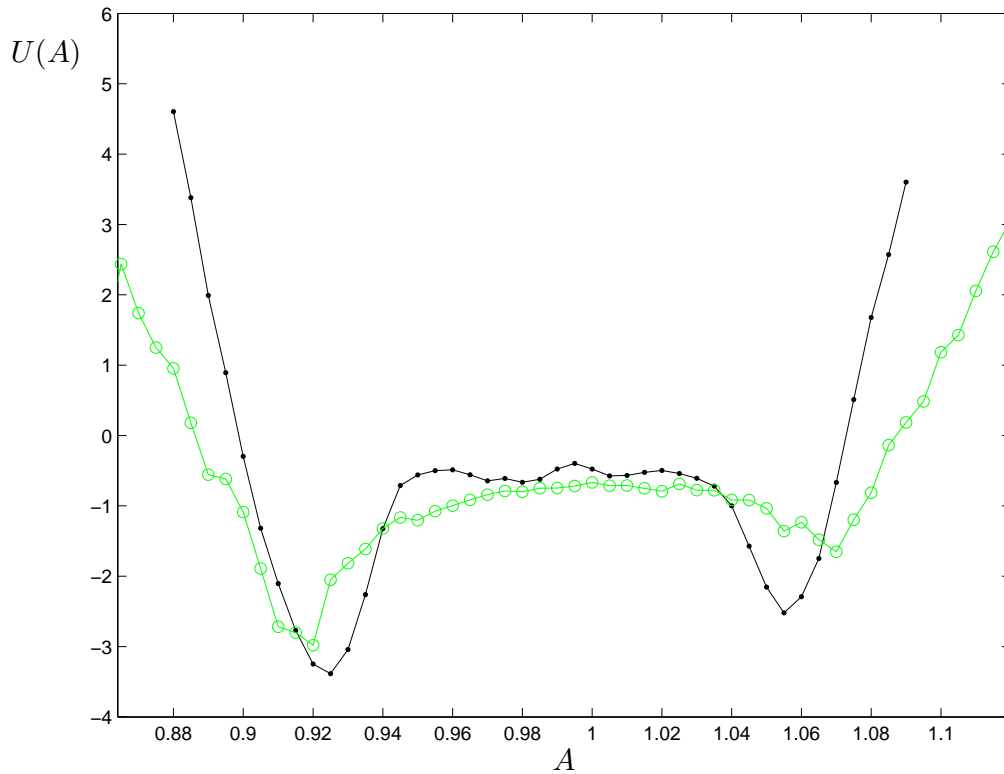


Figure 2.10: Estimates of the effective potential  $U(A)$  for the system when  $\Delta r_o = 0.6$ . The effective potential was estimated (black) using a long-time simulation database and the relation  $U(A) = -\log(P_s(A))$  and (green) using the lifting procedure to initialize short-bursts of simulation and estimating  $D^{(1)}(A)$ ,  $D^{(2)}(A)$ , and  $U(A)$  using equations (2.7) and (2.10).

## 2.6 Mean Residence Times

Now that we have associated the dynamics of our system with an effective potential, we may ask how long the system on average stays in either the stationary or mobile state. We first compute the mean residence times in the stationary and mobile state by taking data from an ensemble of long-time simulations and averaging over the time spent in each well. For the parameter  $\Delta r_o = 0.6$  these times were found to be 994 for the stationary well and 509 for the mobile well. The distribution of times is exponential as predicted from Kramers theory [30, 41]; see Figure 2.11.

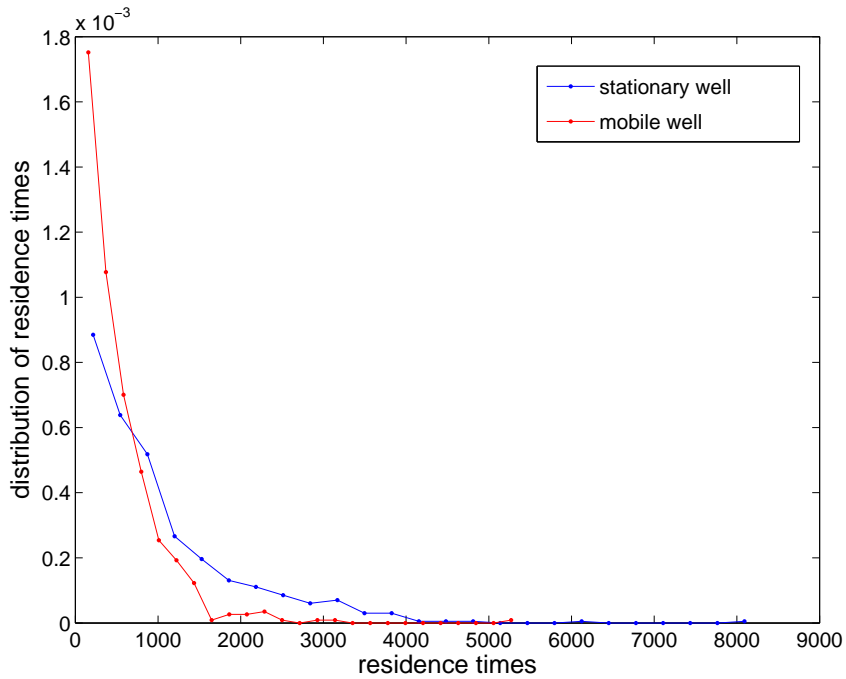


Figure 2.11: Probability distribution of residence times in the stationary well (blue) and mobile well (red) for  $\Delta r_o = 0.6$ . The probability distributions were formed by estimating the times spent in each well over a period of  $10^4$  steps in an ensemble of 100 runs.

We can use Kramers Formula (see the derivation in Appendix B) to estimate

the mean residence times in each well. If  $D^{(2)}(X)$  is relatively small, the average time  $T$  spent in a well located at  $X = X_{min}$  is approximated by [30]

$$T \approx \frac{2\pi \exp(\Delta U)}{\overline{D} \sqrt{-U''(X_{min})U''(X_{max})}}, \quad (2.16)$$

where  $X = X_{max}$  is the location of the local maximum (saddle point) of the potential  $U$ ,  $X_{min}$  is the location of the local minimum,  $\overline{D} = \frac{1}{2} (D^{(2)}(X_{max}) + D^{(2)}(X_{min}))$ , and  $\Delta U = U(X_{max}) - U(X_{min})$ .

For  $\Delta r_o = 0.6$  the mean residence times were estimated to be  $T = 1060$  for the stationary well and  $T = 505$  for the mobile well. A central difference approximation was used to estimate the derivatives in (2.16). These times are quite close to the empirically estimated times calculated from long-time steady state runs. The lifting procedure produced average residence times of approximately 640 for the left well and 217 for the right well for  $\Delta r_o = 0.6$ . These times are a bit smaller than the residence times estimated from long-time simulation data. The ratio of times  $r = 640/217 \approx 2.95$  is larger than the ratio estimated from long-time data which is approximately  $r = 994/509 \approx 1.95$ . This is consistent with the fact that the depth of the second well of the potential obtained from the lifting procedure is not as large as the depth obtained by using long-time simulation data and indicates that additional coordinates may be needed for full specification.

## 2.7 Coarse Bifurcation Diagrams

To study the dependence of the behavior of the system on parameters, the critical points of the effective potential were followed as  $\Delta r_o$  was varied. This is a useful practical analog of deterministic bifurcation diagrams for this stochastic case. The minima of the effective potential correspond to points on the stable branch of the bifurcation diagram and the maxima correspond to points on the unstable branch. To filter the spurious minima and maxima which may arise due to school fragmentation, we perform a quadratic fit of the effective potential between the two prominent wells. The coarse bifurcation diagrams obtained using estimates of the effective potential formed from both long- and appropriately initialized short-time simulation statistics are shown in Figure 2.12. The diagrams compare well quantitatively and qualitatively with each other. Two saddle node bifurcations are found at approximately  $\Delta r_o = 0.14$  and  $\Delta r_o = 1.09$  and the system appears bistable for values of  $\Delta r_o$  within this range.

## 2.8 Conclusion

The individual-based stochastic model of self-organizing group formation analyzed in this chapter shows that animal groups can switch between qualitatively different collective motion states due entirely to stochastic effects. In particular, changes to behavioral rules or the environment are *not* necessary for such transitions to occur. This mechanism relies on the presence of at least two metastable

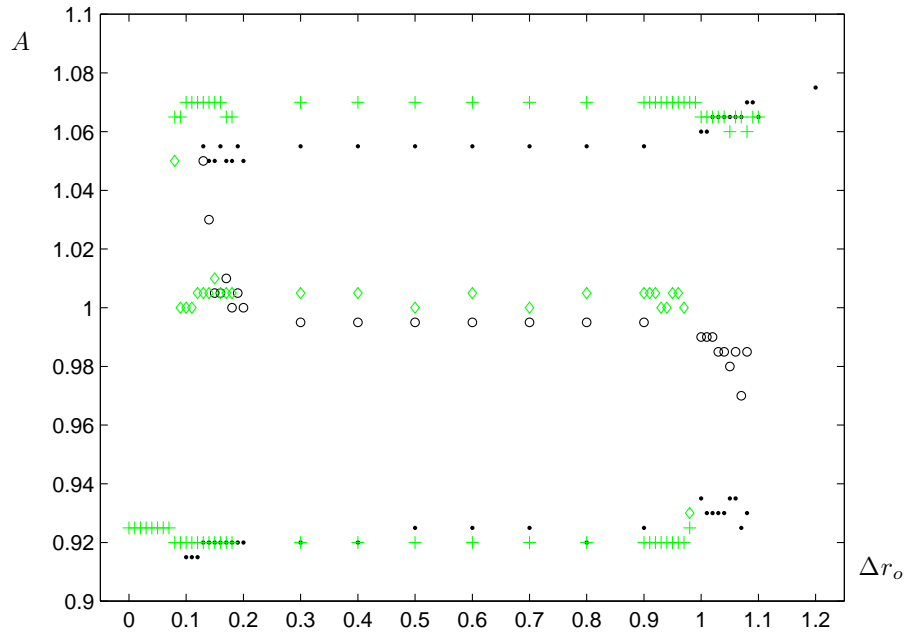


Figure 2.12: Coarse-grained bifurcation diagram showing the critical points of the effective potential as  $\Delta r_o$  is varied. The minima of the effective potential correspond to the stable branch (dot, plus) and the maxima correspond to the unstable branch (circle, diamond). (Black) An ensemble of 100,  $10^4$  step runs is used to estimate the stationary probability distribution  $P_s(A)$  and the corresponding effective potential  $U(A) = -\log(P_s(A))$ . (Green) The lifting procedure is used to initialize short bursts of simulations to estimate the drift and diffusion terms in the FP equation. In both cases, the unstable solutions were located by performing a quadratic fit of the data between the two wells and then locating the maxima of the fit.

collective motion states, and stochasticity of appropriate type and strength to allow transitions to occur.

Because the stochasticity that leads to switching is imposed at the level of individuals, this analysis suggests that random decisions by a small number of individuals can change an entire population’s collective behavior, in particular when these individuals are near the edge of the school. This complements recent simulations for a related model which indicate that a small number of *informed* individuals can influence group dynamics [18]. One can imagine that a combination of these effects might also be important: for example, a small number of individuals might spot a predator and quickly, randomly change their directions, an “informed stochasticity”, which leads to a change in the entire group’s motion, which could allow all individuals to escape (cf. [46]). In Chapter 6, we will investigate the relationship between spatial position and information transfer in two-dimensional schools.

We have developed a useful coarse-grained, computer-assisted framework for the analysis of such stochasticity-induced switching. We characterize switching at the macroscopic level with a single coarse observable  $A(t)$ , average distance to nearest neighbor, whose dynamics are described by an effective Fokker-Planck equation. The construction of effective potentials from long- as well as short-time simulation statistics allows us to locate metastable collective states, and their parametric dependence, as well as estimate mean residence times. The use of appropriately initialized short-time simulation statistics, made possible with the lifting algorithm, allows us to obtain estimates of mean residence times without having to observe

them from long-time simulation data. This allows us to gain *a priori* estimates of the length of time a school will display a particular collective behavior before transitioning into another. This is especially useful when such times are too large to practically estimate from long-time equilibrium simulations.

# Chapter 3

## Coarse Analysis of Collective Motion with Different Communication Mechanisms

### 3.1 Introduction

In the schooling model studied in Chapter 2, it was assumed that individuals are able to communicate with *all* neighbors within their behavioral zones, regardless if they are ahead or behind of them, or facing towards or away from them. For many animal groups, however, it is realistic to assume that individuals may only receive some signals unidirectionally [86, 97, 106]. This might be due to many factors including their physiology, behavioral preferences, or environmental conditions [26, 63]. Most organisms, for example, have a limited field of vision, and

neighbors in their “blind spot” are visually undetectable. In the presence of predators, birds may use directional sound cues to prevent receivers other than the addressee from obtaining information [106]. As in [25], for which different animal communication mechanisms were explored for a one-dimensional hyperbolic partial differential equation model for group formation, here we compare the effects of a change in the communication protocol on the individual-based schooling model. More specifically, we consider the case that individuals receive repulsion and attraction signals omnidirectionally but only orient with those facing towards them (this is called mechanism M1 in [25]). In this chapter, we demonstrate how this signalling constraint affects the properties of collective motion.

The average distance to the nearest neighbor was used as a coarse variable in Chapter 2 to characterize the collective behavior of the school. This was shown to be a dynamically meaningful observable through computational experiments to test possible candidate observables. However, as pointed out in Chapter 2, the value of this coarse variable can depend on details of the positions of the individuals which do not affect the dynamics; this is a consequence of the fact that the only positional information used to determine the dynamics for a given individual is which zone other individuals are in, and can be viewed as a “neutral stability” property of solutions to the model.

In the present chapter, we will instead use an automated data-driven technique for generating coordinates that correlate with the collective behavior of the school. First, we will construct the normalized graph Laplacian by interpreting a sample

simulation dataset as a graph whose connection strengths are given by a Gaussian kernel [6]. Using the framework developed in [14], we then construct “diffusion map” coordinates from the eigenvectors of this matrix and use them to provide a geometrically meaningful lower-dimensional representation of the dataset. The advantage of using such an approach over more classical methods such as principal component analysis is that it is nonlinear and preserves local data structures [48]. Further motivation for using diffusion maps as reaction coordinates for stochastic dynamical systems can be found in [72]. The diffusion map framework allows us to find a low dimensional representation of the dynamics of the schooling model. Specifically, we will show that a single diffusion map coordinate is, in our case, sufficient to characterize the dynamics. This coordinate also overcomes the “neutral stability” issue which arose for the coarse variable used in Chapter 2. We will compute a probability distribution as a function of this coordinate. An effective potential is formed from this probability distribution and used to locate metastable states, their parametric dependencies, and estimate mean residence times as in Chapter 2. Coarse bifurcation diagrams are constructed for each of the models and compared to quantify the effects of the signalling constraint on the collective dynamics.

## 3.2 The Model

We consider the same one-dimensional individual-based model schooling model that was studied in Chapter 2, which incorporates a tendency for each agent to align

its position and orientation with an appropriate average of its neighbors' positions and orientations, plus a tendency for each agent to avoid collisions. In this model, agents are able to communicate with all neighbors within their behavioral zones, regardless of their relative positions or orientations. Here, we consider a *constrained* signalling model, for which agents receive repulsion and attraction signals omnidirectionally but are only able to align with those in their zone of orientation that are facing towards them. In this case, the summation index in the orientation contribution  $o_i(t)$  in equation (2.3) is changed to  $\{c_j(t) \in Z_{o_i}(t) \mid v_j(t) \frac{c_j(t) - c_i(t)}{|c_j(t) - c_i(t)|} = -1\}$ .

For the parameters studied in Chapter 2, namely  $N = 100$ ,  $s = 0.75$ ,  $\tau = 0.1$ ,  $r_r = 1$ ,  $0.1 < \Delta r_o < 1.3$ ,  $\Delta r_a = 1$ ,  $p = 0.001$ , we observe that both models, each with a different communication rule, can display the two metastable collective states described in Chapter 2, a “stationary state”, in which the dynamics are driven by repulsion, and a “mobile state”, in which the school is aligned and travels in the positive or negative direction. Both models exhibit stochasticity-induced switching between the stationary and mobile state for certain values of the parameters. For the signal constrained model, the mobile state only exists for higher values of  $\Delta r_o$ ; a detailed bifurcation analysis will be performed later in the chapter to quantify this more precisely.

## 3.3 Diffusion maps: data-driven detection of coarse observables

### 3.3.1 Background

For many complex biological systems, it is often quite difficult to identify appropriate coarse variables, “observables”, or “reaction-coordinates” that correlate with the population-level behavior of the system and capture its geometric structure. In addition, often such systems have many degrees of freedom and it is useful to explore methods for reducing their dimensionality. Here we summarize a data-mining technique for obtaining a low-dimensional representation of a high-dimensional dataset [14, 71, 72], and show how it can be applied to find an appropriate coarse observable for our schooling models. This technique has been successfully applied to models in systems biology and neuroscience [27, 59].

### 3.3.2 Diffusion Map Theory

Suppose  $\{X^{(i)}\}_{i=1}^m$  is a finite dataset with each  $X^{(i)} \in \mathbb{R}^N$ . A random walk may be defined on the graph of the dataset as follows [71]. Points in the dataset correspond to nodes of a graph with connection strength given by a Gaussian kernel. (In [14], anisotropic kernels formed from renormalizing the Gaussian kernel were also explored.) Applying the graph Laplacian normalization [6] to the kernel, one may form a Markov (row stochastic) matrix  $M$ . With this framework, one can quantify the similarity between datapoints, the “diffusion distance”, by comparing

the probability distributions of random walks starting at the nodes of the graph. A “diffusion map”, which maps datapoints to their eigencomponents in diffusion map space, is constructed from the first  $k$  eigenvectors of  $M$ . It was proved in [71] that diffusion distance is equal to Euclidean distance in diffusion map space. Thus, datapoints that are close together in diffusion distance are mapped to points close together in Euclidean distance. In addition, if  $M$  has a spectral gap, it was shown that a  $k < N$  dimensional approximation is optimal under a certain mean squared error criterion.

Asymptotic analysis has also shown that for datasets sampled from an underlying probability distribution, written in Boltzmann form as  $p(x) = e^{-U(x)}$ , in the limit that the sample size  $m \rightarrow \infty$  and the standard deviation of the kernel  $\sigma \rightarrow 0$ , the random walk on the graph converges to a diffusion process which can be described by a Fokker-Planck equation [71]. Different normalizations of the Gaussian kernel were shown to produce different differential operators [72]. In particular, for the isotropic Gaussian kernel, the eigenvalues and eigenvectors of  $M$  are discrete approximations to the eigenvalues and eigenfunctions of the Fokker-Planck operator with potential  $2U(X)$ . In the case that  $U(X)$  (and thus  $2U(X)$ ) has two wells separated by a large barrier (i.e., the dataset has two well-separated clusters), then the diffusion map approach can identify a single coarse observable, the first non-trivial (second principal) eigenvector, whose components parametrize the dataset.

### 3.3.3 Diffusion Map Coordinates and Nyström extension

We now review the procedure for computing diffusion map coordinates for a dataset, including the use of the Nyström extension to obtain diffusion map coordinates for points outside the dataset. (See [59] for an example of this approach applied to a neural field model.) Let  $\{X^{(i)} \in \mathbb{R}^N\}_{i=1}^m$  be a finite dataset with distance measure  $d : \mathbb{R}^N \times \mathbb{R}^N \rightarrow \mathbb{R}$ . For our model, this corresponds to snapshots of the school taken from a representative steady state simulation. Next, define the Gaussian kernel  $K(X^{(i)}, X^{(j)}) = \exp\{-[d(X^{(i)}, X^{(j)})]^2/\sigma^2\}$  and its corresponding matrix representation  $K_{i,j} = K(X^{(i)}, X^{(j)})$ . Let  $D_{i,i} = \sum_{j=1}^m K_{i,j}$  be the diagonal matrix formed from the row sums of  $K$ . Then, the Markov (row stochastic) matrix  $M = D^{-1}K$  defines a random walk on a graph whose nodes correspond to the points in the dataset. The entries  $M_{i,j}$  can be interpreted as representing the probability of transition from  $X^{(i)}$  to  $X^{(j)}$  in the time  $\Delta t = \sigma$  [71].

Define the symmetric matrix  $M_s = D^{1/2}MD^{-1/2}$ . Note that  $M$  is related to  $M_s$  through a similarity transformation, so they share the same eigenvalues. Since  $M_s$  is symmetric, it is diagonalizable, and its eigenvectors  $\{\Psi_j\}_{j=1}^m$  form an orthonormal basis of  $\mathbb{R}^m$ . Let  $\{\lambda_j\}_{j=1}^m$  be the corresponding (real) eigenvalues of  $M_s$  and  $M$ . Then the eigenvectors  $\{\Phi_j\}_{j=1}^m$  of  $M$  are related to those of  $M_s$  by the relation  $\Phi_j = D^{-1/2}\Psi_j$ . For  $\sigma$  large enough, all points are connected ( $M$  is strictly positive) and it follows from the Perron-Frobenius Theorem [66] that  $\lambda_1 = 1$  is a unique eigenvalue with corresponding eigenvector  $\Phi_1 = [1, 1, \dots]$  and  $1 > \lambda_2 \geq \lambda_3 \geq \lambda_4 \geq$

...  $\lambda_m \geq 0$ . The diffusion map  $f : \mathbb{R}^N \rightarrow \mathbb{R}^k$  is defined as

$$f : X^{(i)} \rightarrow (\Phi_2^{(i)}, \Phi_3^{(i)}, \dots, \Phi_{k+1}^{(i)}), \quad (3.1)$$

where an appropriate  $k$  is chosen based on the spectral gap. Here  $k$  is the number of non-trivial eigenvalues clustered near one with all additional eigenvalues close to zero. The notation  $\Phi_k^{(i)}$  represents the  $i^{\text{th}}$  component of the  $k^{\text{th}}$  eigenvector. In practice, we compute the eigenvalues and eigenvectors of  $M_s$  and then use the relation  $\Phi_j = D^{-1/2}\Psi_j$  to find the eigenvectors of  $M$ .

We now discuss how to compute the diffusion map coordinates for points outside of our dataset. By definition, the eigenvectors  $\Psi_j$  of  $M_s$  satisfy the following equation

$$\Psi_j^{(k)} = \frac{1}{\lambda_j} \sum_{i=1}^m M_s(X^{(k)}, X^{(i)}) \Psi_j^{(i)}. \quad (3.2)$$

Here  $M_s = D^{-1/2} K D^{-1/2}$ , so that the component

$$(M_s)_{k,i} \equiv M_s(X^{(k)}, X^{(i)}) = \frac{K(X^{(k)}, X^{(i)})}{\sqrt{\sum_{j=1}^m K(X^{(k)}, X^{(j)}) \sum_{j=1}^m K(X^{(i)}, X^{(j)})}}. \quad (3.3)$$

The eigenvectors  $\Phi_j$  of  $M$  satisfy

$$\Phi_j^{(k)} = \frac{1}{\sqrt{D_{k,k}}} \Psi_j^{(k)} = \frac{1}{\sqrt{\sum_{j=1}^m K(X^{(k)}, X^{(j)})}} \Psi_j^{(k)}. \quad (3.4)$$

We can extend these formulas for a point  $X^{(\text{new})}$  outside the dataset using the Nyström extension [5] as follows:

$$\Psi_j^{(\text{new})} = \frac{1}{\lambda_j} \sum_{i=1}^m \widetilde{M}_s(X^{(\text{new})}, X^{(i)}) \Psi_j^{(i)}, \quad (3.5)$$

where

$$\widetilde{M}_s(X^{(\text{new})}, X^{(i)}) = \frac{K(X^{(\text{new})}, X^{(i)})}{\sqrt{\sum_{j=1}^m K(X^{(\text{new})}, X^{(j)}) \sum_{j=1}^m K(X^{(i)}, X^{(j)})}} \quad (3.6)$$

$$= \frac{1}{m} \frac{K(X^{(\text{new})}, X^{(i)})}{\sqrt{\langle K(X^{(\text{new})}, X^{(j)}) \rangle \langle K(X^{(i)}, X^{(j)}) \rangle}}, \quad (3.7)$$

and  $\langle \cdot \rangle$  denotes expectation. New datapoints in the  $\Phi$  coordinates are related by the equation

$$\Phi_j^{(\text{new})} = \frac{1}{\sqrt{\sum_{j=1}^m K(X^{(\text{new})}, X^{(j)})}} \Psi_j^{(\text{new})}. \quad (3.8)$$

An eigendecomposition is typically performed from a sample database and the Nyström extension is used to efficiently compute the diffusion map coordinates for points outside of the database. It is worth noting that the Nyström extension can be quite successful in *interpolating* new points, but can quickly and spectacularly fail when extrapolating beyond the original database. A discussion of this can be found in [58].

### 3.4 Distance measure for the Schooling Model

In order to form a Markov matrix whose leading eigenvectors provide a reduced set of coarse observables for our dataset, we must first define a distance measure between schools. We choose the one described below which leads to useful diffusion map coordinates.

Let  $N$  be the size of a school and  $d_{i,j}$  denote the Euclidean distance between fish  $i$  and  $j$ . In the following, we will assume that members of a given school

have been sorted by position in increasing order from left to right. Two schools are considered “close” in distance if they are composed of members exhibiting the same behavioral responses at the same ordering index within the school (modulo the left-right reflection symmetry). To account for the the fact that the behavioral zones elicit the same response for a range of distances, we first replace distances  $d_{i,i+1}$ ,  $i = 1, \dots, N - 1$  between subsequent individuals as follows:

$$d_{i,i+1} \rightarrow \begin{cases} r_r, & d_{i,i+1} \leq r_r \\ r_o, & r_r < d_{i,i+1} \leq r_o \\ r_a, & r_o < d_{i,i+1} \leq r_a \\ r_a + \delta, & d_{i,i+1} > r_a \end{cases}$$

That is, immediate neighbors within the repulsion (resp., orientation, attraction) zone are moved a fixed distance  $r_r$  (resp.,  $r_o$ ,  $r_a$ ) apart. Agents that are spaced a distance  $d_{i,i+1} > r_a$  apart, who do not feel any social forces, are moved a fixed distance  $r_a + \delta$  from one another. The precise value of  $\delta$  is not important; in the following we take  $\delta = r_r$ . After replacing distances, the schools are shifted so that the center of mass is at the origin.

After this rearrangement, let  $x_i$  and  $y_i$ ,  $i = 1, \dots, N$ , be the positions of individuals in schools  $X$  and  $Y$ , respectively. The distance  $d(X, Y)$  between schools  $X$  and  $Y$  is defined as

$$d(X, Y) = \min(d_1, d_2),$$

where

$$d_1 = \sqrt{\sum_{i=1}^N (x_i - y_i)^2}, \quad d_2 = \sqrt{\sum_{i=1}^N (x_i - (-y_{N+1-i}))^2}.$$

Here  $d_1$  and  $d_2$  are the Euclidean distances between vectors in  $\mathbb{R}^N$  whose components are the (one-dimensional) coordinates of the sorted positions of the individuals within the school. Note that we take  $\min(d_1, d_2)$  to take into account the reflection symmetry.

## 3.5 Diffusion Map Coordinates for the Schooling Model

Starting with this measure of distance, we can form a Markov matrix from long-simulation data of the model and compute diffusion map coordinates. First we show some results from a dataset created by sampling every 8 time units a  $10^4$  step run (after initial transients have passed) of the original fish schooling model with  $N = 100$ ,  $r_r = 1$ ,  $\Delta r_0 = 0.6$ ,  $\Delta r_a = 1$ , and  $\sigma = 40$  for the diffusion kernel. Note that the Gaussian kernel acts as a nonlinear transformation on distances between points in the dataset. The variance of the kernel,  $\sigma$ , should be chosen so that points close by (in the same well) are at a distance close to one, while points that are far away (in different wells) are at a distance close to zero and thus effectively disconnected from the graph of the dataset. For the distance measure chosen in Section 3.4, “far away” is on the order of 90 units, while “close by” is on the order of 5 units. This narrows the range of possible values for  $\sigma$ . In practice, different values

of  $\sigma$  were tested, and the spectral gap was used as an indicator of an appropriate choice. See Appendix C for an example which compares the effects of varying  $\sigma$  and relates the diffusion map procedure to principal component analysis. Figure 3.1 shows a space-time plot of the school as well as its low-dimensional representation in terms of the second principal eigenvector  $\Phi_2^{(i)}$ . In Figure 3.2 we show that the data collapse on an approximately one-dimensional manifold (projected here on the  $(\Phi_2^{(i)}, \Phi_3^{(i)})$  plane). Simulation points in the  $(\Phi_2^{(i)}, \Phi_3^{(i)})$  coordinates are colored according to their associated value of the empirical coordinate used in Chapter 2:

$$A(t) = \frac{1}{N} \sum_{i=1}^N \min_{j \neq i} |c_j(t) - c_i(t)|, \quad (3.9)$$

the average distance to nearest neighbor. When  $A$  is large (red), the school is in the “mobile” state, and when  $A$  is small (blue), the school is in the “stationary” state. Since the manifold is approximately one-dimensional and there is a large gap in the eigenvalue spectrum, we appear justified in keeping the first nontrivial eigenvector as our coarse observable. The first panel of Figure 3.3 shows the dataset in the two coordinates  $\Phi_2^{(i)}$  and  $A$ .

The second panel of Figure 3.3 shows why the observable  $A$  is less useful than the diffusion map coordinates. This dataset was obtained by running a  $10^4$  step simulation of the schooling model with the same parameters as above but with a slightly different initial population density. Like the previous dataset, the school is transitioning between the stationary and mobile state, however  $A$  takes values in the range  $[0.98, 1.13]$  instead of  $[0.92, 1.07]$ . This is a consequence of the model, which specifies rules of motion based on distances within a zone, allowing the school

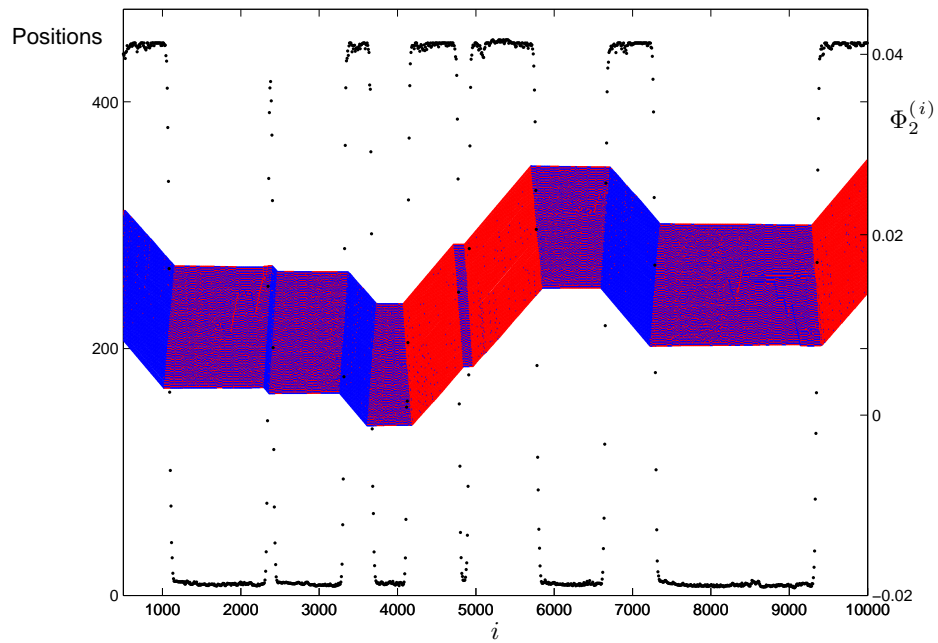


Figure 3.1: Positions of  $N = 100$  agents (after transient) for a  $10^4$  step run of the original schooling model with parameters  $s = 0.75$ ,  $\tau = 0.1$ ,  $r_r = 1$ ,  $\Delta r_o = 0.6$ ,  $\Delta r_a = 1.0$ ,  $p = 0.001$ , red (resp., blue) indicates motion of an agent in the positive (resp., negative) direction. The black dots indicate the corresponding diffusion map coordinate representation.

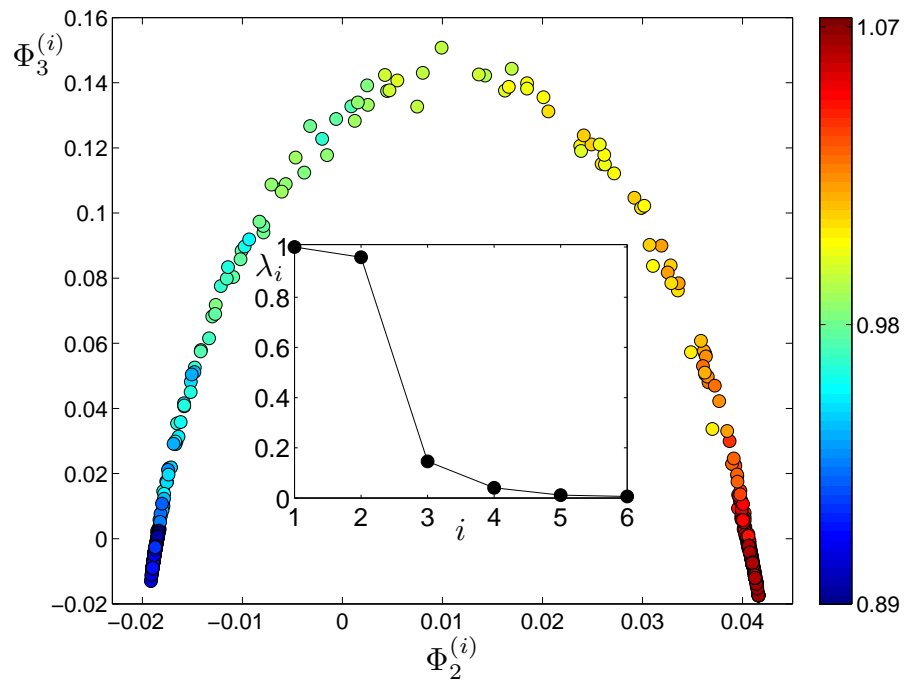


Figure 3.2: Plot of the data in the plane of the first two non-trivial eigenvectors  $(\Phi_2^{(i)}, \Phi_3^{(i)})$  constructed from the simulation dataset. Simulation points in the diffusion map coordinates are colored according to their associated value of the coordinate  $A$ , average distance to nearest neighbor. Inset: Plot of the first few eigenvalues. Since there is a spectral gap, we are justified in keeping  $\Phi_2^{(i)}$  as a single observable for the system.

to exhibit the same dynamics at a range of distances between neighbors. Our new distance measure avoids this problem by replacing the range of distances which yield the same response in the model by a single distance. As can be seen from Figure 3.3, the diffusion map coordinate  $\Phi_2^{(i)}$ , obtained on this new dataset by using the Nyström extension, gives values in the same range as the previous dataset.

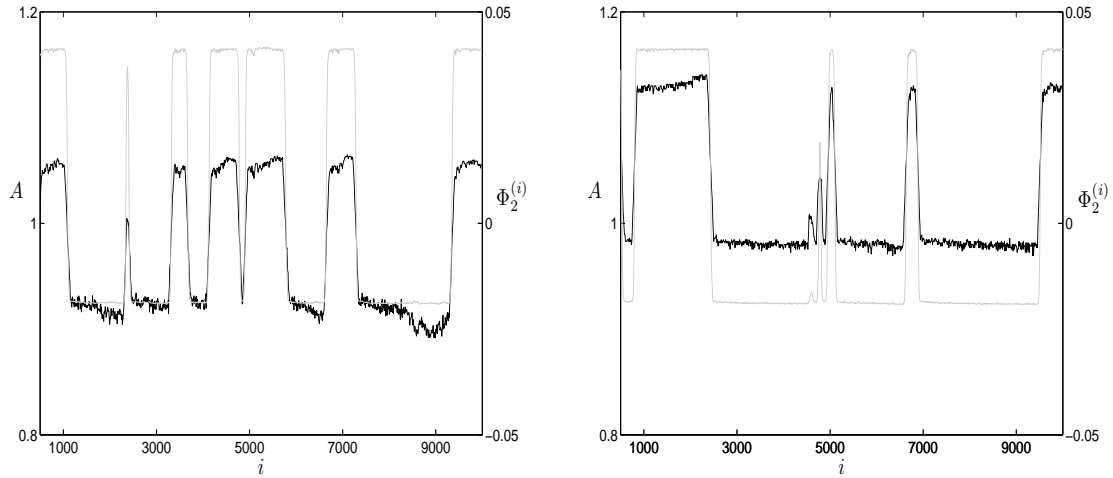


Figure 3.3: Left Panel: Representation of the first dataset in  $A$  (black) and  $\Phi_2^{(i)}$  (gray) coordinates. Right Panel: Representation of the second dataset, a simulation with slightly different initial population density, in  $A$  (black) and  $\Phi_2^{(i)}$  (gray) coordinates. The coordinate  $\Phi_2^{(i)}$  is a more useful coordinate than  $A$ , which may take on a range of values when the school is in the same collective state.

In some cases, a school may fragment into subgroups displaying the same or different dynamics. As in Chapter 2, such fragmented states will not be included in the coarse analysis of the dynamics of the schooling models. Clearly, multiple coordinates are necessary to successfully describe fragmentation and will be the subject of future work.

## 3.6 Estimating the Effective Potential and Mean Residence Times

As discussed in Chapter 2, we may construct an effective potential in terms of the coarse observable  $X = \Phi_2$  from long-time simulation data in one of two ways. The simplest approach is to form a probability distribution function  $P_s(X)$  from long-time simulation statistics and then use the relation  $U(X) = -\log(P_s(X)) + \text{const.}$  This method is used in Figure 3.4, in which the probability distribution functions and corresponding effective potentials for the original and signal constrained schooling model are compared for  $\Delta r_o = 0.2$ . In each case, a database was formed from one hundred  $10^4$  step simulations, with the first 1000 transient steps discarded. As one can see from the figure, for  $\Delta r_o = 0.2$ , the original model has two metastable states, the stationary state at  $\Phi_2 \approx -0.018$  and the mobile state at  $\Phi_2 \approx 0.042$ . The school exhibits stochasticity-induced switching between these states, spending more time in the stationary than in the mobile state on average. For this same parameter value, the signal constrained schooling model has only one stable state at  $\Phi_2 = -0.018$ , remaining in the stationary state for the entire duration of the simulations. For larger values of  $\Delta r_o$ , the signal constrained model does exhibit switching between the stationary and mobile state. It therefore appears that the signalling constraint prevents the mobile state from existing below a certain threshold of the parameter  $\Delta r_o$ . We will investigate the precise parametric dependencies in the next section.

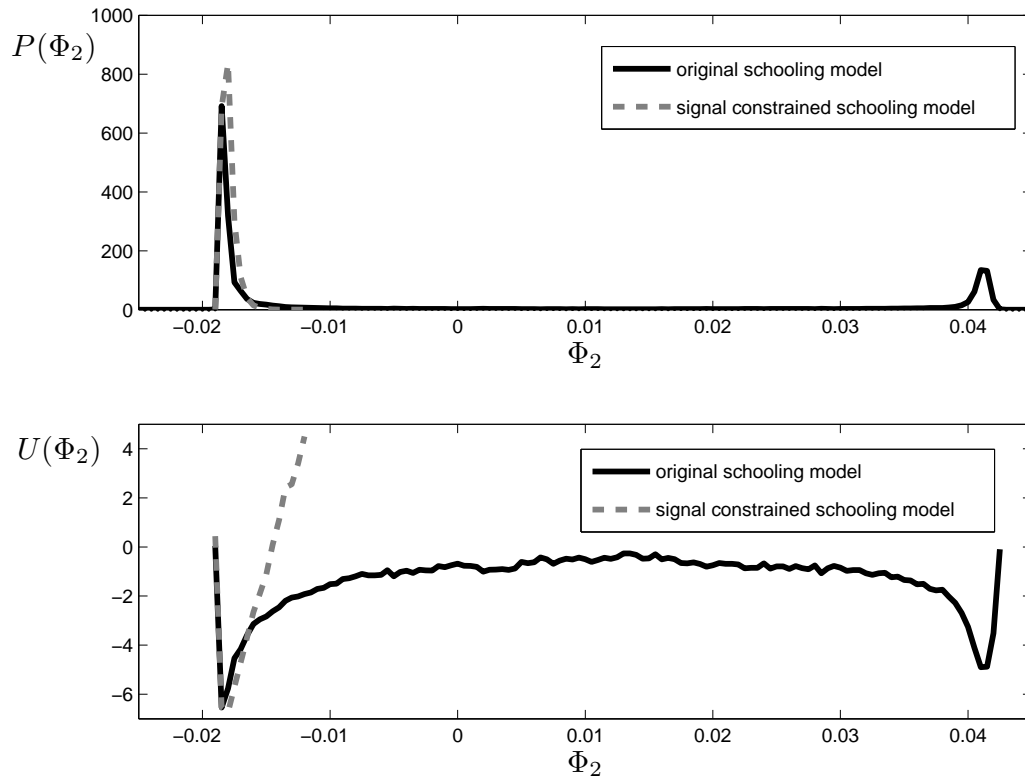


Figure 3.4: Probability distributions and corresponding effective potentials for the original and signal constrained schooling model with  $\Delta r_o = 0.2$ .

Alternatively, one may construct an effective potential by assuming that the observable  $X = \Phi_2$  obeys an effective Langevin equation, or equivalently its probability distribution  $P(X)$  obeys an effective Fokker-Planck equation. As described in Chapter 2, the effective potential  $U(X)$  satisfies

$$U(X) = \log(D^{(2)}(X)) - \int_{-\infty}^X \frac{D^{(1)}(X')}{D^{(2)}(X')} dX' + \text{const.}, \quad (3.10)$$

where the drift and diffusion terms are related to the short time evolution of the first two moments as

$$D^{(1)}(X_0) = \left. \frac{\partial \langle X(t; X_0) \rangle}{\partial t} \right|_{t=0}, \quad D^{(2)}(X_0) = \left. \frac{1}{2} \frac{\partial \text{Var}(t; X_0)}{\partial t} \right|_{t=0}. \quad (3.11)$$

One may estimate the effective potential by compiling enough statistics from long-time simulation data to estimate the drift and diffusion terms using (3.11). Here, we discretize  $X = \Phi_2$  over a grid of values in the range  $[-0.019, 0.043]$  with a uniform mesh of size  $10^{-3}$ . Once the drift and diffusion terms are estimated,  $U(X)$  is estimated by numerically approximating the integral in equation (3.10).

Figure 3.5 shows the drift, diffusion, and effective potential as a function of  $\Phi_2$ , the latter obtained using both estimation approaches for the original schooling model with  $\Delta r_o = 0.6$ . The effective potential formed using equation (3.11) agrees very well with that obtained using the relation  $U(X) = -\log(P_s(X)) + \text{const}$ , which supports our choice of  $X = \Phi_2$ .

With  $U(X)$  and  $D^{(2)}(X)$  computed using the second approach, we may estimate the mean residence times in each well using Kramers formula (2.16) as in Chapter 2. For  $\Delta r_o = 0.6$ , the mean residence times were estimated to be  $T = 850$  for

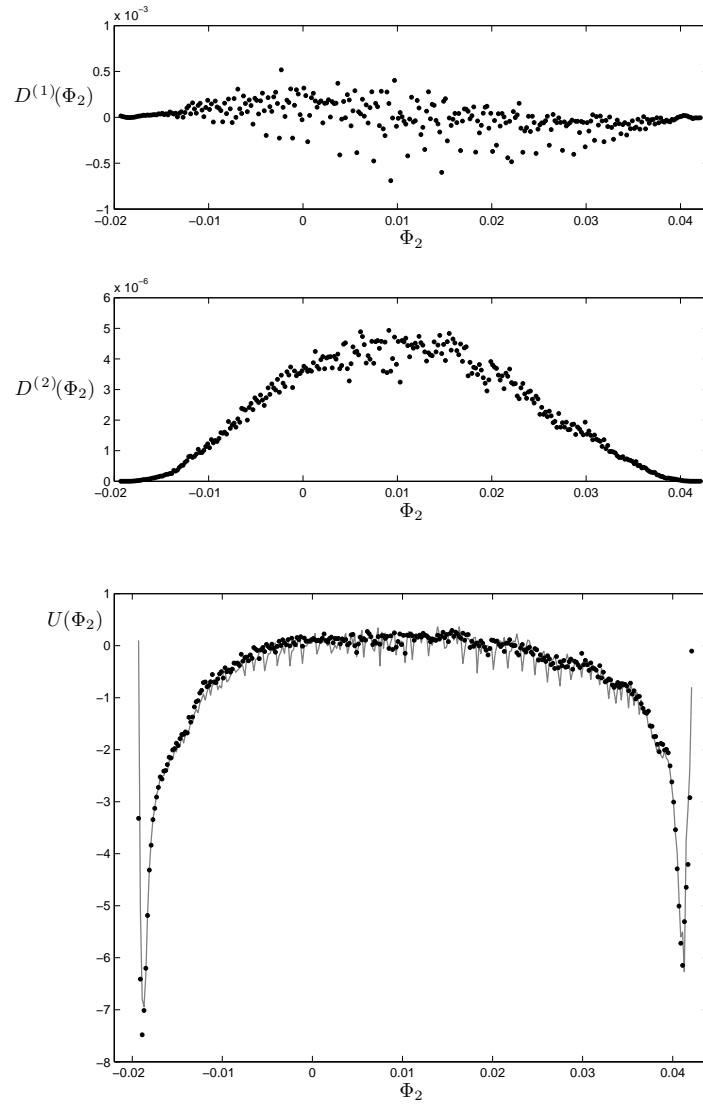


Figure 3.5: Top: Drift  $D^{(1)}(\Phi_2)$  and diffusion terms  $D^{(2)}(\Phi_2)$  estimated from the simulation dataset. Bottom: Estimates of the effective potential, using  $U(\Phi_2) = -\log(P_s(\Phi_2)) + \text{const.}$  (solid gray) and estimating the drift and diffusion terms and using equation (2.10) (black dots).

the leftmost well and  $T = 321$  for the well on the right. The second derivatives in equation (2.16) were estimated using a centered difference approximation. These estimated times compare well to the mean residence times observed directly from the simulation ensemble database in Chapter 2, which gave times of approximately  $T_1 = 1026$  and  $T_2 = 507$  for  $\Delta r_o = 0.6$ . This lends further support that  $X = \Phi_2$  is an appropriate dynamic observable for the schooling model.

### 3.7 Coarse Bifurcation Diagrams

We investigate the dependencies of the schooling model on the parameter  $\Delta r_o$ , the width of the zone of orientation, by tracking the critical points of the corresponding effective potentials. As discussed in Chapter 2, we associate minima of the effective potential with stable fixed points and 1-D maxima (more generally, saddle points) with unstable fixed points. With this association, we may form a coarse bifurcation diagram by locating the critical points of the effective potential as the parameter  $\Delta r_o$  is varied.

As we discussed in Section 3.5, school fragmentation occurs with some probability in many of our simulations. Thus, some of the effective potentials (and associated probability distribution functions) have multiple valleys (peaks) for values of  $\Delta r_o$  within the bistable range. These metastable states are associated with the fragmentation of the group into noncoordinated subgroups and are typically quite small in comparison to the coordinated wells. As in Chapter 2, to filter out such spurious states, we perform a quadratic fit of the effective potential between

the stationary and mobile wells. This allows us to estimate the saddle point of the effective potential, and thus obtain a good approximation of the unstable branch of the bifurcation diagram. See Figure 3.6 for plots of the bifurcation diagrams for the original and signal constrained schooling model.

For the original schooling model, two saddle node bifurcations are found at  $\Delta r_o \approx 0.12$  and  $\Delta r_o \approx 1.1$  and the system is bistable for  $\Delta r_o$  within this range. The diagram compares well qualitatively with the one constructed in Chapter 2 with the empirical observable  $A$ . For the signal constrained model, we also find two saddle node bifurcations, but they are located at  $\Delta r_o \approx 0.85$  and  $\Delta r_o \approx 1.2$ . Thus, it seems that the signalling constraint effectively prevents the mobile state from existing below  $\Delta r_o = 0.85$ , and the parameter range for which the original model is bistable is effectively shortened.

We can understand the effect of the signalling constraint as follows. The parametric range of existence (and stability) of the stationary state is virtually the same for both models. This is not surprising since this state is driven by repulsion events, which are unaffected by the signalling constraint. On the other hand, a larger  $\Delta r_o$  is necessary to get enough interactions when the signalling constraint is present to “hold together” the mobile state.

## 3.8 Conclusion

We studied the effects of a signalling constraint on an individual-based model of self-organizing group formation using a coarse analysis framework. This involved

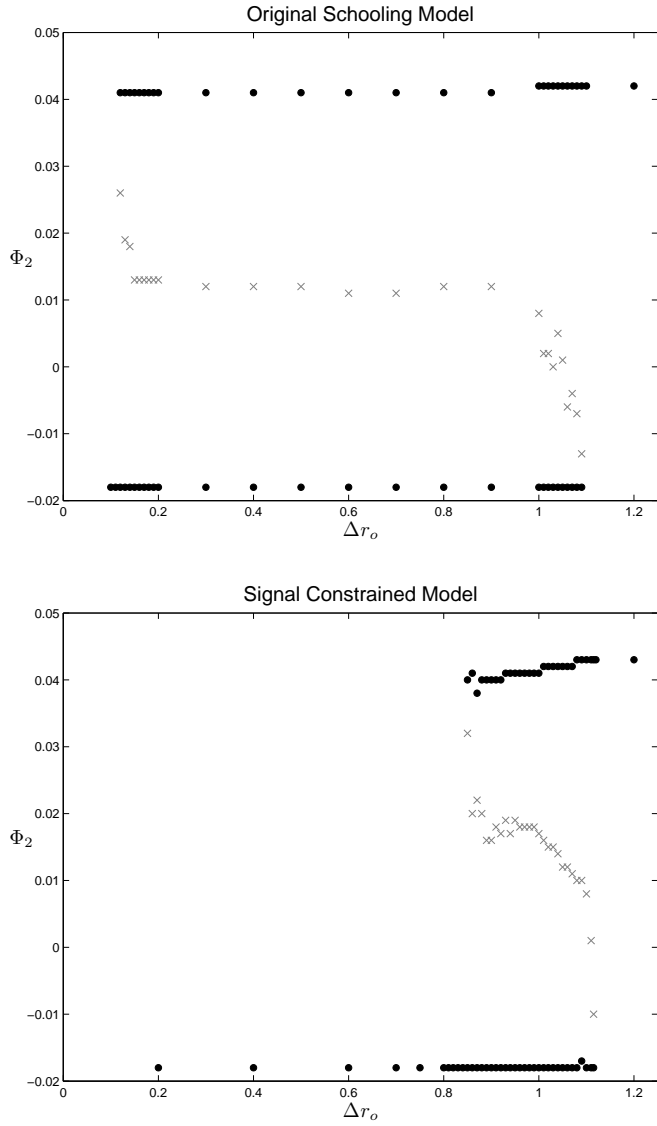


Figure 3.6: Coarse bifurcation diagrams showing the critical points of the effective potential as  $\Delta r_o$  is varied. The minima of the effective potential correspond to the stable branch (black dots) and the maxima correspond to the unstable branch (gray x's). Left panel: original schooling model, Right panel: signal constrained schooling model.

the selection of a coarse variable by defining a diffusion process on the graph of a sample dataset formed from a representative steady-state simulation. The eigenvectors of the graph Laplacian were used to construct “diffusion-map” coordinates which provide a geometrically meaningful low-dimensional representation of the dataset. The first nontrivial (second principal) eigenvector provided a sufficient representation of the dataset, so we used it as a coarse observable. This facilitated the computation of coarse bifurcation diagrams, which showed that the signalling constraint reduces the region over which there is bistability between the stationary and mobile collective motion states. Overall, our results suggest that the diffusion map framework is a promising new approach for understanding collective motion for fish schooling models.

Our approach complements the one used in Chapter 2. The main difference is that in Chapter 2 we used the average distance to nearest neighbor as a coarse variable to characterize the collective behavior of the school. This was shown to be a dynamically meaningful observable through computational experiments to test possible candidate observables. In this paper, we instead used an automated data-driven technique for generating the coarse variable. Although it is difficult to interpret this coarse variable physically, we were able to use it to construct effective potentials and calculate bifurcation behavior. In addition, our approach overcomes the “neutral stability” issue that arose for the coarse observable used in Chapter 2. We also note that in Chapter 2 we developed a “lifting” procedure which initializes the individual-based model with a particular value of the coarse variable

and allowed more efficient population-level analysis. The necessity for lifting (and the associated difficulties) did not arise in the computations presented here.

The framework developed in Chapters 2 and 3 provides a useful, computer-assisted approach for the analysis of emergent phenomena in individual-based models for collective motion. Most analysis of individual-based models in the field of group formation has relied on costly long-time simulations, which has limited the number of individuals that can be simulated as well as the types of analysis that can be realistically done [84]. This approach allows one to achieve a new level of understanding and quantification of biological self-organization by bridging individual-based modeling with coarse, population-level analysis. A challenge for extending this framework to two- or three-dimensional schools is the development of an appropriate measure for the distance between two schools, which perhaps would have to take into account the positions *and velocities* of all individuals. This would allow the computation of diffusion map coordinates which could aid in a similar analysis of stochasticity-induced switching between the milling and parallel motion states as was reported in Figure 2.2 of Chapter 2.

# Chapter 4

## Bistability in a Model for Collective Motion with Coupled Oscillator Dynamics

### 4.1 Introduction

In Chapters 2 and 3 we showed for a discrete-time individual-based schooling model, transitions between qualitatively different collective motion states can occur entirely due to stochastic effects. In particular, changing behavioral rules or environmental factors, including the introduction of predators, are *not* necessary for such transitions to occur. Such stochasticity-induced transitions require the presence of at least two metastable collective states and noise of appropriate type and strength.

In this Chapter, we will consider how to design interaction rules that simultaneously stabilize different collective motion states for a continuous-time kinetic model of collective motion with coupled oscillator dynamics. Such models have recently been developed in the engineering literature for applications such as formation control of unmanned vehicles and spacecraft [49, 95, 96], cooperative robotics [12], and sensor networks [15]. Much of this work has been devoted to developing interaction rules which allow a population to robustly operate in a particular collective motion state, perhaps with or without centralized coordination, see, e.g. [22, 31, 47, 49, 60, 78, 82, 96].

Here, we will instead consider how to design interaction rules which simultaneously stabilize different collective motion states. For simplicity, we consider the motion of two agents, and restrict our study to the phase dynamics, treating the agents as a system of coupled oscillators. We reduce the dynamics to a single coarse observable, the phase difference, and find a class of interaction rules that simultaneously stabilize parallel (zero phase-difference) and anti-parallel ( $\pi$  phase difference) motion. With the addition of Gaussian white noise of appropriate strength, the system exhibits stochasticity-induced switching between such states. The effects of the noise on the dynamics of the system will be explored numerically by estimating an effective potential and mean residence times using a coarse-grained, computer assisted framework. Such estimates compare favorably with those obtained from long-time steady state computations as well as analytically derived results.

## 4.2 The Model

We consider a model which was recently presented in [49, 95, 96] in which each agent is modeled as a point particle travelling at unit speed and interacts with other agents through steering control  $u_k$ :

$$\dot{r}_k = e^{i\theta_k}, \quad \dot{\theta}_k = u_k(\mathbf{r}, \theta), \quad k = 1, 2, \dots, N. \quad (4.1)$$

Here  $r_k = x_k + iy_k$  gives the position of agent  $k$  in the  $(x, y)$  plane and the angle  $\theta_k$  gives its orientation relative to the  $x$  axis. The function  $u_k$  is the steering control for agent  $k$ . When  $u_k = 0$ ,  $\theta_k$  remains constant, so that agent  $k$  moves in a straight line.

In [95], different control laws were presented to stabilize and switch between different collective motion patterns, including rectilinear motion of all agents in the same or different directions, and circular formations with agents at the same location or spread evenly around the circle. Steering control was split into spacing and orientation terms  $u_k = u_k^{spac}(\mathbf{r}, \theta) + u_k^{ori}(\theta)$ , with the latter benefitting from the well-developed theory of coupled oscillators [4, 9]. In [81] it was demonstrated for  $N = 2$  agents that steering control can be chosen to stabilize both rectilinear and circular collective motions at the same control parameter values. This arises due to the interplay between the spacing and orientation components of the steering control law.

Here, we show that for  $N = 2$  agents a different kind of bistability, in which both parallel and anti-parallel motions are stable, can be achieved for (4.1) solely

through the choice of the coupling function for the control of the phase dynamics.

We consider steering control laws of the form

$$\begin{aligned}\dot{\theta}_1 &= \omega + Kf(\theta_2 - \theta_1) \equiv u_1^0, \\ \dot{\theta}_2 &= \omega + Kf(\theta_1 - \theta_2) \equiv u_2^0.\end{aligned}\tag{4.2}$$

Borrowing the terminology of coupled oscillators, we refer to  $\omega$  as the natural oscillator frequency,  $K$  as the coupling strength, and  $f$  as the coupling function, which is  $2\pi$ -periodic. Setting  $\psi = \theta_1 - \theta_2$ , (4.2) yields

$$\dot{\psi} = K(f(-\psi) - f(\psi)) \equiv Kg(\psi).\tag{4.3}$$

In the context of coarse-grained computation, we may think of  $\psi$  as a *coarse observable* since it describes the collective behavior of the oscillators. For example, when  $\psi = 0$ , the oscillators are *in phase*, while when  $\psi = \pi$ , the oscillators are  $\pi$  out of phase, which is referred to as the *splay state*.

### 4.2.1 Fixed Points and Stability

We now make some general comments regarding the stability properties of (4.3). Note that  $g(\psi)$  is an odd function since  $g(-\psi) = f(\psi) - f(-\psi) = -g(\psi)$ . Phase-locked solutions, for which  $\theta_1 - \theta_2$  remains constant for all time, correspond to fixed points  $\psi_p$  of (4.3). The asymptotic stability of a phase-locked solution is determined as follows: if  $Kg'(\psi_p) < 0$  then it is stable, and if  $Kg'(\psi_p) > 0$  then it is unstable. Unless otherwise stated, in the following we take  $K > 0$ .

For any coupling function  $f$  one finds that

$$g(0) = f(0) - f(0) = 0, \quad (4.4)$$

and

$$g(\pi) = f(-\pi) - f(\pi) = f(\pi) - f(\pi) = 0. \quad (4.5)$$

Thus  $\psi = 0$  and  $\psi = \pi$  are always fixed points of (4.3). The solution  $\psi = 0$  corresponds to the two agents always having the same instantaneous orientations, and following the notation of [4, 9] will be referred to as the  $S_2$  state because such solutions are invariant under the permutation symmetry  $(\theta_1, \theta_2) \rightarrow (\theta_2, \theta_1)$ .<sup>1</sup> The solution  $\psi = \pi$  corresponds to the agents always having orientations which differ by  $\pi$  radians, and will be called the  $Z_2$  state because such solutions are invariant under the symmetry  $(\theta_1, \theta_2) \rightarrow (\theta_2 + \pi, \theta_1 + \pi)$ .<sup>2</sup> Other fixed points of (4.3), corresponding to phase-locked solutions with the instantaneous orientation of the agents being an angle not equal to 0 or  $\pi$ , are also possible, but are not guaranteed to exist for all coupling functions [4, 9]. Such solutions are called  $S_1 \times S_1$  states, and are not invariant under any nontrivial symmetries.

As discussed in [96], the relationship between the phase-locked states and the motion of agents which obey (4.1) is as follows:

- i) For  $\dot{\theta}_1 = \dot{\theta}_2 = 0$ , the  $S_2$  state corresponds to the agents moving in straight lines parallel to each other.

---

<sup>1</sup> $S_n$  is the  $n!$  element permutation group on  $n$  elements.

<sup>2</sup> $Z_n$  is the cyclic group with  $n$  elements.

ii) For  $\dot{\theta}_1 = \dot{\theta}_2 \neq 0$ , the  $S_2$  state corresponds to the agents moving in circles with velocities always pointing in the same direction.

iii) For  $\dot{\theta}_1 = \dot{\theta}_2 = 0$ , the  $Z_2$  state corresponds to the agents moving in straight lines anti-parallel to each other.

iv) For  $\dot{\theta}_1 = \dot{\theta}_2 \neq 0$ , the  $Z_2$  state corresponds to the agents moving in circles with velocities always pointing in opposite directions.

The  $S_1 \times S_1$  solutions have similar interpretations:

v) For  $\dot{\theta}_1 = \dot{\theta}_2 = 0$ , the  $S_1 \times S_1$  state corresponds to the agents moving in straight lines neither parallel nor anti-parallel to each other.

vi) For  $\dot{\theta}_1 = \dot{\theta}_2 \neq 0$ , the  $S_1 \times S_1$  state corresponds to the agents moving in circles with velocities not pointing in either the same nor in opposite directions.

See Figure 4.1 for illustrations of each of these cases.

## 4.2.2 Coupling Function and Bistability

For bistability of the phase-locked states  $S_2$  ( $\psi = 0$ ) and  $Z_2$  ( $\psi = \pi$ ), both  $g'(0) < 0$  and  $g'(\pi) < 0$ . Since  $g$  is a  $2\pi$ -periodic odd function, we may write it as

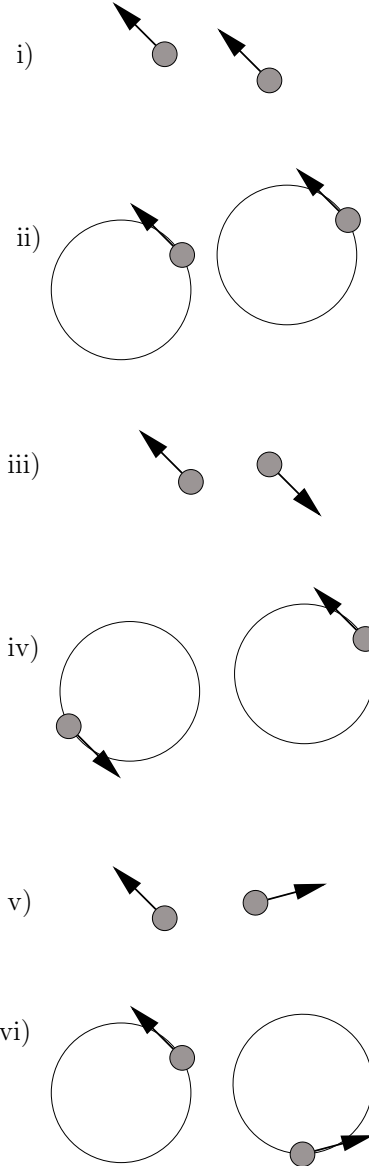


Figure 4.1: Phase-locked motion of  $N = 2$  agents obeying equations (4.1). (i)  $S_2$  state with  $\dot{\theta}_1 = \dot{\theta}_2 = 0$ , (ii)  $S_2$  state with  $\dot{\theta}_1 = \dot{\theta}_2 \neq 0$ , (iii)  $Z_2$  state with  $\dot{\theta}_1 = \dot{\theta}_2 = 0$ , (iv)  $Z_2$  state with  $\dot{\theta}_1 = \dot{\theta}_2 \neq 0$ , (v)  $S_1 \times S_1$  state with  $\dot{\theta}_1 = \dot{\theta}_2 = 0$ , (vi)  $S_1 \times S_1$  state with  $\dot{\theta}_1 = \dot{\theta}_2 \neq 0$ .

a Fourier series:

$$g(\psi) = \sum_{n=1}^{\infty} a_n \sin(n\psi). \quad (4.6)$$

Thus, the following conditions must be satisfied for bistability:

$$g'(0) = \sum_{n=1}^{\infty} n a_n < 0, \quad g'(\pi) = \sum_{n=1}^{\infty} (-1)^n n a_n < 0. \quad (4.7)$$

From these conditions, one may readily see that for bistability of the  $S_2$  and  $Z_2$  states,  $g$  must include even harmonics. (If  $g$  only includes odd harmonics, then  $g'(\pi) = -g'(0)$ , and so conditions (4.7) cannot be simultaneously satisfied.)

As an example, suppose we take the coupling function

$$f(\theta) = A \sin \theta + B \sin 2\theta, \quad (4.8)$$

so that

$$g(\psi) = -2A \sin \psi - 2B \sin 2\psi. \quad (4.9)$$

Fixed points of (4.3) are the zeros of (4.9), namely  $\psi = 0$ ,  $\psi = \pi$ , and

$$\psi_{S_1 \times S_1}^{\pm} \equiv \pm \cos^{-1} \left( -\frac{A}{2B} \right), \quad (4.10)$$

with the latter only existing when  $|A/(2B)| \leq 1$ . Using

$$g'(0) = -2A - 4B, \quad (4.11)$$

$$g'(\pi) = 2A - 4B, \quad (4.12)$$

$$g'(\psi_{S_1 \times S_1}^{\pm}) = 4B - A^2/B, \quad (4.13)$$

we obtain the existence and stability results summarized in Figure 4.2. In particular, there are regions of parameter space  $(A, B)$  for which only the  $S_2$ ,  $Z_2$ , or  $S_1 \times S_1$

state is stable. Furthermore, by choosing  $B > -A/2$  and  $B > A/2$ , both the  $S_2$  and  $Z_2$  states are stable.

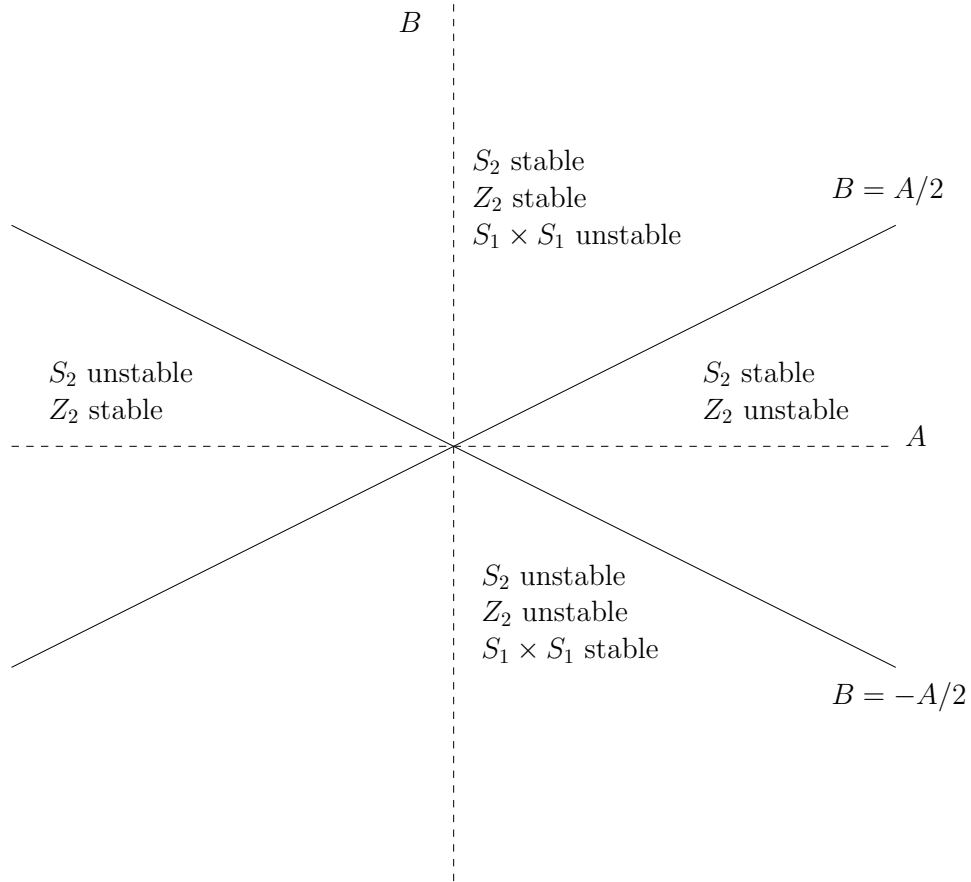


Figure 4.2: Existence and stability of the  $S_2$ ,  $Z_2$  and  $S_1 \times S_1$  states in the  $(A, B)$  plane for the phase control law with coupling function given by (4.8). If  $B > -A/2$  and  $B > A/2$  then both the  $S_2$  and  $Z_2$  states are stable.

Before proceeding, it is instructive to consider how  $g$  changes for this example as  $A$  is held constant and  $B$  is increased. From Figure 4.3 we see that the curve  $B = A/2$  corresponds to a pitchfork bifurcation [38] of the  $Z_2$  state, in which two symmetry-related  $S_1 \times S_1$  states are born. (We note that the  $S_1 \times S_1$  states form the boundaries of the basins of attraction of the  $S_2$  and  $Z_2$  states: see Figure 4.3(iii).) Similarly, the curve  $B = -A/2$  corresponds to a pitchfork bifurcation of the  $S_2$

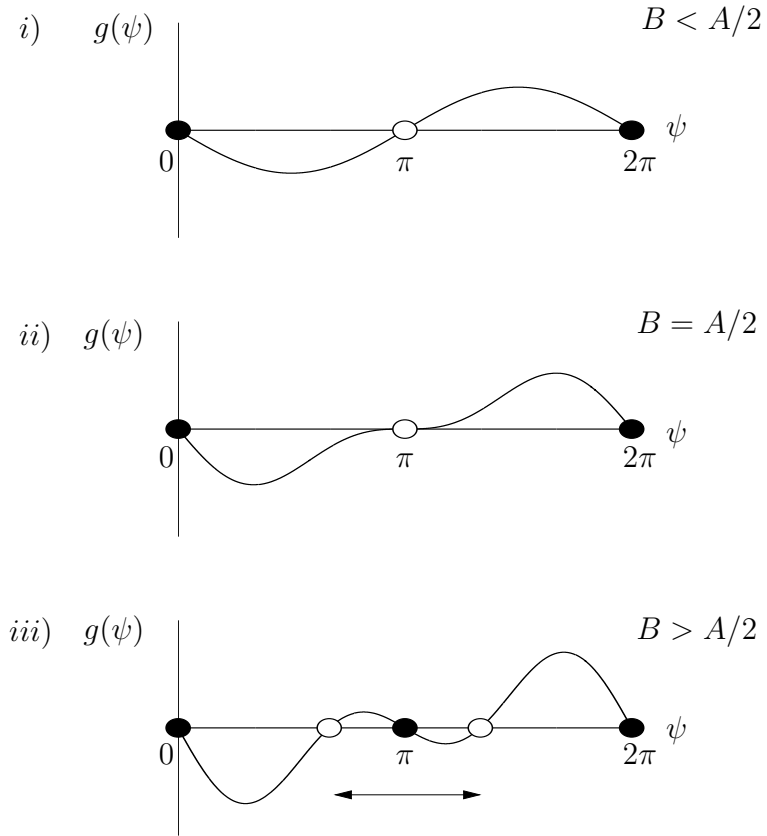


Figure 4.3: Pitchfork bifurcation of the  $Z_2$  state as  $A$  is held constant and  $B$  is increased for the phase control law with coupling function given by (4.8). In this example,  $A = 2$  and (i)  $B = 0$  (ii)  $B = 1$ , and (iii)  $B = 2$ . The  $S_2$  state corresponds to  $\psi = 0$ , the  $Z_2$  state corresponds to  $\psi = \pi$ , and the  $S_1 \times S_1$  state corresponds to  $\psi = \cos^{-1}(-1/2)$ . For (iii), the basin of attraction for the  $Z_2$  symmetric state is indicated by the arrows; the complement to this, excluding the  $S_1 \times S_1$  states, is the basin of attraction for the  $S_2$  state.

state.

Finally, we note that results for  $B = 0$  (i.e.,  $f(\theta) = A \sin(\theta)$ ) have been considered in detail in the work of Sepulchre, Paley, and Leonard (e.g. [81, 95]), not just for two agents, but for an arbitrary number. For the case of two agents,  $g(\psi) = -2A \sin(\psi)$  with  $g'(0) = -2A$  and  $g'(\pi) = 2A = -g'(0)$ . Thus, it is not possible to choose  $A$  so that both  $g'(0) < 0$  and  $g'(\pi) < 0$ . In this case, only the  $S_2$  or the  $Z_2$  state is stable, and one can switch their stability by letting the coupling constant  $K \rightarrow -K$ .

### 4.3 Stochasticity-Induced Switching

In the case that the  $S_2$  and  $Z_2$  state coexist, noise can induce switching between the two states. Here we consider the dynamics of such stochasticity-induced switching by adding Gaussian white noise to equations (4.2):

$$\begin{aligned}\dot{\theta}_1 &= \omega + Kf(\theta_2 - \theta_1) + \lambda_1 \xi_1(t), \\ \dot{\theta}_2 &= \omega + Kf(\theta_1 - \theta_2) + \lambda_2 \xi_2(t).\end{aligned}\tag{4.14}$$

We choose  $f(\theta) = A \sin(\theta) + B \sin(2\theta)$  which was shown in Section 4.2.2 to be bistable for  $A$  and  $B$  satisfying  $B > -A/2$  and  $B > A/2$ . Here  $\xi_1(t)$  and  $\xi_2(t)$  are uncorrelated Gaussian white noise signals with  $\langle \xi_i(t) \rangle = 0$  and  $\langle \xi_i(t) \xi_j(t') \rangle = \delta_{ij} \delta(t - t')$ , and  $\lambda_1$  and  $\lambda_2$  are noise strengths.

### 4.3.1 Coarse Analysis

Choosing the coarse observable  $\psi = \theta_1 - \theta_2$ , it follows that

$$\dot{\psi} = Kg(\psi) + \lambda\xi(t), \quad (4.15)$$

with  $g(\psi) = f(-\psi) - f(\psi) = -2A \sin(\psi) - 2B \sin(2\psi)$ , unit variance white noise  $\xi(t)$ , with noise strength  $\lambda = \sqrt{\lambda_1^2 + \lambda_2^2}$ . One may rewrite equation (4.15) as

$$d\psi = g(\psi)dt + \lambda dW, \quad (4.16)$$

where  $W(t)$  is a Wiener process. This is a one-dimensional Langevin equation with potential  $U_0(\psi)$  defined so that  $U_0'(\psi) = -g(\psi)$ . The statistical behavior of equation (4.16) is determined by the Fokker-Planck equation [30]:

$$\frac{\partial P(\psi, t)}{\partial t} = -\frac{\partial}{\partial \psi} [g(\psi)P(\psi, t)] + \frac{\lambda^2}{2} \frac{\partial^2}{\partial \psi^2} [P(\psi, t)], \quad (4.17)$$

where  $P(\psi, t)$  is the probability density function with  $P(\psi, t_0 | \psi_0, t_0) = \delta(\psi - \psi_0)$ .

We impose periodic boundary conditions over the  $2\pi$ -periodic interval  $(a, b)$  for solutions to equations (4.16) and (4.17). The stationary solution  $P_s(\psi)$  is found by solving (4.17) with  $\partial/\partial t = 0$ :

$$g(\psi)P_s(\psi) - \frac{\lambda^2}{2} \frac{\partial}{\partial \psi} [P_s(\psi)] = J, \quad (4.18)$$

where  $J$  is the constant probability current. This can be easily integrated over  $(a, b)$

to give

$$P_s(\psi) = P_s(a)G(\psi) - \frac{2J}{\lambda^2} G(\psi) \int_a^\psi \frac{d\psi'}{G(\psi')}, \quad (4.19)$$

where

$$G(\psi) = \exp\left(\frac{2}{\lambda^2} \int_a^\psi g(\psi') d\psi'\right). \quad (4.20)$$

Imposing periodic boundary conditions over the interval  $(a, b)$ ,  $P_s(a) = P_s(b)$ , and since  $g$  is  $2\pi$ -periodic over  $(a, b)$ ,  $G(a) = G(b)$ . It follows that  $J = 0$  so that

$$P_s(\psi) = N e^{\frac{-2U_0(\psi)}{\lambda^2}}, \quad (4.21)$$

where  $U_0(\psi) = -\int_a^\psi g(\psi') d\psi'$  and  $N$  is a normalization constant such that  $\int_a^b P_s(\psi) d\psi = 1$ .

In the case that the  $S_2$  and  $Z_2$  states coexist, then the corresponding  $U_0(\psi)$  is a double well potential with minima at  $\psi = 0$  and  $\psi = \pi$  corresponding to the  $S_2$  and  $Z_2$  collective states, respectively. With the Fokker-Planck or Langevin formalism, one may view the dynamics of the variable  $\psi$  as governed by the effective potential  $U(\psi) = 2U_0(\psi)/\lambda^2$ , with the noise term inducing transitions between the two metastable collective states, located at the minima of the wells.

### 4.3.2 Numerical Simulations

We simulate equations (4.14) with  $A = 1, B = 5$ , and  $\lambda^2 = 2$ , using the Euler-Maruyama method for stochastic differential equations [42]. See Figure 4.4 for a sample trajectory initialized at  $(\theta_1, \theta_2) = (\pi, 0)$  plotted as a function of the coarse observable  $\psi(t) = \theta_1(t) - \theta_2(t)$ . Here we use periodic boundary conditions over the  $2\pi$ -periodic interval  $(a, b) = (-\cos^{-1}(-1/10), -\cos^{-1}(-1/10) + 2\pi)$  enclosing the stable fixed points  $\psi = 0, \pi$  and unstable fixed point  $\psi = \cos^{-1}(-1/10)$ . As you can see from the figure, the system exhibits noise-induced transitions between the two metastable states  $S_2$  ( $\psi = 0$ ) and  $Z_2$  ( $\psi = \pi$ ). See Figure 4.6 for a plot of the effective potential  $U(\psi) = U_0(\psi) = -2\cos(\psi) - 5\cos(2\psi)$  over this interval. The

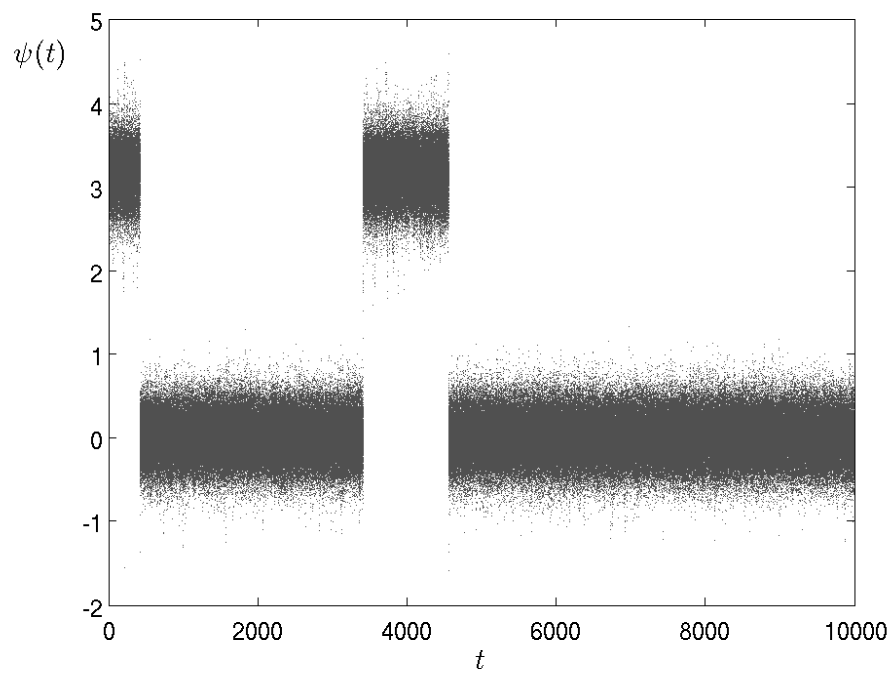


Figure 4.4: Sample trajectory in  $\psi$  coordinates for equations (4.2) simulated with Euler-Marayama method with a stepsize of  $\Delta t = 0.02$  and initial condition  $(\theta_1, \theta_2) = (\pi, 0)$ .

stable fixed points,  $\psi = 0$  and  $\psi = \pi$ , are located at the minima of  $U(\psi)$  and the unstable fixed point,  $\psi = \arccos(-1/10)$ , is the local maxima of  $U(\psi)$ .

### 4.3.3 Coarse-Grained Computation

We now demonstrate how coarse-grained computation can be used to quantify the collective dynamics of the two agent system in terms of the coarse variable  $\psi = \theta_1 - \theta_2$ , using only simulations of the individual-based oscillator equations (4.14). Since equations at both the fine and coarse level are explicitly known, we compare analytical expressions for  $U(\psi)$ ,  $D^{(1)}(\psi)$  and  $D^{(2)}(\psi)$  with numerical estimates.

For the moment, let's suppose that we do not have population-level equations for  $\psi$ , i.e., equation (4.16) or its equivalent Fokker-Planck form (4.17). We may still, however, estimate the effective potential  $U(\psi)$  if we make the assumption that  $\psi$  satisfies a generalized Fokker-Planck equation of the form

$$\frac{\partial P(\psi, t)}{\partial t} = -\frac{\partial}{\partial \psi} [D^{(1)}(\psi)P(\psi, t)] + \frac{\partial}{\partial \psi^2} [D^{(2)}(\psi)P(\psi, t)], \quad (4.22)$$

where  $D^{(1)}(\psi)$  is the drift coefficient and  $D^{(2)}(\psi) > 0$  is the diffusion coefficient, which are related to the first two moments of  $\psi$  as

$$D^{(1)}(\psi_0) = \left. \frac{\partial \langle \psi(t; \psi_0) \rangle}{\partial t} \right|_{t=0}, \quad D^{(2)}(\psi_0) = \left. \frac{1}{2} \frac{\partial \text{Var}(t; \psi_0)}{\partial t} \right|_{t=0}, \quad (4.23)$$

where  $\psi(t; \psi_0)$  denotes a trajectory at  $t = 0$  initialized at  $\psi_0$ , angular brackets denotes averaging over different realizations of the trajectory, and  $\text{Var}(\psi)$  denotes

the variance of  $\psi$  for such an ensemble. Assuming

$$P_s(\psi) \sim \exp(-U(\psi)) \quad (4.24)$$

at steady state, it follows that the effective potential  $U(\psi)$  satisfies

$$U(\psi) = \log(D^{(2)}(\psi)) - \int_a^\psi \frac{D^{(1)}(\psi')}{D^{(2)}(\psi')} d\psi' + \text{const.} \quad (4.25)$$

We may use expressions (4.24) and (4.25) to estimate  $U(\psi)$  two different ways.

The simplest approach is to compile statistics from long-time simulation data, and then use expression (4.24) to estimate  $U(\psi)$  from  $P_s(\psi)$ . To do so, one must integrate the individual oscillator equations (4.14) and then *restrict* from fine to coarse to gain a representation in terms of the coarse variable  $\psi$ . Here, restriction is performed simply using the definition of  $\psi$  as  $\psi = \theta_1 - \theta_2$ .

An alternative, more efficient approach, is to estimate the drift  $D^{(1)}(\psi)$  and diffusion  $D^{(2)}(\psi)$  terms and then use equation (4.25) to estimate  $U(\psi)$ . This may be done as follows. First, discretize  $\psi$  over a mesh of values. To *lift* from coarse to fine, i.e., initialize  $\psi$  at a given  $\psi_0$ , set  $(\theta_1, \theta_2) = (\psi_0, 0)$  as an initial condition in equations (4.14). Note that lifting is a one to many mapping and thus the choice of lifting operation is *not* unique. With the prescribed lifting procedure, one may integrate ensembles of trajectories with the same initial condition  $\psi = \psi_0$  over a short time interval (there is no “healing time” since  $\psi$  is the only macroscopic variable) and then estimate the rate of change of the mean (resp., variance) by taking the slope of the linear regression of  $\langle \psi(t; \psi_0) \rangle$  (resp.,  $\text{Var}(t; \psi_0)$ ), using the restriction operation to obtain the coarse representation in terms of  $\psi$ . Once the

drift and diffusion terms are estimated over the mesh of  $\psi$  values, the integral in expression (4.25) may be numerically approximated to estimate the effective potential  $U(\psi)$ .

For the coupling function and noise studied in section 4.3.2, an ensemble of 1000 simulations was performed for each  $\psi_0$  over a grid of mesh 0.05 to estimate the drift and diffusion terms. Analytical expressions for the drift term  $D^{(1)}(\psi) = g(\psi) = -2 \sin(\psi) - 10 \sin(2\psi)$ , the diffusion term  $D^{(2)}(\psi) = \lambda^2/2 = 1$ , and the effective potential  $U(\psi) = -2 \cos(\psi) - 5 \cos(2\psi)$  compare well with the numerical estimates. See Figures 4.5 and 4.6 for more details.

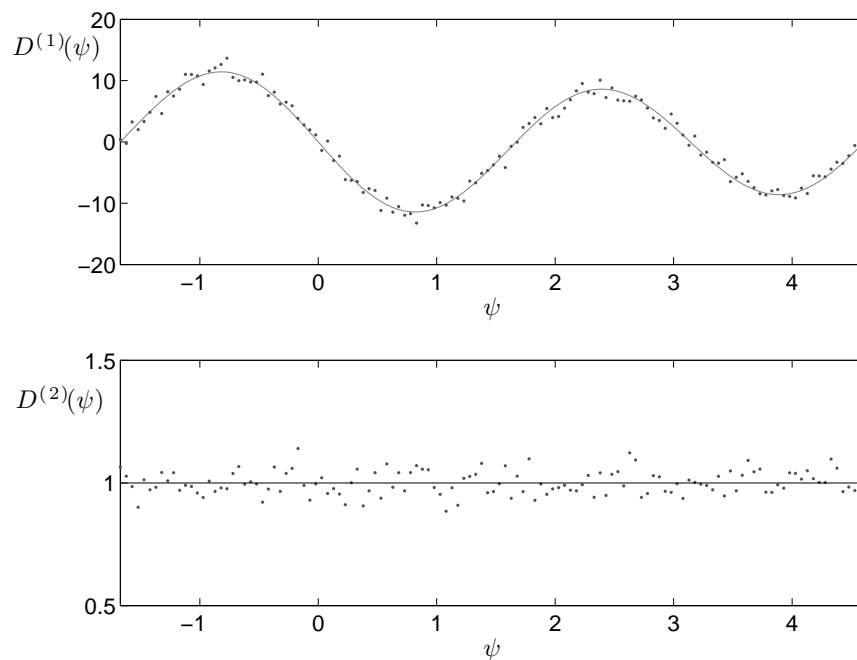


Figure 4.5: Top: (Solid) Drift term in the Fokker-Planck equation  $D^{(1)}(\psi) = g(\psi) = -2 \sin(\psi) - 10 \sin(2\psi)$ . (Dots) Estimate of the drift term in the Fokker-Planck equation using ensembles of appropriately initialized short-time simulations. Bottom: (Solid) Diffusion term in the Fokker-Planck equation  $D^{(2)} = 1$ . (Dots) Estimate of the diffusion term in the Fokker-Planck equation using ensembles of appropriately initialized short-time simulations

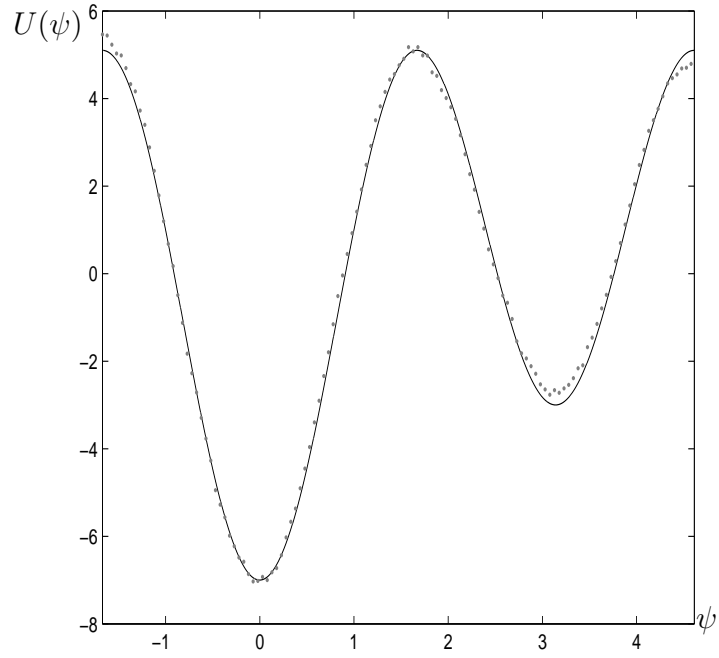


Figure 4.6: (Solid)  $U(\psi) = -2 \cos(\psi) - 5 \cos(2\psi)$  on the  $2\pi$  periodic interval  $(a, b) = (-\cos^{-1}(-1/10), -\cos^{-1}(-1/10) + 2\pi)$ . (Dots) Drift and Diffusion terms were estimated by initializing ensembles of short-time simulations with a given  $\psi = \psi_0$  by taking  $(\theta_1, \theta_2) = (\psi_0, 0)$  as an initial condition in equations (4.14). The effective potential  $U(\psi)$  was then estimated using equation (4.25).

## 4.4 Conclusion

For a continuous-time kinetic model of two agents moving in the plane with unit speed, we have shown that bistability between different collective states can be achieved solely through the choice of the coupling function for the control of the phase dynamics. These collective states are the  $S_2$  symmetric state, in which agents instantaneously have the same orientations, and the  $Z_2$  symmetric state, in which agents instantaneously have opposite orientations. Depending on the natural oscillator frequency associated with the phase control, in these states the agents could either be moving in straight lines or in circles.

We have demonstrated how the coarse-grained equation-free computational framework can be used to quantify the collective dynamics of the two agent system in terms of the coarse variable  $\psi = \theta_1 - \theta_2$ . Since equations at both the coarse and fine level are explicitly known, this system provides a nice “test of concept” for equation-free numerical methods. Analytical expressions for the drift and diffusion terms in the Fokker-Planck equation compare well with estimates obtained using appropriately initialized short-time simulations of the fine-scale equations.

# Chapter 5

## Optimal Switching between Coexisting Collective Motion States

### 5.1 Introduction

As shown in Chapter 4, for the coupled oscillator model for collective motion, it is possible to choose a coupling function so that both the  $S_2$  and  $Z_2$  phase-locked states are stable. In this chapter, we show in such a situation how the steering control for one of the agents can be modified to optimally switch from one of these states to the other. Existence and uniqueness of the optimal input is proven and a transition time symmetry between switching problems identified. The properties of the optimal inputs are interpreted by considering the phase-space geometry of

the Euler-Lagrange equations associated with the optimization. We illustrate the results with a coupling function chosen such that the  $S_2$  and  $Z_2$  states are bistable.

## 5.2 Optimal Switching

Consider two agents with steering control laws given by

$$\dot{\theta}_1 = \omega + Kf(\theta_2 - \theta_1) + I(t) \equiv u_1, \quad (5.1)$$

$$\dot{\theta}_2 = \omega + Kf(\theta_1 - \theta_2) \equiv u_2^0. \quad (5.2)$$

We will show how to find the input  $I(t)$  which takes the system from the stable  $S_2$  state at  $t = 0$  to the stable  $Z_2$  state at a specified time  $t = t_1$  and minimizes the  $L^2$  norm of the input

$$G[I(t)] \equiv \int_0^{t_1} [I(t)]^2 dt. \quad (5.3)$$

(Similarly, we consider optimal switching from the  $Z_2$  state to the  $S_2$  state.) The  $L^2$  norm has been suggested in a slightly different context [49] as an appropriate measure for steering “energy” (defined as the  $L^2$  norm of steering control) which is an important quantity to minimize when designing steering laws for unmanned aerial vehicle applications. For our purposes, this norm has the desirable property that smaller inputs are considered to be better. A similar approach, however, could be done for other appropriate cost functions of the input  $I(t)$ .

Letting  $\psi = \theta_1 - \theta_2$  as before, (5.1,5.2) become

$$\dot{\psi} = K(f(-\psi) - f(\psi)) + I(t) \equiv Kg(\psi) + I(t). \quad (5.4)$$

Next, we apply calculus of variations to minimize [29]

$$C[I(t)] = \int_0^{t_1} \underbrace{\left\{ [I(t)]^2 + \lambda \left( \frac{d\psi}{dt} - Kg(\psi) - I(t) \right) \right\}}_{P[I(t)]} dt, \quad (5.5)$$

with  $\lambda$  being the Lagrange multiplier associated with requiring that the dynamics satisfy (5.4). The associated Euler-Lagrange equations are

$$\frac{\partial P}{\partial I} = \frac{d}{dt} \left( \frac{\partial P}{\partial \dot{I}} \right), \quad \frac{\partial P}{\partial \lambda} = \frac{d}{dt} \left( \frac{\partial P}{\partial \dot{\lambda}} \right), \quad \frac{\partial P}{\partial \psi} = \frac{d}{dt} \left( \frac{\partial P}{\partial \dot{\psi}} \right),$$

giving

$$I(t) = \lambda(t)/2, \quad (5.6)$$

$$\frac{d\psi}{dt} = Kg(\psi) + I(t) = Kg(\psi) + \lambda/2, \quad (5.7)$$

$$\frac{d\lambda}{dt} = -K\lambda g'(\psi). \quad (5.8)$$

To find the optimal  $I(t)$  to switch from the  $S_2$  state to the  $Z_2$  state, (5.7) and (5.8) need to be solved subject to the conditions  $\psi(0) = 0, \psi(t_1) = \pi$ . Similarly, to find the optimal  $I(t)$  to switch from the  $S_2$  state to the  $Z_2$  state, (5.7) and (5.8) need to be solved subject to the conditions  $\psi(0) = \pi, \psi(t_1) = 2\pi$ . This requires that we find the appropriate initial condition  $\lambda(0) \equiv \lambda_0$ , which can be done with numerical methods such as the shooting method. The solution  $(\psi(t), \lambda(t))$  using this initial condition can then be used in (5.6) to give the optimal input  $I(t)$ .

Before solving the Euler-Lagrange equations for a specific example, we give some useful general results. First, equations (5.7,5.8) have the symmetry property that if  $(\psi(t), \lambda(t))$  is a solution, then so is  $(-\psi(t), -\lambda(t))$ . This follows from the fact that  $g(-\psi) = -g(\psi)$ . Since such trajectories are related by symmetry, we associate

them with each other below. Second, the Hamiltonian function

$$H(\psi, \lambda) = K\lambda g(\psi) + \lambda^2/4 \quad (5.9)$$

is conserved on trajectories for the Euler-Lagrange equations (5.7,5.8), as can be readily verified. This Hamiltonian was obtained using the Legendre transformation [33]. We will be interested in trajectories with  $\psi = 0$  or  $\psi = \pi$  at  $t = 0$ . Since  $g(0) = g(\pi) = 0$ , the relationship between  $\lambda_0$  and the initial value of the Hamiltonian,  $H_0$ , is

$$H_0 = \lambda_0^2/4. \quad (5.10)$$

The fact that there are two possible values of  $\lambda_0$  for a given value of  $H_0$  follows from the reflection symmetry mentioned above. In the following, without loss of generality we consider solutions that always have  $\lambda_0 > 0$ .

Furthermore, equations (5.7,5.8) have two classes of fixed points  $(\psi_p, \lambda_p)$ . Those in the first class satisfy  $\lambda_p = 0$  and  $g(\psi_p) = 0$ , and since the eigenvalues of the Jacobian evaluated at these fixed points are  $\pm K g'(\psi_p)$  they are saddles. From (5.9), the stable and unstable manifolds of these fixed points lie on the curves  $\lambda = 0$  and  $\lambda/4 + K g(\psi) = 0$ . The other class of fixed points satisfy  $g'(\psi_p) = 0$  and  $K g(\psi_p) + \lambda_p/2 = 0$ . The eigenvalues of the Jacobian evaluated at these fixed points are  $\pm K \sqrt{g(\psi_p)g''(\psi_p)}$ , so that when  $g(\psi_p)$  and  $g''(\psi_p)$  have opposite signs, they are centers.

### 5.3 Existence and Uniqueness of $I(t)$

The techniques from [67] can be modified as follows to show the existence and uniqueness (modulo symmetries) of an optimal  $I(t)$  for *any* positive  $t_1$ . Let's assume that we are interested in the trajectory of (5.7,5.8) which goes from  $\psi = 0$  to  $\psi = \pi$  in the time  $t_1$  with  $\lambda_0 > 0$ ; a similar argument holds for the trajectory which goes from  $\psi = \pi$  to  $\psi = 2\pi$  with  $\lambda_0 > 0$ .

**Lemma 5.3.1.**  *$d\psi/dt$  is always strictly positive for trajectories of (5.7,5.8) with  $\psi(0) = 0$ ,  $\psi(t_1) = \pi$ , and  $\lambda_0 > 0$ .*

*Proof.* Consider a trajectory  $(\psi, \lambda)$  for  $0 \leq t \leq t_1$  which solves (5.7,5.8) with  $\psi(0) = 0$ ,  $\psi(t_1) = \pi$ , and  $\lambda_0 > 0$ . It follows from (5.7) that  $d\psi/dt = \lambda_0/2 > 0$  at  $t = 0$ . Suppose by contradiction that  $d\psi/dt < 0$  for some time  $\bar{t}$  with  $0 < \bar{t} < t_1$ . Since any trajectory in the phase plane cannot be self-intersecting, there must be a value of  $\psi$  for which there are three different values for  $\lambda$ . However, the trajectory must be a level set of  $H$ , which is quadratic in  $\lambda$  and hence can only have at most two different values for a given  $\psi$ . This is a contradiction and so the lemma follows. □

**Proposition 5.3.1.** *There exists a unique optimal input  $I(t)$  for any positive  $t_1$  (modulo symmetry related solutions).*

*Proof.* It follows from (5.9) that trajectories satisfy  $\lambda^2/4 + Kg(\psi)\lambda - H_0 = 0$ . Solving for  $\lambda$ , we find that  $\lambda = 2 \left[ -Kg(\psi) + \sqrt{[Kg(\psi)]^2 + H_0} \right]$ . Here we take the '+' solution since from Lemma 5.3.1,  $d\psi/dt = \lambda/2 + Kg(\psi) > 0$ . Then, the

transition time  $t_1$  from the  $S_2$  to the  $Z_2$  state may be written as

$$t_1 = \int_0^{t_1} dt = \int_0^\pi \frac{d\psi}{Kg(\psi) + \frac{\lambda}{2}} = \int_0^\pi \frac{d\psi}{\sqrt{[Kg(\psi)]^2 + H_0}}. \quad (5.11)$$

Therefore,

$$\frac{\partial t_1}{\partial H_0} = -\frac{1}{2} \int_0^\pi \frac{d\psi}{([Kg(\psi)]^2 + H_0)^{3/2}} < 0. \quad (5.12)$$

Thus  $t_1$  decreases monotonically as  $H_0$  increases. Recalling that  $H_0 = \lambda_0^2/4$ , we see that  $t_1$  decreases monotonically with  $\lambda_0 > 0$ . By choosing  $\lambda_0$  large, we get a solution with arbitrarily small  $t_1$ , and by choosing  $\lambda_0$  so that the denominator of (5.11) becomes arbitrarily small, we get a solution with arbitrarily large  $t_1$ .  $\square$

## 5.4 Transition Time Symmetry

In Section 5.3 we showed the existence and uniqueness of an optimal input  $I(t)$  to switch from the  $S_2$  state to the  $Z_2$  state in time  $t_1$ . This required that we find an appropriate initial condition  $(\psi(0) = 0, \lambda(0) = a)$  so that  $\psi(t_1) = \pi$ . Similarly, there also exists a unique  $I(t)$  to switch from the  $Z_2$  state to the  $S_2$  state in time  $t_2$ . Here we must find an appropriate initial condition  $(\psi(0) = \pi, \lambda(0) = b)$  so that  $\psi(t_2) = 2\pi$ . We now demonstrate a useful relationship between these switching problems.

**Proposition 5.4.1.** *If  $\lambda(0) = a$ , then  $\lambda(t_1) = a$ . Furthermore,  $t_1 = t_2$  whenever  $a = b$ .*

*Proof.* Recall that  $H$ , as defined in (5.9), is conserved for trajectories of (5.7,5.8).

Thus, for the trajectory with initial condition  $(\psi, \lambda) = (0, a)$ , at time  $t_1$  we have

$H(\pi, \lambda(t_1)) = (\lambda(t_1))^2/4 = H(0, a) = a^2/4 \equiv H_a$ . This implies that  $\lambda(t_1) = a$ .

Now, let  $H_b \equiv H(\pi, b)$ . The transition time  $t_1$  from  $S_2$  to  $Z_2$  and  $t_2$  from  $Z_2$  to  $S_2$

is

$$t_1 = \int_0^\pi \frac{d\psi}{\sqrt{[Kg(\psi)]^2 + H_a}}, \quad t_2 = \int_\pi^{2\pi} \frac{d\psi}{\sqrt{[Kg(\psi)]^2 + H_b}}.$$

Since  $g$  is a  $2\pi$ -periodic odd function,  $g(2\pi - \psi) = g(-\psi) = -g(\psi)$ ,  $(g(2\pi - \psi))^2 = g(\psi)^2$ . Thus, letting  $\phi = 2\pi - \psi$ ,

$$t_2 = - \int_\pi^0 \frac{d\phi}{\sqrt{[Kg(2\pi - \phi)]^2 + H_b}} = \int_0^\pi \frac{d\phi}{\sqrt{[Kg(\phi)]^2 + H_b}}.$$

Therefore, if  $H_a = H_b$ , or equivalently  $a = b$ , then  $t_1 = t_2$ . □

## 5.5 Example

We now illustrate how this optimal switching method is used for the coupling function (4.8) with  $A = B = 1$ , which gives stable  $S_2$  and  $Z_2$  solutions (see Figure 4.2). In this case,  $g(\psi) = -2\sin(\psi) - 2\sin(2\psi)$ . For definiteness, other parameters in the steering control laws are taken to be  $K = \omega = 1$ . (Note that the optimal  $I(t)$  is independent of  $\omega$ .)

To find the optimal  $I(t)$  to switch from the  $S_2$  state to the  $Z_2$  state (or from the  $Z_2$  state to the  $S_2$  state), the boundary value problem (5.7) and (5.8) with boundary conditions  $\psi(0) = 0, \psi(t_1) = \pi$  (resp.,  $\psi(0) = \pi, \psi(t_2) = 2\pi$ ) needs to be solved. The shooting method was used to compute the necessary initial value for  $\lambda$ , which is then used to obtain the optimal input  $I(t) = \lambda(t)/2$ . Figures 5.1 and 5.2 show the optimal input  $I$  for a range of times  $t_1$  and  $t_2$  with scaled time axis. As

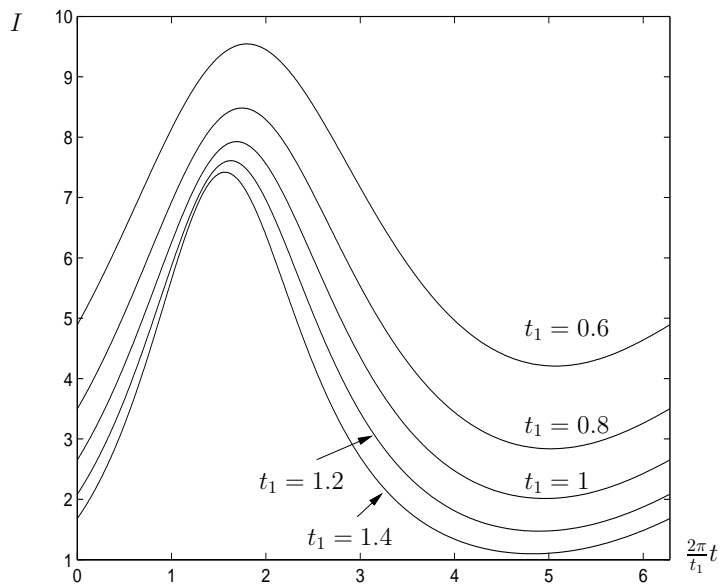


Figure 5.1: Optimal input  $I(t)$  for a variety of transition times  $t = 0.6, 0.8, 1, 1.2, 1.4$  from the  $S_2$  state to the  $Z_2$  state.

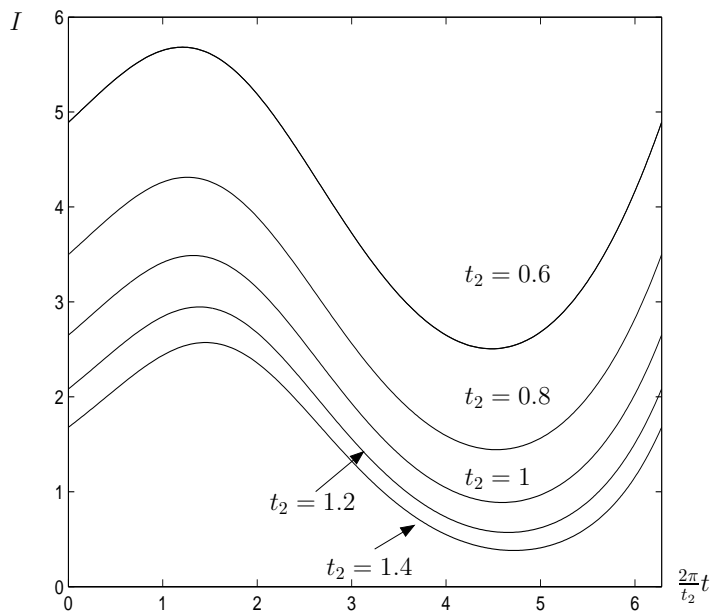


Figure 5.2: Optimal input  $I(t)$  for a variety of transition times  $t = 0.6, 0.8, 1, 1.2, 1.4$  from the  $Z_2$  state to the  $S_2$  state.

we showed in Proposition 5.4.1,  $\lambda_0$  and therefore  $I_0$  are the same when  $t_1 = t_2$ . In Figures 5.3 and 5.4, we show sample trajectories in phase space for  $\psi(0) = 0$  and  $\psi(0) = \pi$ . As expected, in order to obtain switching for large times the trajectories remain close to the stable and unstable manifolds of the fixed points with  $\lambda = 0$  and  $\psi = 0, \psi = \cos^{-1}(-1/2), \psi = \pi$ , and  $\psi = 2\pi$ .

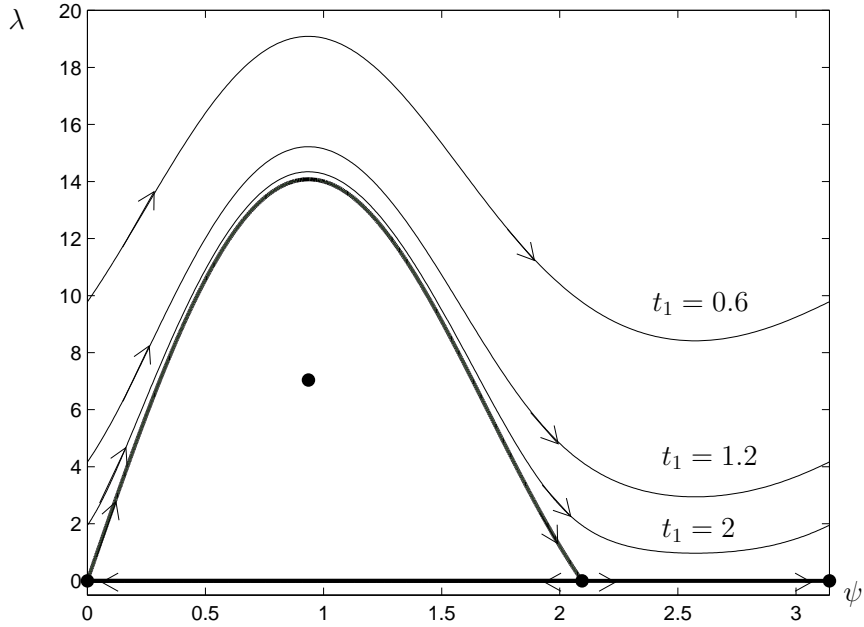


Figure 5.3: Sample trajectories in the  $(\psi, \lambda)$  plane transitioning from the  $S_2$  state ( $\psi = 0$ ) to the  $Z_2$  state ( $\psi = \pi$ ) in time  $t = 0.6, 1.2$ . As  $t$  increases, trajectories approach the stable and unstable manifolds of the fixed points  $\psi = 0, \psi = \arccos(-1/2), \psi = \pi$ .

One may follow the trajectories of the agents by integrating equation (4.1) with steering control given by equations (5.1,5.2). Figure 5.5 shows sample trajectories for agents optimally switching from the  $S_2$  to the  $Z_2$  state in time  $t_1 = 0.6$ . Both agents are initially placed at the origin  $(x, y) = (0, 0)$  with  $\theta_1 = \theta_2 = 0$  ( $\psi = 0$ ), so that each agent has initial velocity vector  $\dot{r}_1 = \dot{r}_2 = (1, 0)$ . After the appropriate

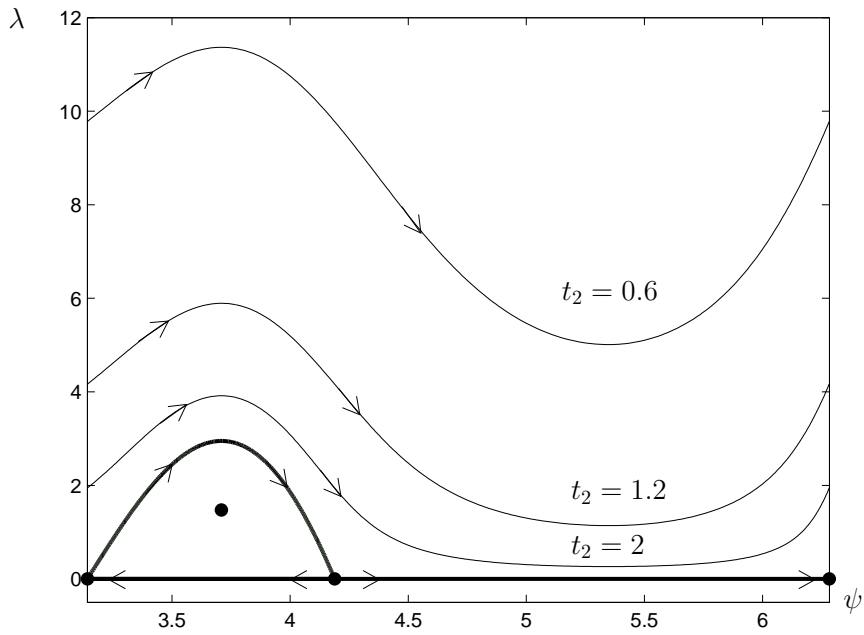


Figure 5.4: Sample trajectories in the  $(\psi, \lambda)$  plane transitioning from the  $Z_2$  state ( $\psi = 0\pi$ ) to the  $S_2$  state ( $\psi = 2\pi$ ) in time  $t = 0.6, 1.2$ . As  $t$  increases, trajectories approach the stable and unstable manifolds of the fixed points  $\psi = \pi, \psi = 2 \arccos(-1/2), \psi = 2\pi$ .

transition time  $t_1$ , the input  $I(t)$  is turned off so that agents remain in the  $Z_2$  state, following circular paths of radius 1 (since  $\omega = 1$ ) with constant phase difference  $\psi = \pi$ . Figure 5.6 shows sample trajectories for agents switching from the  $Z_2$  to the  $S_2$  state in time  $t_2 = 0.6$ . As in the previous case, agents are initially placed at the origin  $(x, y) = (0, 0)$ , but with  $\theta_1 = \pi$  and  $\theta_2 = 0$  so that  $\psi = \pi$ . After time  $t_2 = 0.6$ , the input  $I(t)$  is turned off and agents remain in the  $S_2$  state, following circular paths of radius 1 (since  $\omega = 1$ ) with the same phase.

Because we are using only phase control, in general the agents will end up tracing different circles after the optimal input  $I(t)$  is turned off.

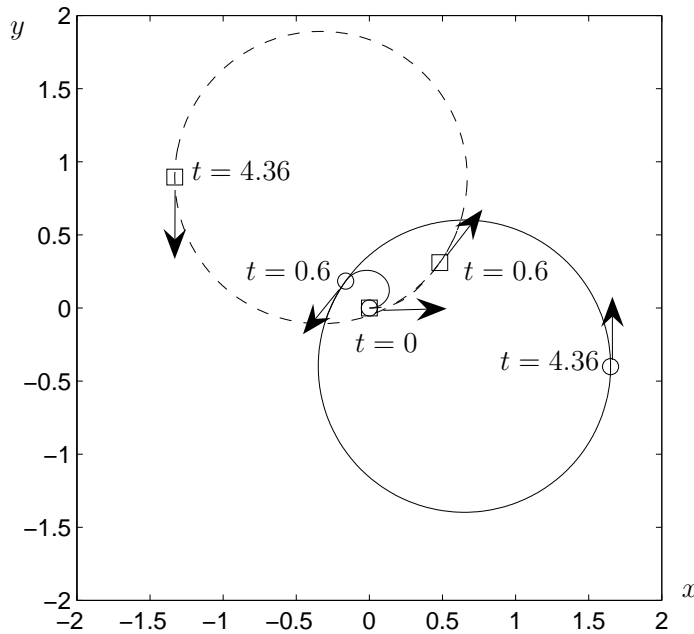


Figure 5.5: Sample path of agents in the  $(x, y)$  plane for optimal switching from the  $S_2$  state ( $\psi = 0$ ) to the  $Z_2$  state ( $\psi = \pi$ ) in time  $t = 0.6$ . Both agents start at the origin at  $t=0$  with  $\theta_1 = \theta_2 = 0$  ( $\psi = 0$ ) and end at  $t = 0.6$  with  $\psi = \pi$ . After  $t = 0.6$ , agents follow circular paths of radius 1 (since  $\omega = 1$ ) with constant phase difference of  $\psi = \pi$ .

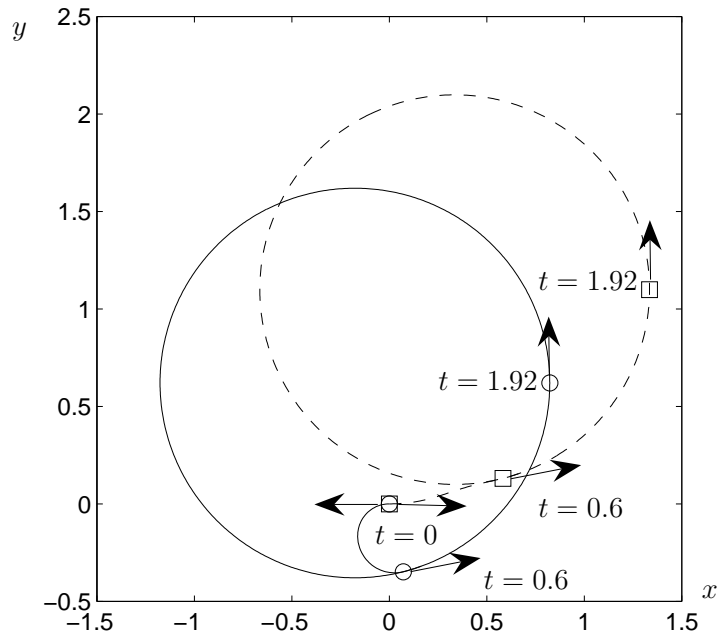


Figure 5.6: Sample path of agents in the  $(x, y)$  plane for optimal switching from the  $Z_2$  state ( $\psi = \pi$ ) to the  $S_2$  state ( $\psi = 0$ ) in time  $t = 0.6$ . Both agents start at the origin at  $t=0$  with  $\theta_1 = \pi, \theta_2 = 0$  ( $\psi = \pi$ ) and end at  $t = 0.6$  with  $\psi = 0$ . After  $t = 0.6$ , agents follow circular paths of radius 1 (since  $\omega = 1$ ) with constant phase difference of  $\psi = 0$ .

## 5.6 Conclusion

Variational methods were used to determine the optimal input to the steering control of one of the agents which leads to switching between two collective states, an “in phase” ( $S_2$ ) and a “splay” ( $Z_2$ ) state. Here optimality refers to minimization of the square-integral measure of the input. For any given time interval of switching, such an optimal input was shown to exist and to be unique, provided symmetry-related solutions are associated. Furthermore, a transition time symmetry was identified which relates the optimal inputs for transitions from the  $S_2$  to the  $Z_2$  symmetric state to the optimal inputs for transitions from the  $Z_2$  to the  $S_2$  symmetric state. Finally, the properties of optimal inputs were interpreted by considering the phase space geometry of the Euler-Lagrange equations associated with the optimization.

We have considered optimal inputs which lead to switching over a specified time interval. Such switching has a nice robustness property: if the input simply puts the system into the basin of attraction of the desired state, the system’s natural dynamics will lead to an asymptotic approach to the desired state. Provided noise and uncertainties in model parameters are not too large, one thus expects that the inputs considered in this chapter will robustly lead to successful switching, although not exactly in the desired amount of time.

Many biological models of collective motion show that animal groups do not necessarily change their behavioral rules to switch between collective states, see, e.g., Chapters 2 and 3. The model studied in this Chapter demonstrates a robust

mechanism for which a member of a school can induce switching between states, without a change to the basic rules of motion, or the knowledge of the rest of the members of the school.

We hope that the techniques used in this Chapter can be extended to other collective motion systems which display bistability, including bistability between other states and systems composed of a larger number of agents. In particular, using the expressions for the eigenvalues of globally coupled oscillator systems derived in [4, 9], it is possible to choose coupling functions such that the  $S_N$  and  $Z_N$  states are bistable. Also, for  $N \geq 3$  agents it is possible to have periodic orbits in the steering control subsystem stably coexisting with phase-locked solutions [52]. Optimal switching between coexisting stable states for such  $N$  agent systems would lead to higher dimensional optimization problems which could be numerically solved with gradient methods.

# Chapter 6

## Spatial Position and Information

## Transfer in a Schooling Model

### 6.1 Introduction

For the one-dimensional individual-based schooling model studied in Chapter 2, we found that groups may stochastically switch between two ordered collective states. Such switching typically begins with a change in the heading of an individual near the edge of the school which then “propagates” throughout the entire school. In this Chapter, we investigate the relationship between spatial position and information transfer for a two-dimensional individual-based schooling model. We begin by introducing the schooling model and then analyze the steady-state dynamics using a few coarse-observables. For efficiency, simulations are performed in parallel on a programmable graphics processing unit. Finally, we use a cross-

correlation function to measure the average response of a school to perturbations in the headings of individual members. We relate the length and strength of response to the spatial positions of the individuals perturbed. Our results show that leaders, i.e., individuals at the front of the school, do not necessarily propagate information most efficiently. This significantly changes current assumptions regarding the costs and benefits of spatial positions in animal groups.

## 6.2 The Model

We consider a two-dimensional individual-based model for schooling fish in which interactions take place within two behavioral zones. This type of model was considered in [18] with an *informed* leader. Here we assume there is no informed leader, so that the group is self-organizing, and explore the effects of different weights of orientation and attraction response on the schooling behavior.

In the model, groups are composed of  $N$  individuals with positions  $p_i(t) \in \mathbb{R}^2$  and unit directions  $\hat{v}_i(t) \in \mathbb{R}^2$ . Individuals travel at constant speed  $s$  and have finite maximum turning rate  $\theta$ . Every time step  $\tau$ , individuals simultaneously determine a new direction of travel by considering neighbors within two behavioral zones. The first zone, a “zone of repulsion”, is represented by a circle of radius  $r_r$  centered about the individual. Individuals repel away from agents within their zone of repulsion. The second zone, a “zone of orientation and attraction”, is represented by an annulus of inner radius  $r_r$  and outer radius  $r_p = r_r + \Delta r_p$  about the individual, excluding a blind area behind the individual, defined as a circular

sector with interior angle  $(2\pi - \eta)$  for which neighbors are undetectable. Individuals align with and are attracted towards neighbors within their zone of orientation and attraction.

These zones are used to define the following behavioral rules of motion. If individual  $i$  finds agents within its zone of repulsion, then it orients its direction away from the average relative directions of those agents. Its desired direction of travel in the next time step is given by the sum

$$v_i(t + \tau) = - \sum_{j \neq i} \frac{p_j(t) - p_i(t)}{|p_j(t) - p_i(t)|}. \quad (6.1)$$

The desired direction of travel of agent  $i$  is normalized as  $\hat{v}_i(t + \tau) = \frac{v_i(t + \tau)}{|v_i(t + \tau)|}$ , assuming  $v_i(t + \tau) \neq 0$ . If  $v_i(t + \tau) = 0$ , then agent  $i$  maintains its previous direction of travel as its desired direction of travel, giving  $\hat{v}_i(t + \tau) = \hat{v}_i(t)$ .

If individual  $i$  does not find agents within its zone of repulsion, then it aligns with (by averaging the directions of travel of itself and its neighbors) and feels an attraction towards (by orienting itself towards the average relative directions of) agents within its zone of orientation and attraction. Its desired direction of travel is given by the weighted sum of two terms:

$$v_i(t + \tau) = \omega_a \frac{a_i(t)}{|a_i(t)|} + \omega_o \frac{o_i(t)}{|o_i(t)|}, \quad (6.2)$$

where  $\omega_o$  and  $\omega_a$  are the weightings of the orientation and attraction terms respectively, and

$$a_i(t) = \sum_{j \neq i} \frac{p_j(t) - p_i(t)}{|p_j(t) - p_i(t)|}, \quad o_i(t) = \sum_j \hat{v}_j(t). \quad (6.3)$$

The desired direction of travel of agent  $i$  is normalized as  $\hat{v}_i(t + \tau) = \frac{v_i(t+\tau)}{|v_i(t+\tau)|}$ , assuming  $v_i(t + \tau) \neq 0$ . As before, if  $v_i(t + \tau) = 0$ , then agent  $i$  maintains its previous direction of travel as its desired direction of travel.

We denote  $r = \omega_o/\omega_a$  as the ratio of orientation and attraction tendencies. For  $r < 1$  ( $\omega_a > \omega_o$ ), individuals are more interested in attraction towards their neighbors than orientation with them. For  $r = 1$ , orientation and attraction influences are weighted equally ( $\omega_o = \omega_a$ ). For  $r > 1$  ( $\omega_o > \omega_a$ ), individuals are more interested in orientation with their neighbors than attraction towards them.

Noise effects are incorporated into the model by rotating agent  $i$ 's desired direction  $\hat{v}_i(t + \tau)$  by an angle drawn from a circularly wrapped normal distribution with mean 0 and standard deviation  $\sigma$ . Also, since individuals can only turn  $\theta\tau$  radians in one timestep, if the angle between  $\hat{v}_i(t)$  and  $\hat{v}_i(t + \tau)$  is greater than  $\theta\tau$ , individuals do not achieve their desired direction, and instead rotate  $\theta\tau$  towards it. Finally, each agent's position is updated simultaneously as

$$p_i(t + \tau) = p_i(t) + s\hat{v}_i(t + \tau)\tau \quad i = 1, \dots, N. \quad (6.4)$$

To begin a simulation, individuals are placed in a bounded region with randomized positions and directions of travel. The simulation is run 3000 time steps until the schooling behavior has reached steady-state.

To accurately determine the statistical properties of the collective motion of fish whose dynamics are described by such a model, many steady-state simulations are required. Simulations of the individual-based model can be quite costly and can benefit from parallel processing. In the model, each agent updates its direction

of travel based on the positions and directions of travel of all other agents. This computation can be performed in parallel across individuals within a single realization. In addition, replicate steady-state simulations can be performed in parallel across realizations. Both are data-parallel computations in which the same instructions are executed on multiple data elements in parallel. We used a programmable Graphics Processing Unit (GPU) to perform simulations of the model in parallel. For further information, see Appendix D.

### 6.3 Observables

Two observables are used to measure the structure of the schools: elongation and polarization. Group elongation is computed by forming the smallest bounding box that contains the school and taking the ratio of the length of the axis of the bounding box aligned with group motion to the axis perpendicular to group motion [18]. When a school is equally wide as it is long,  $E(t) = 1$ . For our steady-state schooling simulations typically  $E \geq 1$ . Polarization,

$$P(t) = \frac{1}{N} \left| \sum_{i=1}^N \hat{v}_i(t) \right|, \quad (6.5)$$

measures the degree of group alignment. If all individuals within a school adopt the same heading,  $P(t) = 1$ , while if their headings balance out,  $P(t) = 0$ . Thus,  $P(t)$  takes values in the range  $[0, 1]$ . To obtain statistics regarding the group structure for a given size set of parameters, 1000 steady-state simulations (with different initial conditions) were run on the GPU for 3000 time steps. The average group elongation

and polarization were recorded as well as the probability of group fragmentation. A group is defined to be fragmented when it is composed of two or more non-interacting subgroups.

In addition to these observables, we measure a schools directional memory with an average heading autocorrelation function. Specifically, define the average group heading as

$$\hat{v}_{av} = \sum_{i=1}^N \hat{v}_i / \left| \sum_{i=1}^N \hat{v}_i \right|. \quad (6.6)$$

Then, the average heading autocorrelation function is defined as

$$A(t) = \langle \hat{v}_{av}(t) \cdot \hat{v}_{av}(0) \rangle, \quad (6.7)$$

where  $\langle \cdot \rangle$  denotes an ensemble average over replicate simulations. Note that  $\hat{v}_{av}(0)$  refers to the initial average heading of a *steady-state* school which has already been simulated for 3000 time steps. The average heading autocorrelation function measures the correlation of the schools initial heading with its current heading as a function of time. At time  $t = 0$ ,  $A(t) = \langle \hat{v}_{av}(0) \cdot \hat{v}_{av}(0) \rangle = 1$ . As  $t$  increases,  $A(t)$  typically decreases towards zero as the school “forgets” its direction of travel.

## 6.4 Simulation Statistics

We fix  $r_r = 1$ ,  $\Delta r_p = 6$ ,  $\eta \approx 6.1$  radians (350 degrees),  $s = 1/\text{sec}$ ,  $\tau = 0.2$  sec,  $\sigma = 0.01$ , and  $\theta \approx 2$  radians (115 degrees). We consider schools of size  $N \in [10, 150]$  and explore the effects of varying  $r = \omega_o/\omega_a$ , the ratio of orientation to attraction weights. For  $r$  near zero, individuals weight attraction much more than orienta-

tion, and swarming behavior persists. Groups are cohesive with low polarization and elongation that is close to 1 (groups are as wide as they are long). As  $r$  is increased, orientation influences become stronger and groups become increasingly more polarized. For  $r$  just past 1, groups become more elongated along their principle axis of motion. Elongation reaches a maximum when orientation weightings are approximately twice that of attraction weightings ( $r \approx 2$ ) and then decreases. Figure 6.1 shows the average group polarization, average group elongation, and probability of group fragmentation statistics for schools of size  $N = 25, 50, 100, 150$  averaged over 1000 replicates at steady-state.

For  $N$  small, the probability of fragmentation is nearly zero for all ratios  $r$  considered. This is due to the fact that when  $N$  is small, the size of the interaction zones is large in comparison to the size of the school, and thus the probability that an individual (or group of individuals) will lose all interaction with the school and fragment is extremely low. For larger size schools, the probability of fragmentation is nearly zero when  $r < 1$  ( $\omega_a > \omega_o$ ). When  $r \geq 1$ , the probability of fragmentation is non-zero. It is interesting to note that the probability of fragmentation is *not* simply a monotonically increasing function of  $r$ . For schools of size  $N = 100$ , for example, for  $r$  just past 1, there is a relatively rapid increase in the probability of fragmentation, reaching a peak probability of 0.28 at  $r = 1.4$ . In this parameter regime, schools are more than twice as long as they are wide and are not highly polarized. Fragmentation seems to take place as a pinching process from a narrow point in a school. When such a weak point exists, and polarization is not extremely

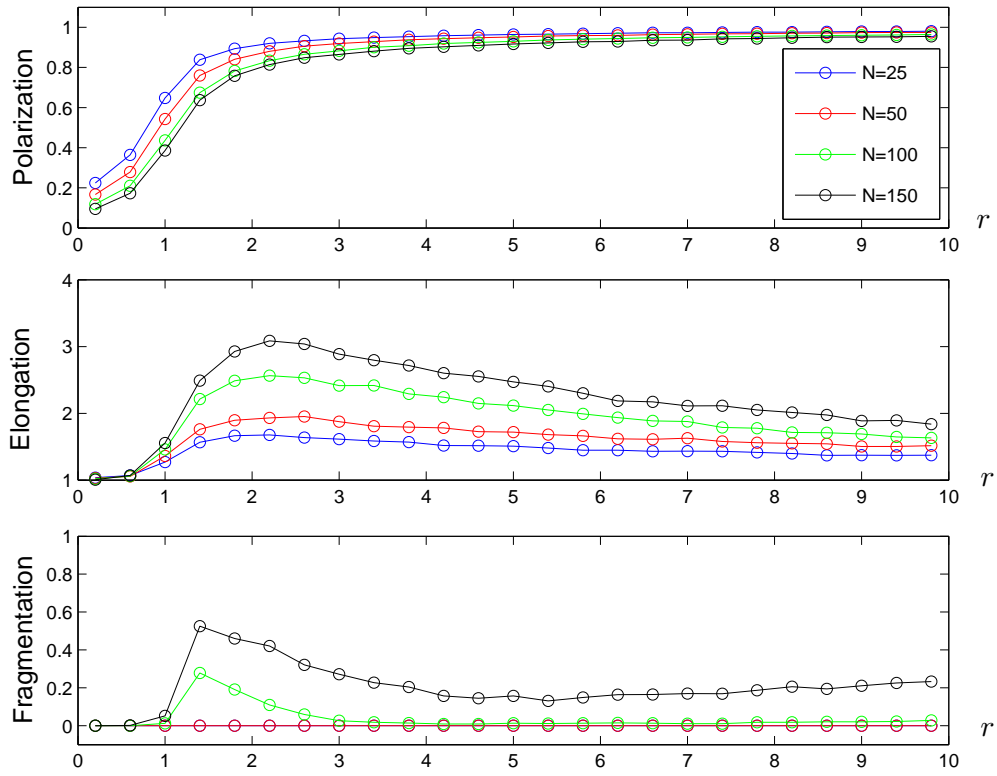


Figure 6.1: Average group polarization, elongation, and probability of fragmentation as a function of  $r$ , the ratio of orientation to attraction weightings, for schools of size  $N = 25, 50, 100, 150$  for the local zone-based schooling model. For schools of size  $N = 25, 50$ , the probability of fragmentation is zero for all values of  $r$ .

high, the school may fragment into subgroups, each adopting different average directions of travel. For larger  $r$ , the probability of fragmentation naturally increases as individuals weight attraction to their neighbors much less than alignment. See Figure 6.2 for examples of fragmentation when  $r = \omega_o/\omega_a = 1.25, 64$ . For all values of  $r$ , the probability of fragmentation increases with simulation time.

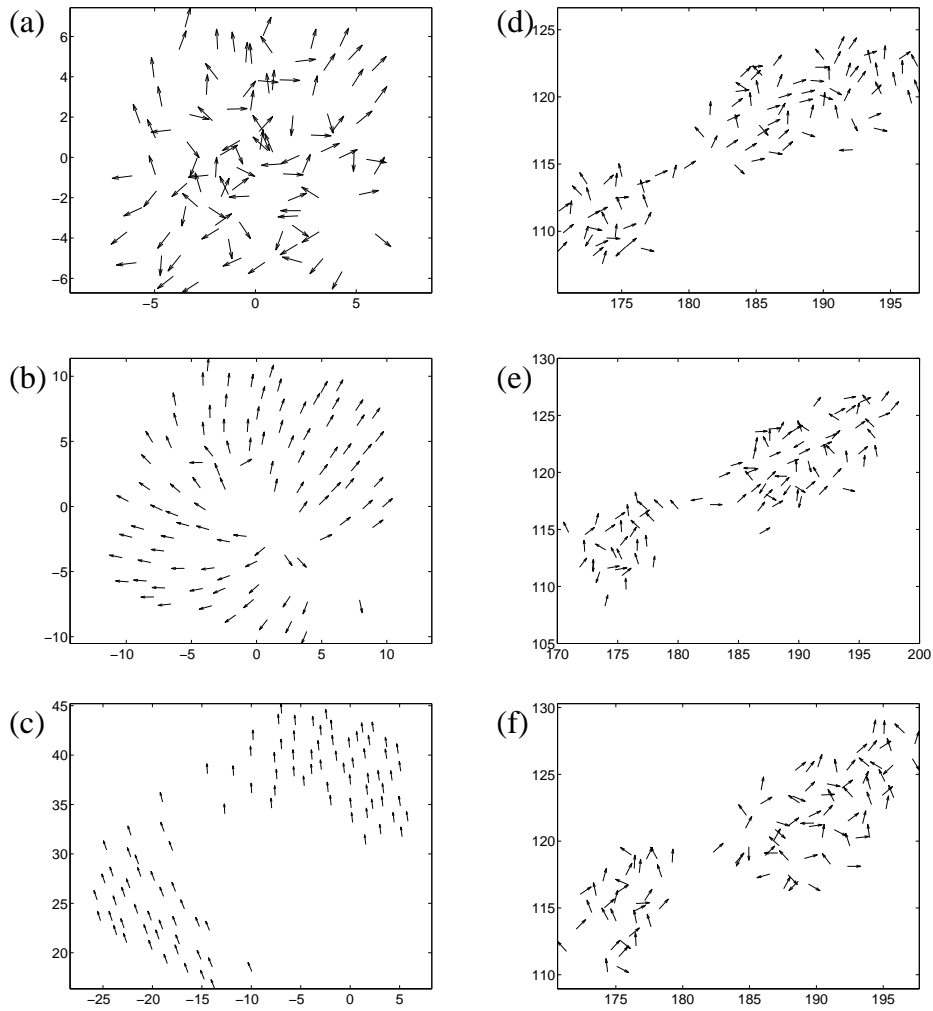


Figure 6.2: (Left panel) Illustration of fragmentation for  $\Delta r_p = 5, r = \omega_o/\omega_a = 64$ . Snapshots of a school at time (a)  $t=10$ , (b)  $t=30$ , and (c)  $t=200$ . (Right panel) Illustration of fragmentation for  $\Delta r_p = 6, r = \omega_o/\omega_a = 1.25$ . Snapshots of a school at time (d)  $t=2740$ , (e)  $t=2760$ , and (f)  $t=2770$ .

Figure 6.3 shows the average heading autocorrelation functions for  $r = 4, 16, 64$  averaged over 1000 different steady-state schools for  $t = 10^4$  steps. The autocorrelation functions seem to decay exponentially with time, i.e., as  $e^{-\lambda t}$ . This is characteristic of an Ornstein-Uhlenbeck process. Thus, we can think of the variable  $v_{av}(t)$  as a stochastic variable with autocorrelation time  $1/\lambda$ . For  $r = 4, 16$ , the autocorrelation functions fit well to exponentials with characteristic times  $1/\lambda \approx 596, 1196$ . Thus, as schools become more polarized, they retain memory of their average headings for longer times. For  $r = 64$ , the autocorrelation function does not fit well to a single exponential. This is most likely due to the fact that the probability of fragmentation when  $r = 64$  is non-zero (nearly 8 percent at  $t = 3000$ ) and increases as a function of simulation time.

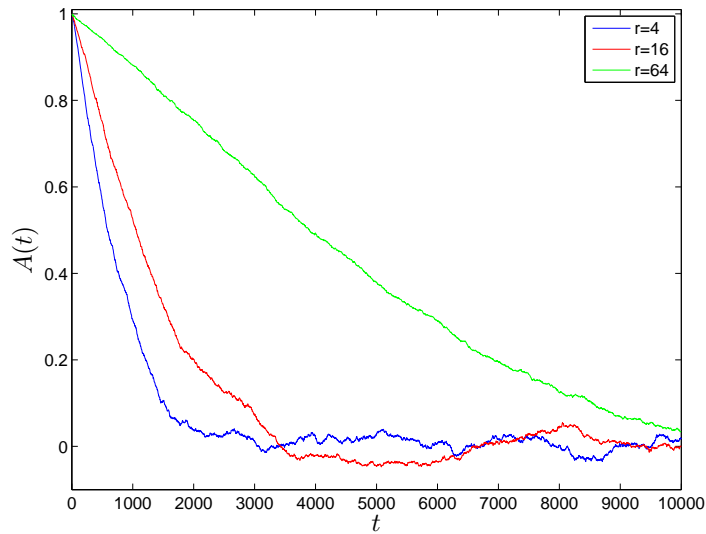


Figure 6.3: Average heading autocorrelation functions for the schooling model with  $r = 4, 16, 64$  averaged over 1000 replicates for  $10^4$  time steps.

## 6.5 Spatial Position and Information Transfer

In this section, we measure the response of a school to internal perturbations with a cross-correlation function and relate this to the location of the perturbation. We begin by ranking individuals within a school. Define the center of mass of the school as  $p_{av} = \frac{1}{N} \sum_{i=1}^N p_i$ . As in [18], for each steady-state school, individuals are ranked according to their signed distance to the plane through  $p_{av}$  with normal direction  $\hat{v}_{av}$ . It follows that individuals near the front of the school have rank close to 1, while individuals near the back of the school have rank close to  $N$ .

### 6.5.1 Perturbing a Single Individual

We rotate the heading of a single individual of rank  $i$  in a steady-state school by 90 degrees counterclockwise (with respect to their initial heading) and measure the correlation of the average heading of the school with the perturbed heading of the individual as a function of time. More specifically, define the cross-correlation function  $C(t, i)$  as

$$C(t, i) = \langle \hat{v}_{av}(t) \cdot \hat{v}_p^i(0) \rangle = \langle \cos(\theta) \rangle, \quad (6.8)$$

where  $\langle \cdot \rangle$  denotes an ensemble average over replicate simulations,  $\hat{v}_p^i$  is the perturbed heading of a fish of rank  $i$ , and  $\theta$  is the angle between  $\hat{v}_{av}(t)$  and  $\hat{v}_p^i(0)$ .  $C(t, i)$  is a measure of the sensitivity of a school to perturbations of individual members located at rank  $i$  within a school. Note that  $C$  takes values in the range  $[-1, 1]$  and by definition  $C(0, i) = 0$ . When  $C > 0$ , the schools heading has on average adjusted to be closer to the heading of the perturbed individual (positive correlation), while

when  $C < 0$ , the schools heading has on average adjusted to be further away from the heading of the perturbed individual (negative correlation).

In the following, we consider schools of size  $N = 100$ , and consider  $r$  in the range  $[0.25, 64]$ . To measure the sensitivity of a school to perturbations as a function of location, we divide the school into four quartiles: front (rank 1 – 25), front-middle (rank 26 – 50), middle-back (rank 51 – 75) and back (rank 76 – 100). We then compute the mean response to perturbations in each of the four quartiles,  $\overline{C}(t)$ , by averaging over individuals of rank in the range  $[j, j + k]$  where  $k = 24$  and  $j = 1, 26, 51, 76$ .

The right panel of Figure 6.4 shows for schools of size  $N = 100$  with  $r = 4$  ( $P \approx 0.91$ ,  $E \approx 2.3$ ),  $r = 16$  ( $P \approx 0.98$ ,  $E \approx 1.5$ ), and  $r = 64$  ( $P \approx 1.0$ ,  $E \approx 1.5$ ), the average response to an internal perturbation  $\overline{C}(t)$ . The correlation functions were averaged over 1000 replicates in each of the four quartiles. The left panel of the figure shows sample schools prior to the perturbation colored according to rank.

In all cases, there seem to be multiple time scales of information transfer and loss as measured by the cross-correlation function  $\overline{C}(t)$ . On the fast time scale, lasting approximately 10-20 timesteps (2-4 seconds real time), the school's average heading rapidly becomes more correlated with the initial heading of the perturbed individual. This corresponds to a first burst of information transfer.

Over longer time scales, there are secondary responses. For  $r = 4$ , the secondary response has almost as large an impact on the heading of the school as the initial and varies strongly with the location of the perturbation. For the middle quartiles

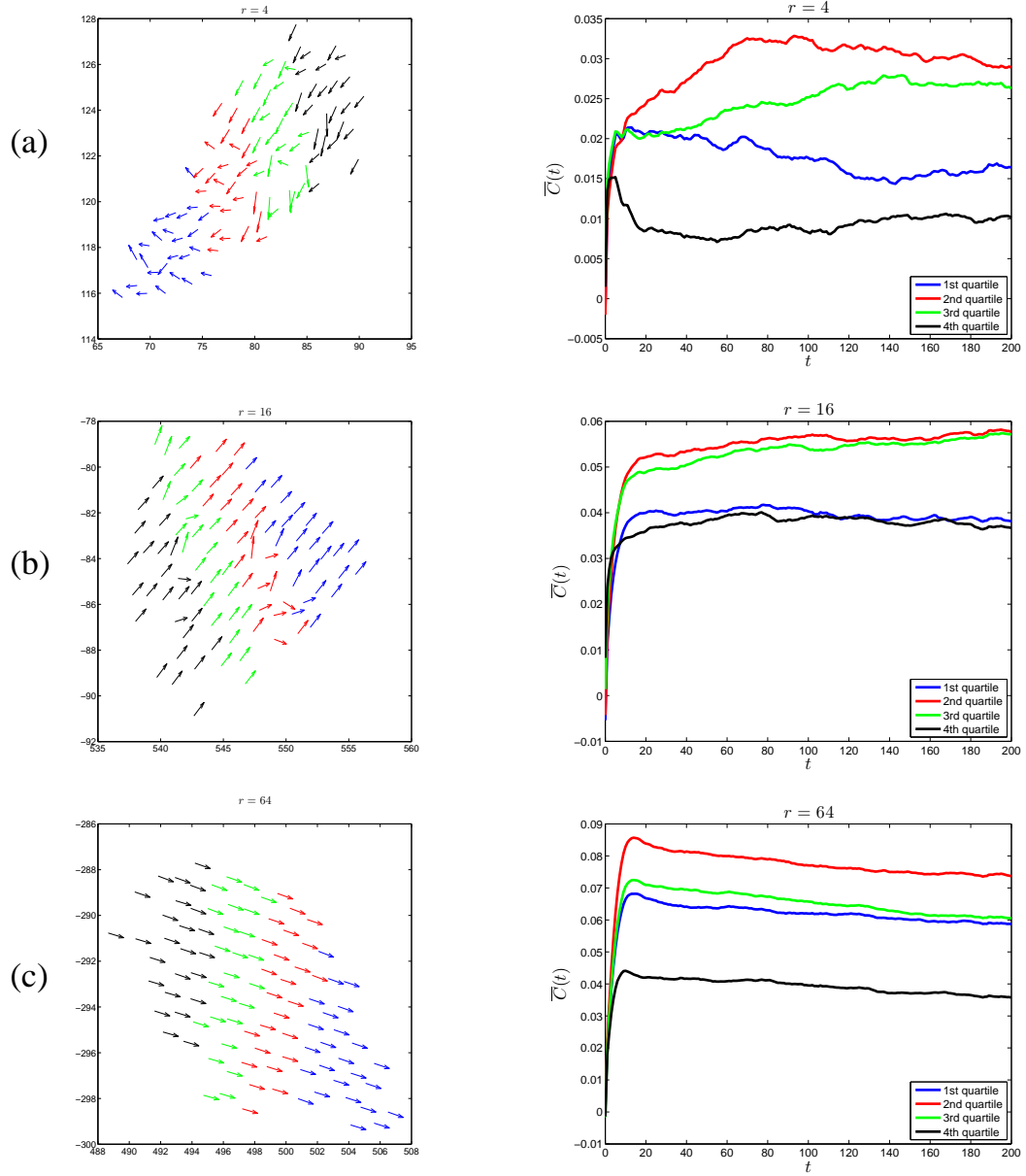


Figure 6.4: Left panel:  $N = 100$  member schools simulated using the local zone model with (a)  $r = 4$  ( $P \approx 0.91$ ,  $E \approx 2.3$ ), (b)  $r = 16$  ( $P \approx 0.98$ ,  $E \approx 1.5$ ), and (c)  $r = 64$  ( $P \approx 1.0$ ,  $E \approx 1.5$ ), all colored according to rank. Right panel: Cross-correlation functions  $\overline{C}(t)$  averaged over 1000 replicates in each of the four quartiles.

(2nd and 3rd), the secondary response appears to be information transfer at a slower rate, while for the front and back quartiles, it seems to be information loss. For  $r = 16$ , after the initial burst of information transfer,  $\overline{C}(t)$  does not make any large gains or losses. For the middle quartiles, there is a small rise in correlation, while for the front and back quartiles there is a small decline in correlation. For  $r = 64$ , after the initial burst of information transfer, one can see a visible trend in information loss. Since schools naturally lose memory of their average direction of travel (as measured by the autocorrelation functions in section 6.4), we suspect the visible trend in information loss for  $r = 64$  is due to noise effects, and not a secondary burst of response.

In Figure 6.5, the peak correlation  $\overline{C}_{max}$  is plotted as a function of  $r$  for each of the four quartiles. Since  $\overline{C}_{max}$  is an increasing function of  $r$ , we may conclude that as schools become more polarized, they respond more strongly to internal perturbations. Thus, by changing local behavioral tendencies (adjusting  $r$ ), schools can tune themselves to be more or less sensitive to fluctuations. Individuals in the front-middle region (2nd quartile) induce the greatest response for all values of  $r$  considered. Individuals in the 1st and 3rd quartiles induce the next greatest response, with individuals in the 3rd quartile typically inducing a larger response. Not surprisingly, members in the 4th quartile at the rear of the school have the least effect.

It is assumed that among the benefits of adopting a frontal position, such as increased food consumption [56], is the ability to lead, i.e., to have more control

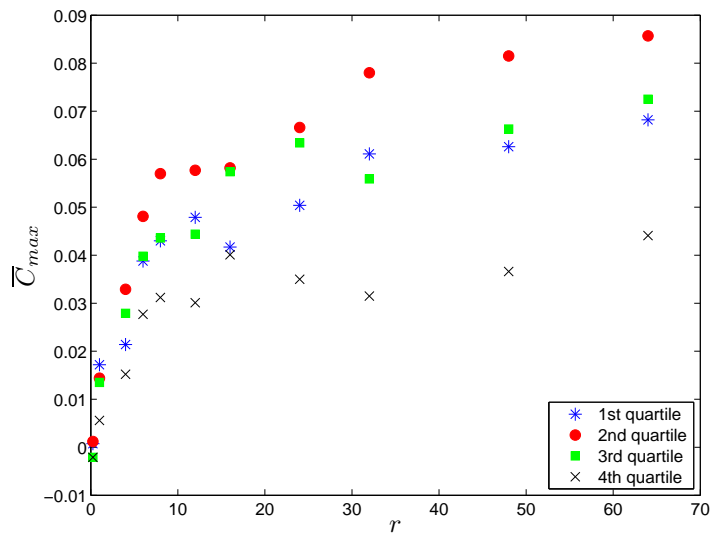


Figure 6.5: Peak correlation  $\overline{C}_{max}$  as a function of  $r$  for each of the four quartiles. Schools respond more strongly to perturbations from the 1st quartile. For all four quartiles,  $\overline{C}_{max}$  is an increasing function of  $r$ . Thus, schools that are more polarized respond more strongly to internal perturbations.

over the collective motion of the group. Our results show that individuals in the very front of the school do not necessarily transfer information most efficiently or have more “control” over group motion. Thus, the optimal position for leadership may not be a front, “lead” position, as previously assumed. There is evidence to support that individuals on the edges of a school may have an increased risk of predation since they are the first to run into danger [16]. Our results put into new perspective the benefits and drawbacks of adopting particular spatial positions within a school.

### 6.5.2 Perturbing Multiple Individuals

We now measure the response of a school to perturbations in the headings of multiple individuals. We consider spatially and temporally correlated perturbations (individuals from the same quartile at the same time) and just temporally correlated perturbations (individuals at the same time). We measure the response of the school to perturbations (rotation by 90 degrees counterclockwise) in the heading of two members with the cross-correlation function

$$C(t, ij) = \langle \hat{v}_{av}(t) \cdot \hat{v}_p^{ij}(0) \rangle, \quad (6.9)$$

where  $\hat{v}_p^{ij}(0)$  denotes the average perturbed heading of individual  $i$  and  $j$ . The response of a school to perturbations in the headings of more than two members is defined in a similar manner.

Figure 6.6 shows for  $r = 64$ , the response of a school to spatially and temporally correlated perturbations of up to six members in the 2nd quartile. The form of response is quite similar: a rapid initial increase in correlation followed by a decay due to noise effects. The peak correlation  $C_{max}$  seems to saturate as the number of perturbed individuals increases. In addition, the time in which the heading cross-correlation function reaches its peak value  $C_{max}$  increases.

In general, for all four quartiles, we find that when individuals are located in the same quartile and perturbed at the same time (spatial-temporal), the peak correlation  $C_{max}$  saturates with the number of perturbed individuals; see Figure 6.7. In other words, the rate of response seems to decrease with the number of individuals perturbed. On the same figure, the peak correlation for temporally (and

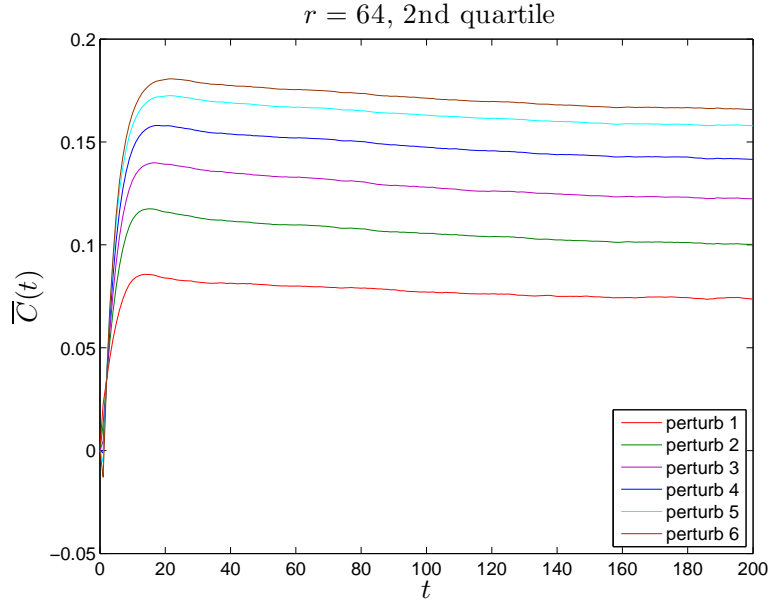


Figure 6.6: Cross-correlation functions measure the response of the school to spatially and temporally correlated perturbations in the headings of 1-6 members in the 2nd quartile of a school with  $r = 64$ .

not spatially) correlated perturbations is shown. Here, the peak correlation  $C_{max}$  increases almost linearly with the number of perturbed individuals. In addition, we find that the overall response of a school to multiple simultaneous perturbations is larger when individuals are not spatially correlated. This is most likely due to the fact that individuals that are not correlated in space can cover more of the social network and thus more effectively influence a greater number of individuals.

## 6.6 Conclusion

We considered a two-dimensional individual-based model for fish schooling which incorporates a tendency for each fish to align its position and orientation with an appropriate average of its neighbors' positions and orientations, plus a tendency for

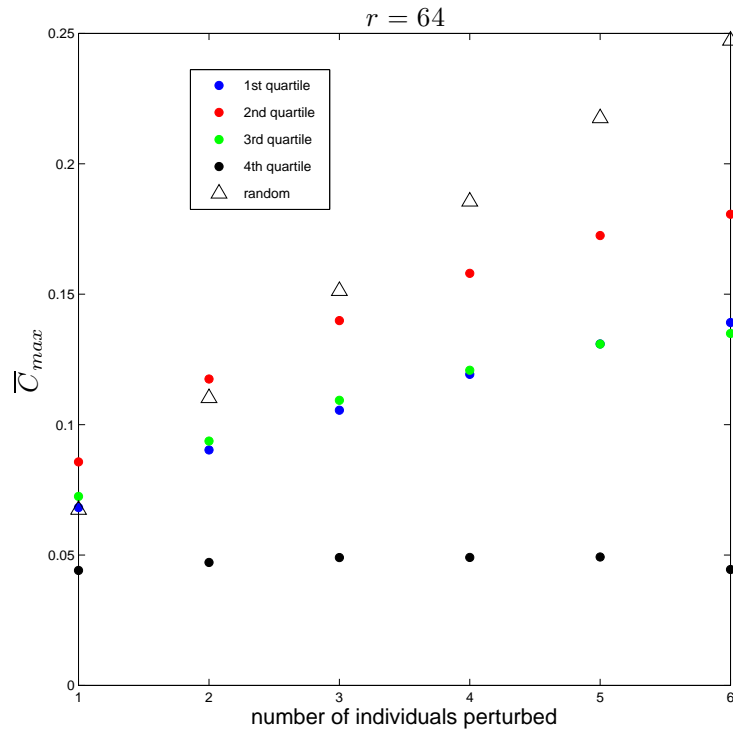


Figure 6.7: Peak response  $\overline{C}_{max}$  of a school to perturbations in the headings of multiple individuals. Here we consider a school's response to spatially and temporally correlated perturbations in each of the four quartiles (circles) and just temporally correlated perturbations (triangle) for  $r = 64$ .

each fish to avoid collisions. We explored the effects of different weights of orientation and attraction response on the schooling behavior. We find that as the ratio of orientation to attraction weights increases, schools become more highly polarized. We also note that when groups are highly elongated but not highly polarized, the probability of fragmentation increases.

We used a cross-correlation function to measure the response of a school to perturbations in the headings of individual members. We find that there are multiple time scales associated with information transfer and loss. In the fast time scale, information is transferred in approximately 2-4 seconds. As schools become more highly polarized, they respond more strongly to internal perturbations. Overall, we find that individuals in the 2nd quartile induce the greatest response. Thus, individuals located in front of the school are *not* necessarily in the best position in terms of control and leadership of the school. In the future, we hope to compare the results with data from laboratory experiments on schooling fish already underway.

# Appendix A

## Derivation of the Fokker-Planck Equation

In this section, we outline a derivation of the Fokker-Planck equation and equations for the drift and diffusion terms. To begin the derivation, we first make some assumptions regarding the properties of the stochastic process. Suppose  $\{X(t) : t \geq 0\}$  is a one-dimensional stochastic process with  $t_1 > t_2 > t_3$ . We use  $P(X_1, t_1; X_2, t_2)$  to denote the joint probability distribution, i.e., the probability that  $X(t_1) = X_1$  and  $X(t_2) = X_2$ , and  $P(X_1, t_1 | X_2, t_2)$  to denote the conditional (or transition) probability distribution, i.e., the probability that  $X(t_1) = X_1$  given that  $X(t_2) = X_2$ , defined as  $P(X_1, t_1; X_2, t_2) = P(X_1, t_1 | X_2, t_2)P(X_2, t_2)$ . We further assume  $X(t)$  is a *Markov* process, namely,

$$P(X_1, t_1 | X_2, t_2; X_3, t_3) = P(X_1, t_1 | X_2, t_2).$$

For any continuous state Markov process, the following Chapman-Kolmogorov equation is satisfied [30, 92]:

$$P(X_1, t_1 | X_3, t_3) = \int P(X_1, t_1 | X_2, t_2)P(X_2, t_2 | X_3, t_3)dX_2. \quad (\text{A.1})$$

Finally, we will also assume  $X(t)$  is *time homogeneous*:

$$P(X_1, t_1 + s; X_2, t_2 + s) = P(X_1, t_1; X_2, t_2),$$

so that  $X$  is invariant with respect to a shift in time. For simplicity of notation, we use  $P(X_1, t_1 - t_2 | X_2) \equiv P(X_1, t_1 | X_2, t_2)$ .

We may now derive the Fokker-Planck equation from the Chapman-Kolmogorov identity (A.1) as follows [13]. Consider

$$\int_{-\infty}^{\infty} h(Y) \frac{\partial P(Y, t | X)}{\partial t} dY,$$

where  $h(Y)$  is any smooth function with compact support. Writing

$$\frac{\partial P(Y, t | X)}{\partial t} = \lim_{\Delta t \rightarrow 0} \frac{P(Y, t + \Delta t | X) - P(Y, t | X)}{\Delta t},$$

and interchanging the limit with the integral, it follows that

$$\int_{-\infty}^{\infty} h(Y) \frac{\partial P(Y, t | X)}{\partial t} dY = \lim_{\Delta t \rightarrow 0} \int_{-\infty}^{\infty} h(Y) \left[ \frac{P(Y, t + \Delta t | X) - P(Y, t | X)}{\Delta t} \right] dY. \quad (\text{A.2})$$

Applying the Chapman-Kolmogorov identity (A.1), the right hand side of expression (A.2) can be written as

$$\lim_{\Delta t \rightarrow 0} \frac{1}{\Delta t} \left[ \int_{-\infty}^{\infty} h(Y) \int_{-\infty}^{\infty} P(Y, \Delta t | Z)P(Z, t | X)dZ dY - \int_{-\infty}^{\infty} h(Y)P(Y, t | X)dY \right]. \quad (\text{A.3})$$

Interchanging the limits of integration in the first term of (A.3), letting  $Y \rightarrow Z$  in the second term, and using the identity  $\int_{-\infty}^{\infty} P(Y, \Delta t | Z) dY = 1$ , we have

$$\lim_{\Delta t \rightarrow 0} \frac{1}{\Delta t} \left[ \int_{-\infty}^{\infty} P(Z, t | X) \int_{-\infty}^{\infty} P(Y, \Delta t | Z) (h(Y) - h(Z)) dY dZ \right].$$

Taylor expanding  $h(Y)$  about  $Z$  gives

$$\lim_{\Delta t \rightarrow 0} \frac{1}{\Delta t} \left[ \int_{-\infty}^{\infty} P(Z, t | X) \int_{-\infty}^{\infty} P(Y, \Delta t | Z) \sum_{n=1}^{\infty} h^{(n)}(Z) \frac{(Y - Z)^n}{n!} dY dZ \right].$$

Defining the jump moments as

$$D^{(n)}(Z) = \frac{1}{n!} \lim_{\Delta t \rightarrow 0} \frac{1}{\Delta t} \int_{-\infty}^{\infty} (Y - Z)^n P(Y, \Delta t | Z) dY, \quad (\text{A.4})$$

it follows that

$$\int_{-\infty}^{\infty} h(Y) \frac{\partial P(Y, t | X)}{\partial t} dY = \int_{-\infty}^{\infty} P(Z, t | X) \sum_{n=1}^{\infty} D^{(n)}(Z) h^{(n)}(Z) dZ. \quad (\text{A.5})$$

Integrating each term on the right hand side of (A.5) by parts  $n$  times and using the assumptions on  $h$ , after moving terms to the left hand side, it follows that

$$\int_{-\infty}^{\infty} h(Z) \left( \frac{\partial P(Z, t | X)}{\partial t} - \sum_{n=1}^{\infty} \left( -\frac{\partial}{\partial Z} \right)^n [D^{(n)}(Z) P(Z, t | X)] \right) dZ = 0.$$

Now, since  $h$  is an arbitrary function, it is necessary that

$$\frac{\partial P(Z, t | X)}{\partial t} = \sum_{n=1}^{\infty} \left( -\frac{\partial}{\partial Z} \right)^n [D^{(n)}(Z) P(Z, t | X)]. \quad (\text{A.6})$$

We define the probability distribution function  $P(X, t)$  of  $X(t)$  as the solution of equation (A.6) with initial condition given by a  $\delta$ -distribution at  $X_0$  at  $t = 0$ . In this case,  $P(X, t) \equiv P(X, t | X_0, 0)$  and we may write equation (A.6) as

$$\frac{\partial P(X, t)}{\partial t} = \sum_{n=1}^{\infty} \left( -\frac{\partial}{\partial X} \right)^n [D^{(n)}(X) P(X, t)], \quad (\text{A.7})$$

and equation (A.4) as

$$D^{(n)}(X_0) = \frac{1}{n!} \lim_{\Delta t \rightarrow 0} \frac{1}{\Delta t} \langle [X(t + \Delta t) - X(t)]^n \rangle |_{t=0}. \quad (\text{A.8})$$

Equation (A.7) is referred to as the Kramers-Moyal expansion. The Fokker-Planck equation is a special case of the Kramers-Moyal expansion (A.7) for which  $D^{(n)}(X) = 0$  for  $n > 2$ . Such a condition holds when the stochastic process  $X(t)$  has continuous sample paths and is satisfied, for example, when  $X$  obeys a stochastic differential equation with Gaussian white noise.

It easily follows from (A.8) that for  $n = 1$ , the drift term may be written as

$$D^{(1)}(X_0) = \left. \frac{\partial \langle X(t; X_0) \rangle}{\partial t} \right|_{t=0}, \quad (\text{A.9})$$

where  $X(t; X_0)$  denotes a trajectory initialized at  $X_0$  at  $t = 0$  and angular brackets denote ensemble averaging over different realizations of the trajectory. We now show how the diffusion term  $D^{(2)}(X)$  can be written as

$$D^{(2)}(X_0) = \left. \frac{1}{2} \frac{\partial \text{Var}(t; X_0)}{\partial t} \right|_{t=0}, \quad (\text{A.10})$$

where  $\text{Var}(t; X_0)$  denotes the variance of an ensemble of trajectories initialized at  $X_0$  at  $t = 0$ . Letting  $n = 2$  in (A.8) we have

$$\begin{aligned} D(X_0) &= \frac{1}{2} \lim_{\Delta t \rightarrow 0} \frac{1}{\Delta t} \langle [X(\Delta t) - X(0)]^2 \rangle \\ &= \frac{1}{2} \lim_{\Delta t \rightarrow 0} \frac{\langle X(\Delta t)^2 \rangle - 2X(0)\langle X(\Delta t) \rangle + X(0)^2}{\Delta t}. \end{aligned}$$

Expanding  $\langle X(t) \rangle$  about  $t = 0$ , we may write  $\langle X(\Delta t) \rangle = X(0) + C_1 \Delta t + C_2 \Delta t^2 + \dots$

so that

$$\begin{aligned}
D(X_0) &= \frac{1}{2} \lim_{\Delta t \rightarrow 0} \frac{\langle X(\Delta t)^2 \rangle - 2X(0)[X(0) + C_1\Delta t + C_2\Delta t^2 + \dots] + X(0)^2}{\Delta t} \\
&= \frac{1}{2} \lim_{\Delta t \rightarrow 0} \frac{\langle X(\Delta t)^2 \rangle - X(0)^2 - 2X(0)[C_1\Delta t + C_2\Delta t^2 + \dots]}{\Delta t} \\
&= \frac{1}{2} \lim_{\Delta t \rightarrow 0} \frac{\langle X(\Delta t)^2 \rangle - X(0)^2 - 2X(0)C_1\Delta t + O(\Delta t^2)}{\Delta t}.
\end{aligned}$$

Expression (A.10) can be written as

$$\begin{aligned}
D(X_0) &= \frac{1}{2} \lim_{\Delta t \rightarrow 0} \frac{\langle [X(\Delta t) - \langle X(\Delta t) \rangle]^2 \rangle}{\Delta t} \\
&= \frac{1}{2} \lim_{\Delta t \rightarrow 0} \frac{\langle X(\Delta t)^2 \rangle - \langle X(\Delta t) \rangle^2}{\Delta t} \\
&= \frac{1}{2} \lim_{\Delta t \rightarrow 0} \frac{\langle X(\Delta t)^2 \rangle - (X(0) + C_1\Delta t + C_2\Delta t^2 + \dots)^2}{\Delta t} \\
&= \frac{1}{2} \lim_{\Delta t \rightarrow 0} \frac{\langle X(\Delta t)^2 \rangle - X(0)^2 - 2X(0)C_1\Delta t + O(\Delta t^2)}{\Delta t}.
\end{aligned}$$

Therefore, expressions (A.10) and (A.8) with  $n = 2$  are equivalent in the limit  $\Delta t \rightarrow 0$ .

# Appendix B

## Derivation of Mean Residence

### Times and Kramers Formula

Using the backward Fokker-Planck equation, one may derive expressions for the mean escape time from each well of a bistable potential. Suppose  $X(t)$  has value  $X$  at time  $t = 0$  where  $X \in (a, b)$ . Then, the probability that  $X(t)$  is in  $(a, b)$  at time  $t$  is given by

$$F(t; X) = \int_a^b P(X', t|X, 0)dX'. \quad (\text{B.1})$$

If  $T$  is the time  $X(t)$  first leaves the interval  $(a, b)$ , then  $F(t; X) = \text{Prob}(T \geq t)$ ; this holds for reflecting or absorbing boundary conditions at  $a$  and  $b$ , as will be used below. For a stationary process, the backward FP equation may be written as [30]

$$\frac{\partial}{\partial t}P(X', t|X, 0) = D^{(1)}(X)\frac{\partial}{\partial X}P(X', t|X, 0) + D^{(2)}(X)\frac{\partial^2}{\partial X^2}P(X', t|X, 0), \quad (\text{B.2})$$

with boundary conditions  $P(X', 0|X, 0) = \delta(X - X')$ . It then follows that  $F$  satisfies the equation

$$\frac{\partial}{\partial t} F(t; X) = D^{(1)}(X) \frac{\partial}{\partial X} F(t; X) + D^{(2)}(X) \frac{\partial^2}{\partial X^2} F(t; X), \quad (\text{B.3})$$

with boundary conditions

$$F(0; X) = \begin{cases} 1 & : a \leq X \leq b \\ 0 & : \text{elsewhere.} \end{cases}$$

The cumulative distribution function of the random variable  $T$  is given by  $\text{Prob}(T < t) = 1 - \text{Prob}(T \geq t) = 1 - F(t; X)$ . Thus, the probability density function of  $T$  is given by  $-\frac{dF}{dt}$  and the mean first passage time  $\langle T \rangle$  is given by

$$\langle T \rangle = - \int_0^\infty t dF(t; X) = - \int_0^\infty t \partial_t F(t; X) dt. \quad (\text{B.4})$$

After integrating equation (B.4) by parts, it follows that

$$T(X) \equiv \langle T \rangle = \int_0^\infty F(t; X) dt. \quad (\text{B.5})$$

Finally, after integrating equation (B.3) over the interval  $(0, \infty)$  one finds that  $T(X)$  satisfies the following differential equation:

$$\frac{dT}{dX} D^{(1)}(X) + \frac{d^2 T}{dX^2} D^{(2)}(X) = -1. \quad (\text{B.6})$$

Now, suppose the left well is located at  $X_1$  with barrier at  $X^*$ . Then, to find the mean time spent in the left well, we must solve equation (B.6) for  $T$  where  $a = -\infty$  is a reflecting boundary and  $b = X^*$  is an absorbing boundary. This means that  $\partial_X F(t; -\infty) = 0$  and  $F(t; X^*) = 0$  which gives the following conditions on  $T$ ,

$$T'(-\infty) = 0, \quad T(X^*) = 0. \quad (\text{B.7})$$

Solving equation (B.6) with conditions (B.7) gives the following equation for the mean time spent in the left well:

$$T(X_1 \rightarrow X^*) = \int_{X_1}^{X^*} dY e^{G(Y)} \int_{-\infty}^Y dZ \frac{e^{-G(Z)}}{D^{(2)}(Z)}, \quad (\text{B.8})$$

where

$$G(X) = - \int_{-\infty}^X dX' \frac{D^{(1)}(X')}{D^{(2)}(X')}. \quad (\text{B.9})$$

$G$  is related to the effective potential in equation (2.10) as  $U(X) = \log(D^{(2)}(X)) + G(X) + \text{const.}$  A similar expression for the mean time spent in the right well, located at  $X_2$ , is given by

$$T(X_2 \rightarrow X^*) = \int_{X^*}^{X_2} dY e^{G(Y)} \int_Y^{\infty} dZ \frac{e^{-G(Z)}}{D^{(2)}(Z)}. \quad (\text{B.10})$$

We may estimate the mean residence time  $T(X_1 \rightarrow X^*)$  for constant  $D^{(2)}(X) = D$  as follows. First, since  $G(X) = U(X) + \text{const.}$ , we rewrite expression (B.8) as

$$T(X_1 \rightarrow X^*) = \frac{1}{D} \int_{X_1}^{X^*} dY e^{U(Y)} \int_{-\infty}^Y dZ e^{-U(Z)}, \quad (\text{B.11})$$

where

$$U(X) = -\frac{1}{D} \int_{-\infty}^X dX' D^{(1)}(X') + \text{const.} = U_0(X)/D + \text{const.} \quad (\text{B.12})$$

Now, if  $\Delta U_0 = U_0(X^*) - U_0(X_1)$  is much larger than  $D$ , then we may approximate (B.11) as

$$T(X_1 \rightarrow X^*) = \frac{1}{D} \left\{ \int_{-\infty}^{X^*} dZ e^{-U(Z)} \right\} \int_{X_1}^{X^*} dY e^{U(Y)}, \quad (\text{B.13})$$

where the inner integral in (B.11) has been replaced by the expression in brackets.

We can further estimate the mean residence time by Taylor expanding  $U(X)$  near

$X_1$  as

$$U(X) \simeq U(X_1) + \frac{U''(X_1)}{2}(X - X_1)^2, \quad (\text{B.14})$$

and near  $X^*$  as

$$U(X) \simeq U(X^*) - \frac{|U''(X^*)|}{2}(X - X^*)^2. \quad (\text{B.15})$$

Then, we may approximate the first integral as

$$\int_{-\infty}^{X^*} dZ e^{-U(Z)} \approx \int_{-\infty}^{\infty} dZ \exp \left\{ -U(X_1) - \frac{U''(X_1)}{2}(Z - X_1)^2 \right\} \quad (\text{B.16})$$

$$= \frac{\sqrt{2\pi}}{\sqrt{U''(X_1)}} e^{-U(X_1)}, \quad (\text{B.17})$$

and the second integral as

$$\int_{X_1}^{X^*} dY e^{U(Y)} \approx \int_{-\infty}^{\infty} dY \exp \left\{ U(X^*) - \frac{|U''(X^*)|}{2}(Y - X^*)^2 \right\} \quad (\text{B.18})$$

$$= \frac{\sqrt{2\pi}}{\sqrt{|U''(X^*)|}} e^{U(X^*)}. \quad (\text{B.19})$$

It follows from (B.17) and (B.19) that the mean residence time  $T(X_1 \rightarrow X^*)$  may be approximated as

$$T(X_1 \rightarrow X^*) \approx \frac{2\pi e^{\Delta U}}{D \sqrt{U''(X_1) |U''(X^*)|}}, \quad (\text{B.20})$$

where  $\Delta U = U(X^*) - U(X_1)$ . Expression (B.20) is commonly known as Kramer's formula and is a classical formula of reaction rate theory in chemistry. A similar expression holds for  $T(X_2 \rightarrow X^*)$ . If  $D^{(2)}(X)$  is not constant, we can use the approximation  $D^{(2)}(X) \approx \bar{D} = \frac{1}{2}(D^{(2)}(X^*) + D^{(2)}(X_1))$  in  $[X_1, X^*]$  to replace  $D$  in formula (B.20).

# Appendix C

## Diffusion Maps and Principal Component Analysis

The diffusion map approach can be thought of as a nonlinear extension of principal component analysis (PCA) [48, 94]. In PCA, analysis of a dataset is based on the assumption of linearity. A sample dataset is re-expressed through a linear transformation in terms of a new orthogonal basis which optimally captures the variance in the dataset. The first few modes give a low-dimensional representation of the dataset. However, due to this linearity assumption, PCA may not always find an optimal (in terms of low-dimensionality) representation of the dataset. For example, consider as in Figure C.1, two Gaussian clouds in the plane drawn from normal distributions centered at  $(-1, 0)$  and  $(1, 0)$  with standard deviation  $\sigma_c = 0.4$  in both cases. For this dataset, PCA finds the optimal basis to be  $e_1 = [1, 0]$  and  $e_2 = [0, 1]$ . In Figure C.2, the projection of the dataset onto the first basis vec-

tor is plotted, which in this example is equivalent to plotting the  $x$ -coordinates of the datapoints. As one can see from the left panel of the figure, the first modal coordinates do not give a sharp parametrization of the dataset which distinguishes between the two cloud clusters.

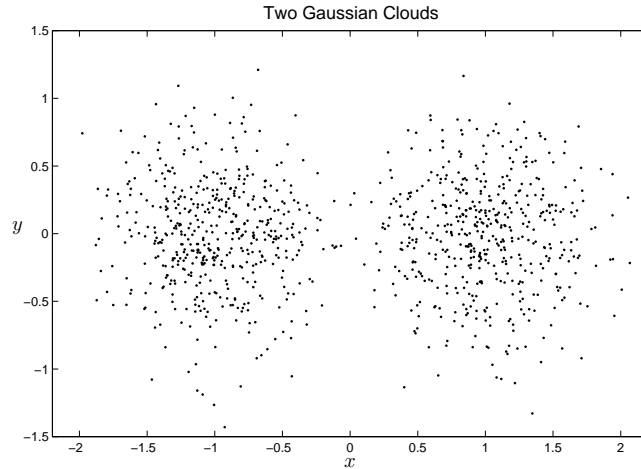


Figure C.1: Dataset sampled from two normal distributions centered at  $(-1, 0)$  and  $(1, 0)$  with standard deviation  $\sigma_c = 0.4$  in each case.

In contrast, using the diffusion map approach, with Gaussian kernel of a sufficiently small variance  $\sigma^2$ , we can capture the bimodal structure of the dataset with a single coordinate. In the right panel of Figure C.2, the sorted components of the first non-trivial eigenvector obtained from the diffusion map procedure with  $\sigma = 0.4$  and  $\sigma = 1.2$  are plotted. The parameter  $\sigma$  controls the connection strength of the graph of the dataset. As one can see from the figure, for  $\sigma = 1.2$  the parametrization of the dataset looks similar to that of PCA, while for  $\sigma = 0.4$ , the first non-trivial eigenvector is approximately constant in each cloud with a sharp

transition between them. This is due to the fact that for  $\sigma$  sufficiently small, the two clouds are effectively disconnected in the graph of the dataset and are therefore quite far away in diffusion distance. Thus, if  $\sigma^2$  is chosen to be of the same order as the variance  $\sigma_c^2$  of the dataset, the diffusion map approach is able to capture the bimodal structure with a single coordinate.

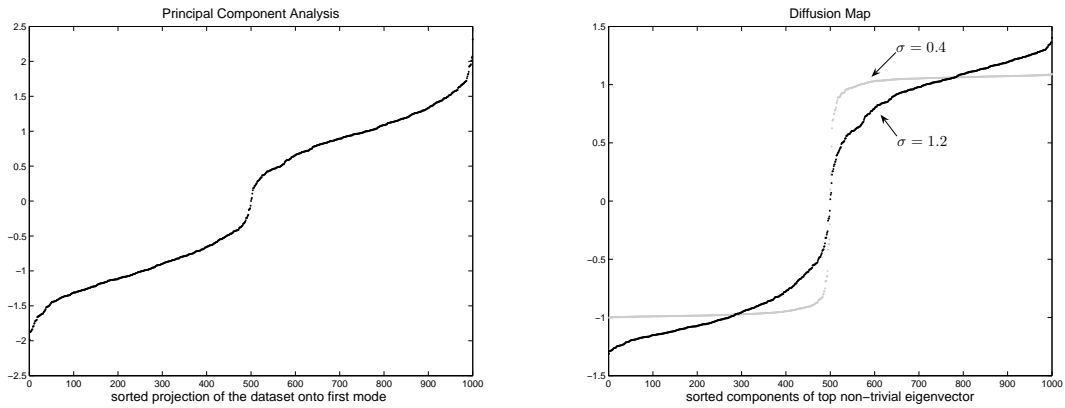


Figure C.2: Left panel: The sorted projection of the Gaussian cloud dataset onto the first mode obtained using Principal Component Analysis. Right panel: The sorted components of the first non-trivial eigenvector obtained from the diffusion map procedure with  $\sigma = 0.4$  (gray) and  $\sigma = 1.2$  (black).

# Appendix D

## Parallel Simulation on a GPU

A Graphics Processing Unit (GPU) is an inexpensive yet powerful alternative to a cluster for parallel simulations. Its architecture is very well suited to simulations of the individual-based schooling model. Parallel computation on general-purpose GPUs (GPGPU) has become an active research area with a wide range of scientific applications including fluid dynamics, cellular automata, particle systems, and neural networks [34, 39, 80]. Previous generation GPUs have required computations to be recast into a graphics applications programming interface such as OpenGL, which has made programming GPUs for non-graphics applications a significant challenge. In 2007, NVIDIA [75] released a Compute Unified Device Architecture (CUDA), a new hardware and software architecture for issuing and managing data-parallel computations on the GPU [74]. The CUDA API is an extension of the C programming language, which results in a minimal learning curve for beginners to access the low-level hardware.

To perform parallel simulations of the two-dimensional schooling model described in Chapter 6, we used a CUDA-enabled NVIDIA GeForce 8800GTX chip with 768 MB RAM installed on a host workstation with Intel Pentium 3.00 GHz CPU and 3.50GB of RAM with physical address extension. The chip has 128 stream processors, divided into 16 clusters of multiprocessors with eight streaming processors per multiprocessor. The eight processors in each multiprocessor share 16K shared memory, bringing data closer to the arithmetic logic unit (ALU). The global memory adjacent to the GPU chip is much larger, but has a much higher latency than the on-chip shared memory. It takes about 400-600 clock cycles to read or write to the global memory vs. 4 clock cycles to access the shared memory. The GPU is still a specialized device. It can only support single-precision operations and is only very efficient for applications with high computation per memory access and single instruction multiple data computation [103]. To efficiently make use of the GPU's computational resources, one must maximize the number of threads running in parallel, while keeping the limited shared memory size into account. By a thread, we mean an executable task on a set of data. Although it is not difficult to migrate code to a GPU, a careful study and implementation is necessary for good performance.

We programmed the GPU to perform multiple steady-state simulations of the schooling model, parallelizing within a single realization and across multiple realizations. To effectively use the GPU, we make as much use of the on-chip shared memory as possible. For parallelization within a realization, there is a limit to

the number of fish that can be stored in shared memory. We thus perform behavioral influence computations in parallel for  $n$  fish at a time, where the school is divided into  $m$  groups of  $n$  individuals. In addition to parallel processing within a single realization, multiple independent replicate simulations are performed in parallel. Whenever a thread is waiting to access the device memory (e.g., to load the current position and heading of agent  $i$ ), another thread is running on the ALUs (e.g., to compute the desired heading of agent  $j$ ). Thus, memory access latency is not a problem. To generate random numbers, which are needed to generate initial conditions and to add noise to our calculations at each step, we employed a modified version of Eric Mills' multi-threaded C implementation of the Mersenne Twister (MT) algorithm [76]. For more details on the parallel implementation of the schooling model, see [61].

We observed speedups of 230-240 times for our parallelized code running on the GPU over the corresponding sequential simulation on the host workstation. It takes only a few minutes to perform 1000 steady-state simulations (lasting 3000 steps) of the model for schools of size  $N = 100$  over a mesh of 25 different values of the parameter  $r$ . The corresponding serial simulation on the CPU takes almost an entire day to complete.

# Bibliography

- [1] Y. Aït-Sahalia. Maximum-likelihood estimation of discretely-sampled diffusions: A closed-form approximation approach. *Econometrica*, 70:223–262, 2002.
- [2] M. Andersson and J. Wallander. Kin selection and reciprocity in flight formation? *Behav. Ecol.*, 15:158–162, 2003.
- [3] I. Aoki. A simulation study on the schooling mechanism in fish. *Bull. Jap. Soc. Fish.*, 48:1081–1088, 1982.
- [4] P. Ashwin and J. Swift. The dynamics of  $N$  weakly coupled identical oscillators. *J. Nonlin. Sci.*, 2:69–108, 1992.
- [5] C. Baker. *The Numerical Treatment of Integral Equations*. Clarendon Press, Oxford, 1977.
- [6] M. Belkin and P. Niyogi. Laplacian eigenmaps for dimensionality reduction and data representation. *Neural Comput.*, 15:1373–1396, 2003.

- [7] E. Bonabeau. Agent-based modeling: Methods and techniques for simulating human systems. *PNAS*, 99:7280–7287, 2002.
- [8] E. Bonabeau, G. Theraulaz, J-L. Deneubourg, S. Aron, and S. Camazine. Self-organization in social insects. *TREE*, 12(5), 1997.
- [9] E. Brown, P. Holmes, and J. Moehlis. Globally coupled oscillator networks. In E. Kaplan, J. Marsden, and K.R. Sreenivasan, editors, *Perspectives and Problems in Nonlinear Science: A Celebratory Volume in Honor of Larry Sirovich*, pages 183–215. Springer-Verlag, New York, 2003.
- [10] J. Buhl, D. J. T. Sumpter, I. D. Couzin, J. J. Hale, E. Despland, E. R. Miller, and S. J. Simpson. From disorder to order in marching locusts. *Nature*, 312:1402–1406, 2006.
- [11] S. Camazine, J. L. Deneubourg, N. R. Franks, J. Sneyd, G. Theraulaz, and E. Bonabeau. *Self-Organization in Biological Systems*. Princeton University Press, Princeton, 2003.
- [12] L. Chaimowicz, V. Kumar, and F. M. Campos. A paradigm for dynamic coordination of multiple robots. *Autonomous Robots*, 17(1):7–21, 2004.
- [13] W. T. Coffey, Yu. P. Kalmykov, and J. T. Waldron. *The Langevin Equation: With Applications to Stochastic Problems in Physics, Chemistry, and Electrical Engineering*. World Scientific, Singapore, 2004.

- [14] R. R. Coifman and S. Lafon. Diffusion maps. *Appl. Comput. Harmon. Anal.*, 21:5–30, 2006.
- [15] J. Cortès, S. Martìnes, T. Karatas, and F. Bullo. Coverage control for mobile sensing networks. *IEEE Trans. on Robotics and Automation*, 20(2):243–255, 2004.
- [16] J. C. Coulson. Differences in the quality of birds nesting in the centre and on the edges of a colony. *Nature*, 217:478–479, 1968.
- [17] I. Couzin. Collective minds. *Nature*, 445, 2007.
- [18] I. D. Couzin, J. Krause, N. R. Franks, and S. A. Levin. Effective leadership and decision making in animal groups on the move. *Nature*, 433:513–516, 2005.
- [19] I. D. Couzin, J. Krause, R. James, G. D. Ruxton, and N. R. Franks. Collective memory and spatial sorting in animal groups. *J. theor. Biol.*, 218:1–11, 2002.
- [20] A. Czirók and T. Vicsek. Collective motion. In T. Vicsek, editor, *Fluctuations and Scaling in Biology*, pages 177–242. Oxford University Press, Oxford, 2001.
- [21] J-L. Deneubourg and S. Goss. Collective patterns and decision making. *Ethol. Ecol. Evol.*, 1:295–311, 1989.
- [22] J. P. Desai, J. P. Ostrowski, and V. Kumar. Modeling and control of formations of nonholonomic mobile robots. *IEEE Trans. Robot. Automat.*, 17:905–908, 2001.

- [23] P. M. Driver and D. A. Humphries. *Protean Behavior: The Biology of Unpredictability*. Oxford University Press, Oxford, 1988.
- [24] L. Edelstein-Keshet, J. Watmough, and D. Grünbaum. Do travelling band solutions describe cohesive swarms? An investigation for migratory locusts. *J. Math. Bio.*, 36:515–549, 1998.
- [25] R. Eftimie, G. de Vries, and M. A. Lewis. Complex spatial group patterns result from different animal communication mechanisms. *Proc. Natl. Acad. Sci. USA*, 104(17):6974–6979, 2007.
- [26] J. A. Endler. Some general comments on the evolution and design of animal communication systems. *Philos. Trans. R. Soc. London Ser. B*, 340:215–225, 1993.
- [27] R. Erban, T. A. Frewen, X. Wang, T. C. Elston, R. Coifman, B. Nadler, and I. G. Kevrekidis. Variable-free exploration of stochastic models: a gene regulatory network example. *J. Chem. Phys.*, 126:155103, 2007.
- [28] U. Erdmann, W. Ebeling, and A. S. Mikhailov. Noise-induced transition from translational to rotational motion of swarms. *Phys. Rev. E*, 71:051904, 2005.
- [29] D. B. Forger and D. Paydarfar. Starting, stopping, and resetting biological oscillators: in search of optimal perturbations. *J. theor. Biol.*, 230:521–532, 2004.

- [30] C.W. Gardiner. *Handbook of Stochastic Methods*. Springer-Verlag, Berlin, 2004.
- [31] V. Gazi and K. M. Passino. Stability analysis of swarms. *IEEE Trans. Automatic Control*, 48:692–696, 2002.
- [32] C. W. Gear, T. J. Kaper, I. G. Kevrekidis, and A. Zagaris. Projecting to a slow manifold: Singularly perturbed systems and legacy codes. *SIAM J. Applied Dynamical Systems*, 4:711–732, 2005.
- [33] H. Goldstein. *Classical Mechanics*. Addison-Wesley, Reading, MA, 1980.
- [34] GPGPU-Home. GPGPU homepage, 2007. <http://www.gpgpu.org/>.
- [35] G. Grégoire, H. Chaté, and Y. Tu. Moving and staying together without a leader. *Physica D*, 181:157–170, 2003.
- [36] V. Grimm and S. F. Railsback. *Individual-based Modeling and Ecology*. Princeton University Press, Princeton, 2005.
- [37] D. Grünbaum. Schooling as a strategy for taxis in a noisy environment. *Evolutionary Ecology*, 12:503–522, 1998.
- [38] J. Guckenheimer and P. Holmes. *Nonlinear Oscillations, Dynamical Systems, and Bifurcations of Vector Fields*. Springer-Verlag, New York, 1983.
- [39] H. Li and L. Petzold. Stochastic simulation of biochemical systems on the graphics processing unit. Technical report, Department of Computer Science, University of California, Santa Barbara, 2007. Submitted.

- [40] M. Haataja, D. J. Srolovitz, and I. G. Kevrekidis. Apparent hysteresis in a driven system with self-organized drag. *Phys. Rev. Lett.*, 92:160603, 2004.
- [41] P. Hänggi, P. Talkner, and M. Borkovec. Reaction-rate theory: fifty years after Kramers. *Reviews of Modern Physics*, 62:251–342, 1990.
- [42] D. J. Higham. An algorithmic introduction to numerical simulation of stochastic differential equations. *SIAM Review*, 43:525–546, 2001.
- [43] C. Huepe and M. Aldana. Intermittency and clustering in a system of self-driven particles. *Phys. Rev. Lett.*, 92:168701, 2004.
- [44] G. Hummer and I. G. Kevrekidis. Coarse molecular dynamics of a peptide fragment: Free energy, kinetics, and long-time dynamics computations. *J. Chem. Phys.*, 118:10762–10773, 2003.
- [45] A. Huth and C. Wissel. The simulation of fish schools in comparison with experimental data. *Ecological Modelling*, 75:135–145, 1994.
- [46] Y. Inada and K. Kawachi. Order and flexibility in the motion of fish schools. *J. theor. Biol.*, 214:371–387, 2002.
- [47] A. Jadbabaie, J. Lin, and A. S. Morse. Coordination of groups of mobile autonomous agents using nearest neighbor rules. *IEEE Trans. Automatic Control*, 48:692–696, 2003.
- [48] I. T. Jolliffe. *Principal Component Analysis*. Springer-Verlag, New York, 1986.

- [49] E. Justh and P. Krishnaprasad. Equilibria and steering laws for planar formations. *Systems and Control Letters*, 52(1):25–38, 2004.
- [50] E. F. Keller and L. A. Segel. Initiation of slime mold aggregation viewed as an instability. *J. Theor. Bio.*, 26(3):399–415, 1970.
- [51] I. G. Kevrekidis, C. W. Gear, J. M. Hyman, P. G. Kevrekidis, O. Runborg, and T. Theodoropoulos. Equation free, coarse-grained multiscale computation: enabling microscopic simulators to perform system-level analysis. *Comm. Math. Sci.*, 1:715–762, 2003.
- [52] M. Kimura and J. Moehlis. Novel vehicular trajectories for collective motion from coupled oscillator steering control. Submitted.
- [53] P. E. Kloeden and E. Platen. *Numerical solution of stochastic differential equations*. Springer-Verlag, Berlin, 1992.
- [54] D. I. Kopelevich, A. Z. Panagiotopoulos, and I. G. Kevrekidis. Coarse-grained kinetic computations for rare events: Application to micelle formation. *J. Chem. Phys.*, 122:044908, 2005.
- [55] J. Krause. The relationship between foraging and shoal position in a mixed shoal of roach (*rutilus rutilus*) and chub (*leuciscus cephalus*): a field study. *Oecologia*, 93:356–359, 1993.
- [56] J. Krause. Differential fitness returns in relation to spatial position in animal groups. *Biol. Rev.*, 69:187–206, 1994.

- [57] J. Krause and G. D. Ruxton. *Living in Groups*. Oxford University Press, Oxford, 2002.
- [58] S. Lafon and R. R. Coifman. Geometric harmonics: A novel tool for multi-scale out-of-sample extension of empirical functions. *Appl. Comput. Harmon. Anal.*, 21:31, 2006.
- [59] C. R. Laing, T. A. Frewen, and I. G. Kevrekidis. Coarse-grained dynamics of an activity bump in a neural field model. *Nonlinearity*, 20(9):2127–2146, 2007.
- [60] N. Leonard and E. Fiorelli. Virtual leaders, artificial potentials and coordinated control of groups. In *Proceedings of the 40th IEEE Conf. Decision and Control*, pages 2968–2973. 2001.
- [61] H. Li, A. Kolpas, J. Moehlis, and L. Petzold. Parallel simulation for a fish schooling model on a general-purpose graphics processing unit. *Concurrency and Computation: Practice and Experience*, 2008. to appear.
- [62] P. B. S. Lissaman and C. A. Shollenberger. Formation flight of birds. *Science*, 168:1003–1005, 1970.
- [63] P. Marler. Animal communication signals. *Science*, 157:769–774, 1967.
- [64] D. R. Martinez and E. Klinghammer. The behavior of the whale *orcinus orca*: a review of the literature. *Z. Tierpsychol.*, 27:828–839, 1970.

- [65] R. M. May. Flight formations in geese and other birds. *Nature*, 282:778–780, 1979.
- [66] C. D. Meyer. *Matrix Analysis and Applied Linear Algebra*. SIAM, Philadelphia, PA, 2000.
- [67] J. Moehlis, E. Shea-Brown, and H. Rabitz. Optimal inputs for phase models of spiking neurons. *ASME J. Comp. Nonlin. Dyn.*, 1:358–357, 2006.
- [68] A. Mogilner and L. Edelstein-Keshet. A non-local model for a swarm. *J. Math. Bio.*, 38:534–570, 1999.
- [69] A. Mogilner, L. Edelstein-Keshet, L. Bent, and A. Spiros. Mutual interactions, potentials, and individual distance in a social aggregation. *J. Math. Bio.*, 47:353–389, 2003.
- [70] S. J. Moon, R. Ghanem, and I. G. Kevrekidis. Coarse graining the dynamics of coupled oscillators. *Phys. Rev. Lett.*, 96:144101, 2006.
- [71] B. Nadler, S. Lafon, R. R. Coifman, and I. G. Kevrekidis. Diffusion maps, spectral clustering and eigenfunctions of Fokker-Planck operators. In Y. Weiss et. al., editor, *Advances in Neural Information Processing Systems*, volume 18, pages 955–962. MIT Press, Cambridge, MA, 2005.
- [72] B. Nadler, S. Lafon, R. R. Coifman, and I. G. Kevrekidis. Diffusion maps, spectral clustering and reaction coordinates of dynamical systems. *Appl. Comput. Harmon. Anal.*, 21:113–127, 2006.

- [73] S. R. S. J. Neill and J. M. Cullen. Experiments on whether schooling by their prey affects the hunting behavior of cephalopods and fish predators. *J. Zoology*, 172:549–569, 1974.
- [74] NVIDIA Corporation. NVIDIA CUDA Compute Unified Device Architecture Programming Guide, 2007. <http://developer.download.nvidia.com>.
- [75] NVIDIA Corporation. NVIDIA homepage, 2007. <http://www.nvidia.com>.
- [76] NVIDIA Forums members. NVIDIA forums, 2007. <http://forums.nvidia.com>.
- [77] A. Okubo and S. A. Levin. *Diffusion and Ecological Problems: Mathematical Models*. Lecture Notes in Biomathematics. Springer-Verlag, 2001.
- [78] R. Olfati-Saber. Flocking for multi-agent dynamic systems: algorithms and theory. *IEEE Trans. Automatic Control*, 51:401–420, 2006.
- [79] O. J. O’Loan and M. R. Evans. Alternating steady state in one-dimensional flocking. *J. Phys. A*, 32:L99–105, 1999.
- [80] J. D. Owens, D. Luebke, N. Govindaraju, M. Harris, J. Krger, A. E. Lefohn, and T. J. Purcell. A survey of general-purpose computation on graphics hardware. In *Eurographics 2005, State of the Art Reports*, pages 21–51, August 2005.
- [81] D. Paley, N. Leonard, and R. Sepulchre. Collective motion: Bistability and trajectory tracking. In *Proceedings of the 43rd IEEE Conf. Decision and Control*, pages 1932–1937. 2004.

- [82] D. A. Paley, N. E. Leonard, R. Sepulchre, D. Gröbbaum, and J. K. Parrish. Oscillator models and collective motion. *IEEE Control Systems Magazine*, pages 89–105, 2007.
- [83] J. K. Parrish and L. Edelstein-Keshet. Complexity, pattern, and evolutionary trade-offs in animal aggregation. *Science*, 284:99–101, 1999.
- [84] J. K. Parrish, S. V. Viscido, and D. Grünbaum. Self-organized fish schools: an examination of emergent properties. *Biol. Bull.*, 202:296–305, 2002.
- [85] B. L. Partridge. The structure and function of fish schools. *Sci. Am.*, 246:90–99, 1982.
- [86] B. L. Partridge and T. J. Pitcher. The sensory basis of fish schools: Relative roles of lateral line and vision. *J. Comp. Physiol.*, 135:315–325, 1980.
- [87] T. J. Pitcher, B. L. Partridge, and C. S. Wardle. A blind fish can school. *Science*, 194:963–965, 1976.
- [88] J. R. Raymond and M. R. Evans. Flocking regimes in a simple lattice model. *Phys. Rev. E*, 73:036112, 2006.
- [89] H. Reuter and B. Breckling. Self-organization of fish schools: an object-oriented model. *Ecol. Model.*, 75:147–159, 1994.
- [90] C. Reynolds. <http://www.red3d.com/cwr/boids>. 2004.
- [91] C. W. Reynolds. Flocks, herds and schools: a distributed behavioral model. *Comput. Graph.*, 21:25–34, 1987.

- [92] H. Risken. *The Fokker-Planck equation: Methods of Solution and Applications*. Springer-Verlag, Berlin, 1996.
- [93] W. L. Romey. Individual differences make a difference in the trajectories of simulated schools. *Ecol. Model.*, 92:65–77, 1996.
- [94] B. Schölkopf, A. Smola, and K. R. Müller. Nonlinear component analysis as a kernel eigenvalue problem. *Neural Comput.*, 10:1299–1319, 1998.
- [95] R. Sepulchre, D. Paley, and N. Leonard. Collective motion and oscillator synchronization. In V. Kumar, N. Leonard, and A. Morse, editors, *Proceedings of the Block Island Workshop on Cooperative Control*, volume 309 of *Lecture Notes in Control and Information Sciences*, pages 189–205. Springer-Verlag, 2004.
- [96] R. Sepulchre, D. Paley, and N. Leonard. Stabilization of planar collective motion: All-to-all communication. *IEEE Trans. on Automatic Control*, 52(5):811–824, 2007.
- [97] S. J. Simpson, G. A. Sword, P. D. Lorch, and I. D. Couzin. Cannibal crickets on a forced march for protein and salt. *Proc. Natl. Acad. Sci. USA*, 103(11):4152–4156, 2006.
- [98] A. R. E. Sinclair and M. Norton-Griffiths. *Serengeti: Dynamics of an Ecosystem*. University of Chicago, Chicago, 1979.

- [99] J. Toner and Y. Tu. Flocks, herds, and schools: a quantitative theory of flocking. *Phys. Rev. E*, 58:4828–4858, 1998.
- [100] C. M. Topaz and A. L. Bertozzi. Swarming patterns in a two-dimensional kinematic model for biological groups. *SIAM J. Appl. Math.*, 2004.
- [101] B. P. Uvarov. *Grasshoppers and Locusts*. Imperial Bureau of Entomology, London, 1928.
- [102] T. Vicsek, A. Czirok, E. Ben-Jacob, I. Cohen, and O. Shochet. Novel type of phase transition in a system of self-driven particles. *Phys. Rev. Lett.*, 75:1226–1229, 1995.
- [103] W.-m. Hwu. GPU computing—programming, performance, and scalability. In *Proceedings of the Block Island Workshop on Cooperative Control*. 2007.
- [104] K. Warburton and J. Lazarus. Tendency-distance models of social cohesion in animal groups. *J. theor. Biol.*, 150:473–488, 1991.
- [105] D. Wiehs. Hydrodynamics of fish schooling. *Nature*, 241:290–291, 1973.
- [106] S. R. Witkin. The importance of directional sound radiation in avian vocalization. *The Condor*, 79(4):490–493, 1977.